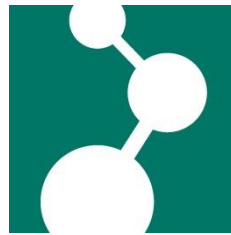


Max Planck **Graduate Center** 
mit der Johannes Gutenberg-Universität



Dissertation for Attaining the Academic Degree of “Doktor rerum naturalium” (Dr. rer. nat.)

of the Departments

08 – Physics, Mathematics, and Computer Science,

09 – Chemistry, Pharmaceutics, and Geosciences,

10 – Biology,

and University Medicine

of the Johannes Gutenberg University

Multifunctional Metal Oxocluster/Polymer Hybrid Nanoparticles

Cesare Benedetti

Mainz, April 2017

1st Supervisor:

2nd Supervisor:

Date of Examination: May 5th, 2017

I hereby declare that I wrote the dissertation submitted without any unauthorized external assistance and used only sources acknowledged in the work. All textual passages which are appropriated verbatim or paraphrased from published and unpublished texts as well as all information obtained from oral sources are duly indicated and listed in accordance with bibliographical rules. In carrying out this research, I complied with the rules of standard scientific practice as formulated in the statutes of the Johannes Gutenberg University Mainz to ensure standard scientific practice.

Mainz, April 2017

Abstract

The design and the applications of novel metal oxocluster/polymer hybrid nanoparticles is the main focus of the present PhD thesis. The targeted hybrid materials are characterized by the covalent incorporation of structurally well-defined and functionalized oxoclusters of group 4 metals (zirconium and titanium) in organic polymers (e.g., methyl methacrylate, *N*-isopropylacrylamide). Free radical copolymerization, initiated either by using thermo- or photoactivation, occurs in the confined space of miniemulsion droplets, providing a degree of control of size and size distribution of the resulting hybrid particles. Because of the nanometric dimensions of the synthesized hybrid systems, higher surface area, an enhanced dispersibility, and processability are achieved. The formation of a strong chemical bond between the organic and the inorganic counterparts has the advantage of protecting the *guest* species (oxoclusters), increasing its stability towards hydrolysis, and providing a homogeneous distribution in the polymer particles. Moreover, because of the functionalization with a high number (6–24) of polymerizable bonds, metal oxoclusters act as cross-linking units for the resulting hybrid polymer matrix. The advantages of using inorganic-based cross-linkers over the “traditional” organic ones are: (i) the enhancement of thermal and mechanical properties of polymers by the inorganic component; (ii) the introduction of specific functional properties (e.g., catalytic properties of $\text{Zr}_4\text{O}_2(\text{OMc})_{12}$); and (iii) a higher cross-linking efficiency due to their multiple docking points. Linear polymers are turned into cross-linked polymers, thus being able to swell in appropriate solvents. The consequent swelling of the resulting hybrid polymer matrix is exploited for applications ranging from the regulation of the catalytic activity to the thermo-responsive fluorescence of encapsulated dyes. The use of different surfactants shows major differences on morphology, cross-linking efficacy, and catalytic performances of the nanoparticles. The choice of the atomic ratio between the oxocluster and the monomer is crucial for tuning structural and functional properties according to the final applications of the material. The synergic outcome, given by the embedding of an inorganic metal oxocluster into a polymer matrix, gives enhanced functionality to the resulting materials, when compared to the individual starting counterparts.

Kurzfassung

Das Design und die Anwendung von neuartigen Metalloxocluster/Polymer-Hybrid-Nanopartikeln ist der Schwerpunkt der vorliegenden Dissertation. Die gezielt hergestellten Hybridmaterialien zeichnen sich durch den kovalenten Einbau von strukturell gut definierten und funktionalisierten Metalloxocluster der vierten Nebengruppe (Zirkonium und Titan) in organischen Polymeren (z.B. Methylmethacrylat, *N*-Isopropylacrylamid) aus. Freie radikalische Copolymerisation, die entweder durch Verwendung von Thermo- oder durch Photoaktivierung initiiert wird, tritt im eingeschränkten Raum von Miniemulsionströpfchen auf und liefert somit einen Grad an Kontrolle über Größe und Größenverteilung der resultierenden Hybridpartikel. Aufgrund der nanometrischen Dimensionen der synthetisierten Hybridsysteme werden eine höhere Oberfläche, eine erhöhte Dispergierbarkeit und Verarbeitbarkeit erreicht. Die Bildung einer starken chemischen Bindung zwischen den organischen und den anorganischen Komponenten hat den Vorteil, dass die Gast-Spezies (Oxocluster) geschützt, ihre Stabilität gegenüber Hydrolyse erhöht und eine homogene Verteilung in den Polymerpartikeln gewährleistet wird. Darüber hinaus wirken Metalloxocluster, aufgrund der Funktionalisierung mit einer hohen Anzahl (6-24) von polymerisierbaren Bindungen, als Vernetzungseinheiten für die resultierende Hybridpolymermatrix. Die Vorteile der Verwendung von anorganischen Vernetzern gegenüber den „traditionellen“ organischen sind: (i) die Verbesserung der thermischen und mechanischen Eigenschaften von Polymeren dank der anorganischen Komponente; (ii) die Einführung spezifischer funktioneller Eigenschaften (z.B. die katalytischen Eigenschaften von $Zr_4O_2(OMc)_{12}$); und (iii) eine höhere Vernetzungswirkung aufgrund ihrer mehrfachen Andockmöglichkeiten. Lineare Polymere werden so zu vernetzten Polymeren, was sie in geeigneten Lösungsmitteln quellen lässt. Die daraus folgende Quellung der resultierenden Hybridpolymermatrix wird für Anwendungen ausgenutzt, die von der Regulierung der katalytischen Aktivität bis hin zur thermoempfindlichen Fluoreszenz von eingekapselten Farbstoffen reichen. Die Verwendung verschiedener Tenside zeigt große Unterschiede in der Morphologie, der Vernetzungswirksamkeit und den katalytischen Leistungen der Nanopartikel. Die Wahl des Atomverhältnisses zwischen dem Oxocluster und dem Monomer ist entscheidend zur Regulierung struktureller und funktioneller Eigenschaften gemäß den endgültigen Anwendungen des Materials. Das

synergetische Ergebnis, das durch die Einbettung eines anorganischen Metall-Oxocluster in eine Polymermatrix gegeben wird, verleiht den resultierenden Materialien im Vergleich zu den einzelnen Ausgangsgegenständen eine verbesserte Funktionalität.

Contents

1. Motivation.....	1
2. Theoretical Background	6
2.1. Transition Metal Oxoclusters and Metal Oxocluster/Polymer Hybrid Materials.....	6
2.1.1. Transition Metal Oxoclusters	7
2.1.2. Organic-Inorganic Hybrids based on Metal Oxoclusters.....	10
2.2. Synthetic Approach for Metal Oxocluster/Polymer Hybrids.....	12
2.2.1. Polymerizations Techniques.....	13
2.2.2. Solution Polymerization.....	13
2.2.3. Bulk Polymerization	13
2.2.4. Thermal and UV Curing.....	14
2.2.5. Miniemulsion Polymerization.....	14
2.3. Miniemulsion	14
2.3.1. Stability of Miniemulsion	16
2.3.2. Miniemulsion Polymerization of Metal Oxocluster/Polymer Hybrids.....	19
3. Characterization Techniques	21
3.1. Gel Permeation Chromatography (GPC)	21
3.2. Inductively Coupled Plasma Optical Emission Spectrometry (ICP-OES)	22
3.3. Electron Microscopy.....	22
3.3.1. Scanning Electron Microscopy (SEM)	23
3.3.2. Transmission Electron Microscopy (TEM).....	23
3.4. X-ray Absorption Spectroscopy (XAS)	24
3.5. Dynamic Light Scattering (DLS)	25
3.6. Attenuated Total Reflectance (ATR).....	26
4. Result and Discussion.....	27
4.1. Dual Role of Zirconium Oxoclusters in Hybrid Nanoparticles: Cross-Linkers and Catalytic Sites	27
4.1.1. Introduction	27
4.1.2. Particle Synthesis and Composition.....	29
4.1.3. Morphology and Structure.....	32

4.1.4.	Cross-Linking, Swelling, and Thermal Properties	37
4.1.5.	Catalysis: Oxidation of Methyl <i>p</i> -Tolylsulfide.....	42
4.1.6.	Other Catalytic Trials	48
4.1.7.	Zr ₄ -Surfactants Interaction.....	49
4.1.8.	Conclusions	53
4.2.	Titanium Oxocluster-based Thermoresponsive Hybrid Nanoparticles for Catalysis Applications	54
4.2.1.	Introduction	54
4.2.2.	Homogeneous Catalysis with Ti ₉ O ₈ (OPr) ₄ (OMc) ₁₆	56
4.2.3.	Heterogeneous Catalysis with Hybrid Poly(NAGA- <i>co</i> -Zr ₄), Poly(NMGA- <i>co</i> -Zr ₄) and Poly(NIPAM- <i>co</i> -Zr ₄) Nanoparticles.....	58
4.2.4.	Conclusions	62
4.3.	Zirconium Oxocluster/Polymer Hybrid Nanoparticles Prepared by Photoactivated Miniemulsion Copolymerization	62
4.3.1.	Introduction	63
4.3.2.	Initiation of the Copolymerization and Particle Morphology	64
4.3.3.	Compositions, Cross-Linking, and Thermal Properties	70
4.3.4.	Polymerization Kinetics.....	72
4.3.5.	Conclusions	76
4.4.	Hybrid Nanocapsules as a Potential Nano-Thermometer System	77
4.4.1.	Introduction	77
4.4.2.	Nanocapsule Synthesis	79
4.4.3.	Composition and Morphology.....	79
4.4.4.	Thermoresponsive Fluorescence Behavior	83
4.4.5.	Conclusions and Outlook	87
5.	Conclusions.....	89
6.	Experimental Part	91
6.1.	Experimental Details for Section 4.1	91
6.1.1.	Materials	91
6.1.2.	Synthesis of Zr ₄ O ₂ [O(O)CC(CH ₃)=CH ₂] ₁₂ (Zr ₄).....	91
6.1.3.	Preparation of Cross-Linked Hybrid Poly(MMA- <i>co</i> -Zr ₄) Nanoparticles.....	92
6.1.4.	Catalytic Experiments	93
6.2.	Experimental Details for Section 4.2	94
6.2.1.	Materials	94

6.2.2.	Synthesis of Amphiphilic Block Copolymer Poly(ethylene/butylene)- <i>block</i> -Poly(ethylene oxide) (P(E/B)- <i>b</i> -PEO) Copolymer	94
6.2.3.	Synthesis of <i>N</i> -Acryloyl Glycinamide (NAGA)	94
6.2.4.	Synthesis of <i>N</i> -Methacryloyl Glycinamide (NMGA)	94
6.2.5.	Synthesis of $Ti_9O_8(OPr)_4(OMc)_{16} (Ti_9)$	95
6.2.6.	Preparation of Hybrid Poly(PNIPAM- <i>co</i> - Ti_9) Nanoparticles	95
6.2.7.	Preparation of Hybrid Poly(NAGA- <i>co</i> - Ti_9) and Hybrid Poly(NMGA- <i>co</i> - Ti_9) Nanoparticles	96
6.2.8.	Catalytic Experiments	96
6.3.	Experimental Details for Section 4.3	96
6.3.1.	Materials	96
6.3.2.	Synthesis of $Zr_4O_2[O(O)CC(CH_3)=CH_2]_{12} (Zr_4)$	97
6.3.3.	Preparation of Cross-Linked Hybrid Poly(MMA- <i>co</i> - Zr_4) Nanoparticles by Thermally Activated Free Radical Polymerization	97
6.3.4.	Preparation of Cross-Linked Hybrid Poly(MMA- <i>co</i> - Zr_4) Nanoparticles by Photoactivated Free Radical Polymerization	98
6.3.5.	Kinetic FTIR Investigation of the Polymerization Process of the Cross-Linked Hybrid Poly(MMA- <i>co</i> - Zr_4) Nanoparticles	98
6.4.	Experimental Details for Section 4.4	99
6.4.1.	Materials	99
6.4.2.	Synthesis of $Zr_4O_2[O(O)CC(CH_3)=CH_2]_{12} (Zr_4)$	99
6.4.3.	Preparation of Cross-Linked PNIPAM and PNIPMM Nanocapsules	99
6.5.	Characterization Techniques	100
6.5.1.	Gel Permeation Chromatography (GPC)	100
6.5.2.	Inductively Coupled Plasma Optical Emission Spectrometry (ICP-OES)	101
6.5.3.	Scanning Electron Microscopy (SEM)	101
6.5.4.	Transmission Electron Microscopy (TEM)	101
6.5.5.	X-ray Absorption Spectroscopy (XAS)	102
6.5.6.	Dynamic Light Scattering (DLS)	102
6.5.7.	Differential Scanning Calorimetry (DSC)	103
6.5.8.	Nuclear Magnetic Resonance (NMR)	103
6.5.9.	X-Ray Photoelectron Spectroscopy (XPS)	103
6.5.10.	Fluorescence Measurements	104
6.5.11.	FTIR Measurements	104
7.	References	105

A. Acronyms List and Symbols	124
B. List of Figures	127
C. List of Tables	132
D. List of Schemes	133
E. Acknowledgments.....	134
F. Curriculum Vitae	135
G. Scientific Contributions	136
G.1. Publications.....	136
G.2. Conferences	137

1. Motivation

“Synergy – the bonus that is achieved when things work together harmoniously”

Mark Twain

The term hybrid is used whenever at least two different counterparts are involved and co-present in the same system: anything deriving by the combination of different components that originates another entity, which works autonomously, and has in common the features of all the counterparts can essentially be called a hybrid (Figure 1.1). The term hybrid, broadly used with all its facets in many different fields and for different purposes, becomes meaningful only when it is supported by an essential feature: synergy. It is, indeed, the enhanced combined result that gives a crucial reason to mix two or more starting counterparts.

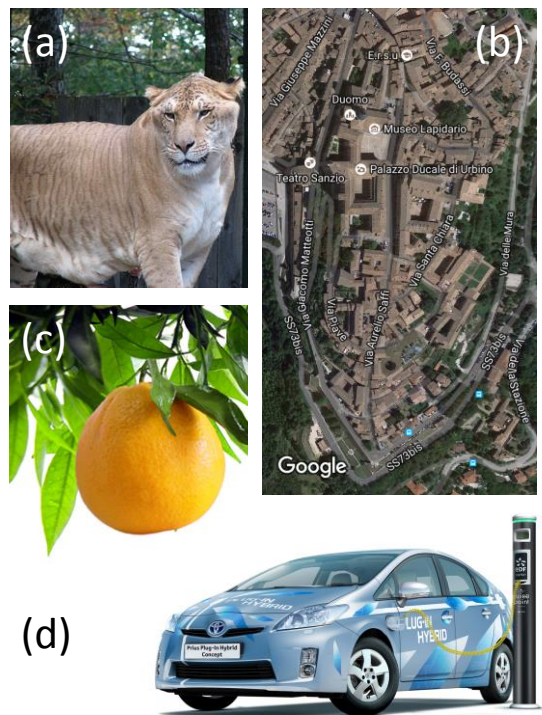


Figure 1.1. Hybrid examples: (a) a liger is a hybrid cross between a male lion (*Panthera leo*) and a female tiger (*Panthera tigris*);ⁱ (b) hybrid maps (of the city of Urbino) are the combination of satellite maps and street maps;ⁱⁱ (c) grapefruit (*Citrus × paradisi*) is a hybrid originating between sweet orange (*C. sinensis*) and pomelo or shaddock (*C. maxima*);ⁱⁱⁱ (d) Hybrid Toyota vehicles.^{iv}

ⁱ Courtesy by <http://ligerfacts.org/> (Feb. 2017)

ⁱⁱ Courtesy by Google (Feb. 2017)

ⁱⁱⁱ Courtesy of <http://www.keyword-suggestions.com/cGluyBncmFwZWZydWI0IHRYZWU/> (Feb. 2017)

^{iv} Courtesy of <http://www.ecoautoninja.com> (Feb. 2017)

Nowadays, when thinking about hybrids, one of the first things that come to our mind is probably the so-called hybrid vehicles. Those cars are a great example of the hybrid concept definition: they run exploiting two different energy sources (usually a combustion engine combined with an electric motor). There is a resulting synergic outcome: depending on the driving conditions hybrid vehicles can be used with one or the other fuel decreasing in consumption, thus lowering greenhouse gas emissions and also increasing the overall efficiency.

Nevertheless, the contribution of this thesis is oriented to material science rather than to engineering or everyday life, we should narrow the field and start to talk about hybrid materials. Kickelbick proposed the following definition: “A hybrid material consists of at least two components – usually an inorganic and an organic component – that are molecularly dispersed in the material”.¹ The first to take advantage of this kind of materials was Mother Nature.²⁻³ For example, bone and teeth are good examples of the synergetic combination between the inorganic mineral calcium phosphate, present as calcium hydroxyapatite ($\text{Ca}_{10}(\text{PO}_4)_6(\text{OH})_2$), and the organic protein collagen (mainly of type I).⁴⁻⁶ The result is a composite material that retains the high rigidity of the inorganic material by improving fracture resistance due to the elasticity of the protein.

Even before William Whewell coined the term *scientist*, humans were already producing hybrid materials by taking inspiration from nature. An example of ancient hybrid material is the old dye Maya blue (Figure 1.2). Unlike the blue dyes used in Europe, Egypt or Asia, the pigment is not a copper mineral, nor is it related to natural ultramarine, ground Lapis Lazuli or azurite. Maya blue is the result of the incorporation of blue indigo (a natural organic chromophore) within the channels of palygorskite (micro-fibrous clay with formula $(\text{Mg},\text{Al})_4\text{Si}_8(\text{O},\text{OH},\text{H}_2\text{O})_{24}$). Considered one of the greatest technological and artistic achievements of Mesoamerica, the brilliant tonality of Maya blue can be still observed more than twelve centuries later because of the mechanical strength of the hosting clay.

Currently, hybrid materials represent a hot topic and are being investigated in many different fields of materials science.⁷⁻⁸ The most fascinating aspect of organic–inorganic hybrid materials is their variability and versatility, both deriving from a theoretically infinite number of combinations in terms of chemical nature and relative amounts.^{7, 9-12} Indeed, the union of different properties in only one material is what makes these systems attractive from a scientific and technological point of view.¹³ Organic–inorganic hybrid materials represent a wide range of different systems including crystalline highly

ordered coordination materials and amorphous compounds produced by sol-gel, from materials which have strong chemical interactions between the counterparts to the ones characterized instead by weak chemical interactions or simple physical mixing.

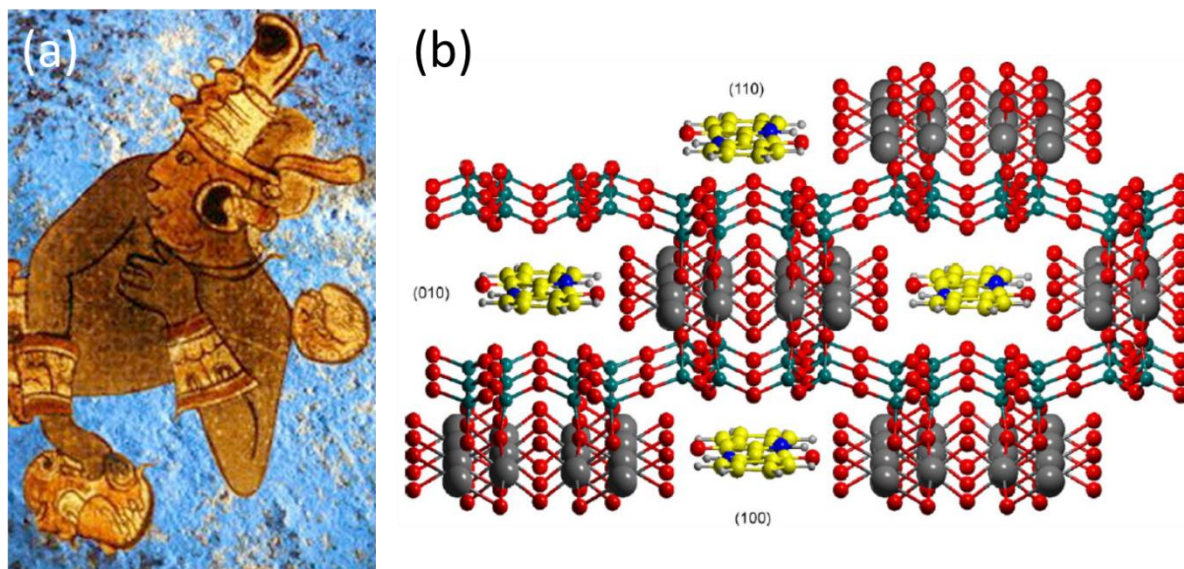


Figure 1.2. Maya blue: (a) on the background of an ancient Mayan paint and (b) chemical structure by Chiari *et al.*¹⁴

A broadly accepted definition for the term *hybrid* distinguishes between the possible interactions existing between the inorganic and the organic components:⁹ (i) class I hybrid materials, characterized by weak interactions (*i.e.*, van der Waals, hydrogen bonding or weak electrostatic interactions) between the two phases; (ii) class II hybrid materials, which are those that have strong (covalent or ionic) bonds among the components.

In this thesis, we are dealing with class II hybrid materials obtained by covalent incorporation of inorganic metal-based building blocks (in the following labeled as BB) into a polymer matrix through copolymerization between organically functionalized inorganic clusters and suitable monomers.^{7, 9, 15-16} Among inorganic nanosized BB, oxide-based clusters (*e.g.*, polyhedral silsesquioxanes (POSS)¹⁷⁻¹⁸, polyoxometalates (POM)¹⁹⁻²⁶, metal oxo-clusters²⁷⁻²⁹) are receiving growing attention. The wide range of appealing properties of oxide-based clusters results from the chemical variability of both constituent metal and structure, as well as from the different functionalization strategies aimed at developing hybrid derivatives.

Herein, the polymerization between transition metal oxoclusters of the group 4 (zirconium and titanium) with organic monomers (methyl methacrylate, *N*-isopropylacrylamide, etc.) has been studied. Metal oxoclusters are polynuclear neutral

complexes with a general formula $M_xO_y(OH)_w(OOR)_z$, where the R groups are typically polymerizable groups that can react, in a further synthetic step, with a suitable monomer. Oxoclusters feature typically from 6 to 24 polymerizable groups and can then trigger a high cross-linking in the polymer. As a consequence, linear polymers are turned into cross-linked polymers, and they are no longer soluble in organic solvents, but swell instead. The resulting swelling behavior could be exploited, for instance, for regulating the catalytic activity of a hybrid material-based heterogeneous catalyst or for delivery purposes.

The targeted hybrid materials are synthesized by free radical polymerization occurring in the confined space of miniemulsion droplets. The miniemulsion technique is known as a versatile technique to prepare a wide range of polymer and hybrid nanoparticles.³⁰⁻³⁷ Because of the nanometric dimension of the synthesized hybrid systems, higher surface area and an enhanced dispersibility are achieved. On one hand, an enhanced processability results from the colloidal character of the obtained hybrid materials. On the other hand, the high shear forces required to form a miniemulsion ensures a homogeneous distribution of the inorganic *guest* in each droplet and in each hybrid/polymer particle formed.

In the following, preparation and the application of metal oxocluster/polymer hybrid nanoparticles are discussed. The initiation of the free radical copolymerization between the metal oxoclusters and the chosen organic monomer is kinetically investigated in the case of both thermo- and photo-activation. The variation of nature, amount, and atomic ratio between the oxocluster and the monomer can be used to tune the structural and functional properties of the materials. The use of different surfactants to pursue the formation of the miniemulsion results in relevant differences in morphology, cross-linking efficacy, and catalytic performances of the nanoparticles. The synergic effect related to the covalent incorporation of an inorganic comonomer into a polymer matrix is reported. Metal oxoclusters are acting as a cross-linker for the resulting particles polymer matrix, as well as catalytic sites. A higher swelling is triggered in suitable solvents, thus allowing the substrate molecules to easily access through the swollen nanoparticle matrix towards the catalytically active oxocluster core. It is, indeed, the described resulting synergic outcome obtained by combining the two roles what provides enhanced functionality to the materials when compared to the individual counterparts (organic polymer matrix and metal oxocluster).

This work consists of five chapters and is organized as follows. Chapter 2 focuses on transition metal oxoclusters and their related hybrid materials; the different synthetic procedures to obtain metal oxocluster hybrid materials, and the benefit of using miniemulsion polymerization are also reported. In Chapter 3, the main characterization methods applied to study the chemical-physical, structural, and morphological features of the hybrids prepared during the thesis, as well as their catalytic performance, are briefly described. The results of the experiments and the characterization of the metal oxocluster hybrid nanoparticles are discussed in the four sections of Chapter 4. Each section is introduced, motivating the purpose of the work, and systematically discussed. Chapter 5 describes the experimental parameters for the synthesis and the acquisition conditions for the characterization.

2. Theoretical Background

2.1. Transition Metal Oxoclusters and Metal Oxocluster/Polymer Hybrid Materials

The formation of a strong chemical bond between organic and inorganic BB (class II hybrid materials) has the advantage of providing a homogeneous distribution of the guest species in the host matrix, overcoming problems related to phase separation, aggregation, and migration of oxoclusters in the matrix, and even leaching.²⁸ Unlike the chemistry of polyhedral oligomeric silsesquioxanes, where organic modification of the silicon-based clusters are occurring through sol-gel processing, for metal oxoclusters this approach cannot be applied due to the higher hydrolytic instability of metal-carbon bonds (with respect to silicon-carbon bonds).³⁸⁻³⁹ For metal oxoclusters, the only possibility to form the cluster core and to anchor suitable organic groups to its surface is by using bi- or multidentate groups (chelating or bridging, such as carboxylates, sulfonates, phosphonates, and β -diketonates).⁴⁰ Since class II hybrid materials are characterized by strong bonds between organic and inorganic components, metal oxoclusters must carry polymerizable moieties to be finally incorporated into a polymer matrix. Polymerizable ligands can be embedded in two main ways, through (Figure 2.1):

- Post-synthesis surface functionalization, which allows the grafting of functional reactive groups on the surface of a preformed cluster.
- Direct *in situ* functionalization of the inorganic BB during its synthesis.⁴¹⁻⁴²

Both ways allow either a single or a multiple anchoring of the inorganic BB to the polymer surface, thus forming either a linear polymeric chains with pending cluster attached or creating a cross-linked network. An example of post-synthesis functionalization are the magnetic manganese oxide clusters of general composition $Mn_{12}O_{12}(OOCR)_{16}$ (R = alkyl, aryl), which are prepared from manganese acetate, the corresponding acid, and $KMnO_4$. The strongly oxidizing conditions during the synthesis do not allow the incorporation of unsaturated groups.⁴³ Instead, the *in situ* multiple functionalization of an inorganic core by bidentate organic ligands is adopted for metal oxoclusters of the IV group (Ti^{IV} , Zr^{IV} , Hf^{IV}). These organic ligands have both a carboxyl coordinating group, with which they contribute to form the core (the terminology *oxo*-cluster derives indeed by the presence of the $RC(O)O-$ groups coordinating to the metal

atoms, thus shaping the cluster core with M-O-M bonds), and at the other extreme a polymerizable functional group, which, upon copolymerization with suitable monomers, allows the covalent incorporation into a polymer matrix.^{27-29, 40, 44} Hereafter, we will deepen in the chemistry of metal oxoclusters formed by *in situ* functionalization and in the relative based hybrid materials.

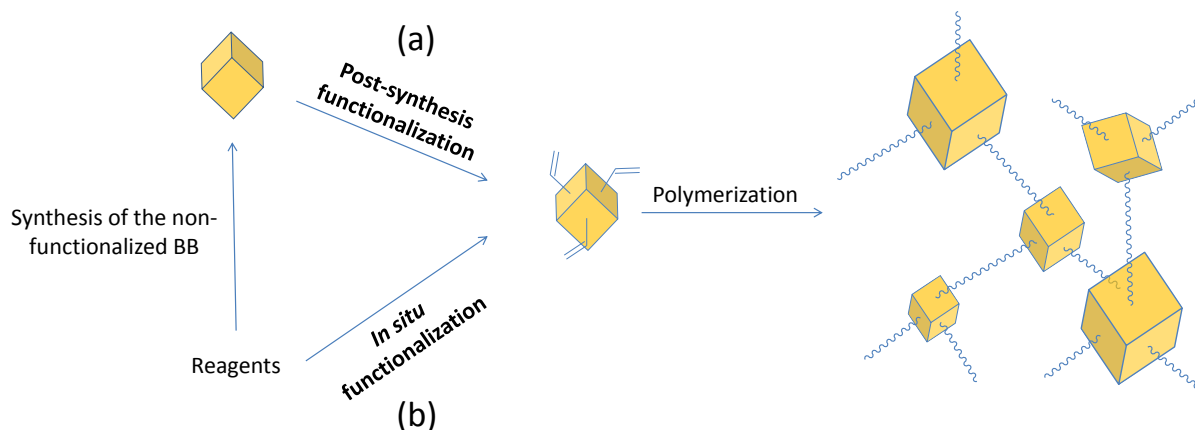


Figure 2.1. Possible ways to functionalize inorganic BB: (a) post-synthesis surface functionalization and (b) direct *in situ* functionalization. The formed functionalized cluster is either way used as inorganic BB in the next polymerization step.¹⁶

2.1.1. Transition Metal Oxoclusters

Transition metal oxoclusters, with the general formula $M_xO_y(OH)_w(OC(O)R)_z$, are neutral complexes (Figure 2.2). They are based on a polyhedral inorganic core, composed by M-O-M bridges (with M as transition metal typically in its highest oxidation state, *e.g.*, Ti^{IV} , Zr^{IV} , Hf^{IV} , and Nb^V), coordinated by carboxylates ($RC(O)O^-$) acting often as bidentate organic ligands.^{27-28, 40, 45} Later transition metals (*e.g.*, Ag) or alkaline earth (*e.g.*, Ba, Mg) metals can also be present in the structure.⁴⁶ Oxoclusters display different nuclearity and, as a consequence, a number of metal atoms per structure (from 2 to 12). The coordination number of the metal atoms and the connectivity fashion (corner, edge or face sharing) of the metal-oxygen polyhedral depend on the metal nature and on the structure.

Metal oxoclusters are typically synthesized by reaction of a metal alkoxide (RO^-) with a carboxylic acid. A series of reaction steps of substitution, hydrolysis, and condensation lead to the formation of the polynuclear complex, called metal oxocluster.⁴² *Step 1* is the partial substitution of the alkoxide (RO^-) group with the bidentate ligand of

the carboxylic acid chosen. During the substitution reaction, alcohol molecules are formed.

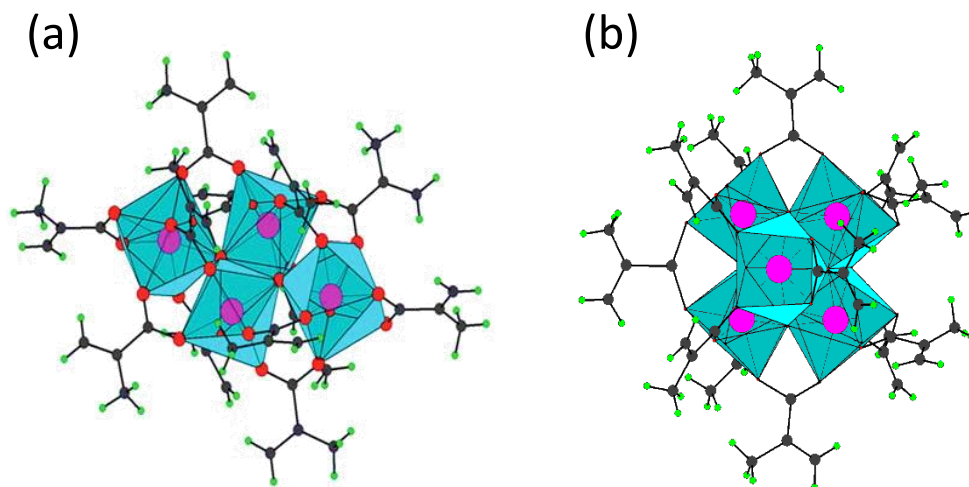


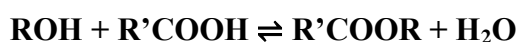
Figure 2.2. Structure of (a) $Zr_4O_2(OMc)_{12}$ ⁴⁷ and (b) $Zr_6(OH)_4O_4(OMc)_{12}$.⁴⁸

Esterification is occurring in *Step 2*, they react with the excess of the carboxylic acid, thus forming water. Water molecules react with the metal partially substituted alkoxide (formed in *Step 1*, characterized by the presence of both alkoxide and carboxylic ligands) in *Step 3*, thus forming the polynuclear structure (based on M–O–M ligands) of the metal oxoclusters.⁴² The formation and the final structural features of oxoclusters depend on (i) the pKa of the carboxylic acid used and, therefore, the dissociation and the number of carboxylic groups available, (ii) the nature of the solvent, (iii) the steric and electronic factors of the –R group linked to the alkoxide, (iv) the oxidation state of the metal, and (v) the molar ratio between the alkoxide and the acid. The latter affects first the formation of the alcohol, and therefore the following esterification, and secondly, the nuclearity of the oxocluster.³⁸ In fact, the esterification, being the slowest reaction step, plays an important role determining the quantity of water formed *in situ* and, as a consequence, the condensation degree and the structure of the inorganic *core*.

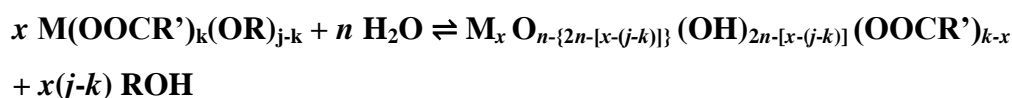
Substitution (Step 1)



Esterification (Step 2)



Condensation (Step 3)



This work is focused on monometallic oxoclusters of zirconium and titanium, in particular on $Zr_4O_2(OMc)_{12}$ (**Zr₄**) and $Ti_9O_8(OPr)_4(OMc)_{16}$ (**Ti₉**).

2.1.1.1. Zirconium Oxoclusters

The first zirconium oxoclusters were synthesized in the early 1990s by Kickelbick using different zirconium alkoxide and methacrylic acid (Figure 2.2b).⁴⁸ In the following years, further contributions were also done by Trimmel, Gross, etc.⁴⁷⁻⁵² Here we focus on $Zr_4O_2(OMc)_{12}$ (**Zr₄**, Figure 2.2a), synthesized by combining a solution of 80% $Zr(O^iBu)_4$ in *n*-butanol with methacrylic acid in a molar ratio of 1:7. In the solid state, **Zr₄** is characterized by four zirconium atoms lying on the same plane: the two closer in the center (with a minimum distance of 3.2945(6) Å) are coordinated by eight oxygen atoms, while the other two are 7-coordinated. Two ligands μ_3 -oxygen are capping two Zr_3 polyhedrons on opposite sides of the plane. The methacrylate ligands are in two different coordination modes: two η^2 are chelating the two farther zirconium atoms, and the other ten μ^2 are symmetrically bridging two symmetrically different metal atoms. The structure also has an inversion center (C_i).

A further asymmetric **Zr₄** isomer can be obtained by using a molar ratio of 1:4 of methacrylic anhydride instead of methacrylic acid. The four zirconium atoms have a distorted butterfly arrangement. In this case, three zirconium atoms are coordinated by eight oxygen atoms, while the fourth is only 7-coordinated. Concerning the methacrylate ligands: two are chelating, nine are symmetrically bridging, and one is the η^2, μ_2 -coordination mode in which one of the oxygen atoms of a chelating carboxylate group additionally coordinates to another metal atom.⁴⁷

2.1.1.2. Titanium Oxoclusters

The first reported Ti-based oxocluster is the hexameric cluster of titanium(IV), with the formula $Ti_6O_4(OR)_8(OMc)_8$, synthesized by Doeuff *et al.* at the end of the 80's.⁵³⁻⁵⁵ In the following years, many others titanium oxoclusters have been extensively prepared and studied by Schubert's, Klemperer's, and Sanchez's groups.^{54, 56-58} As described in Section 4.2, $Ti_9O_8(OPr)_4(OMc)_{16}$ (**Ti₉**, Figure 2.3) has been synthesized by reacting $Ti(OPr)_4$ with 4-fold excess of methacrylic acid. The structure is characterized by a ring of nine $[TiO_6]$ octahedrals linked by six μ_2 - and two μ_3 -oxide bridges. All titanium atoms are octahedrally coordinated and all the methacrylate groups are acting as bridges. In contrast to Zr structures, where it is possible to have coordination numbers higher than 6 (which is the maximum degree of substitution for titanium

compounds), in case of **Ti**, the higher degree of substitution by bidentate carboxylate ligands forces the structure to open and become less condensed. Except two of the nine octahedra present, which share an edge, all the others share the *cis* vertices. Moreover, the macrocycle is asymmetric since two octahedra are connected only by one methacrylate bridge, while the second bridge is replaced by two OPr ligands.⁵⁹

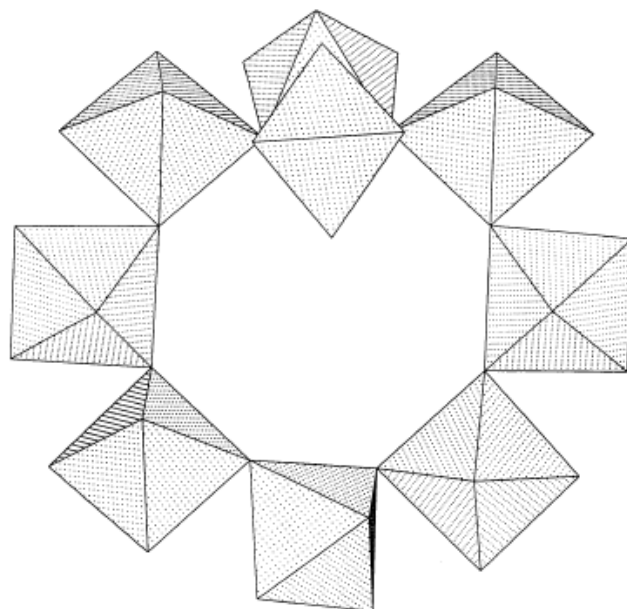


Figure 2.3. Structure of $\text{Ti}_9\text{O}_8(\text{OPr})_4(\text{OMc})_{16}$ by Kickelbick *et al.*⁵⁹

2.1.2. Organic-Inorganic Hybrids based on Metal Oxoclusters

Owing to their tunable structure (in terms of composition, polyhedral arrangement, nuclearity, and functionalization) metal oxoclusters represent outstanding BB for the preparation of organic–inorganic hybrid materials.^{27-29, 40, 44, 47, 60-62} In this regard, the choice of a suitable bidentate carboxylic ligand during the synthesis of the metal oxocluster has several distinctions. First of all, the cluster acts as a comonomer (*i.e.*, the ligands around the cluster take part in the polymerization), therefore the carboxylic ligand should contain a vinyl group (direct *in situ* functionalization). Second, the dispersion and solubility of the cluster in the monomer are also determined by the choice of ligands, thus resulting in a homogeneous distribution of the oxocluster within the copolymer matrix, overcoming problems related to phase separation, aggregation, and migration.

The synergic covalent incorporation of metal oxoclusters into a polymer matrix could bring structural improvements and/or functional endowments to the resulting hybrid

polymer matrix.²⁸ When the final material retains the main characteristic of a polymer, but the presence of an inorganic guest is able to make some structural enhancement, the incorporation of the oxocluster is defined as structural improvement. Structurally defined oxoclusters with 6 to 24 polymerizable groups can promote a high cross-linking of linear organic polymers.^{15, 45, 63-64} The cross-linked polymer matrix is no longer soluble in organic solvents, but it typically swells upon storage in an organic solvent.⁴⁷ Moreover, incorporation of early transition metal oxoclusters has been shown to improve the mechanical (strength, hardness, brittleness, scratch resistance, *etc.*)⁶⁵⁻⁶⁶ and thermal resistance of the resulting copolymers.^{16, 27, 58, 60, 67-73} As reported by Gao *et al.*, the glass transition temperature (T_g) of PMMA (105 °C) increases to 127.5 °C when the polymer is cross-linked by 0.3 mol% $Ti_6O_4(OEt)_8(OMc)_8$.⁶⁷ The enhanced structural properties have enabled the application of metal oxocluster based hybrid materials as coating films for wood, cellulose and alloy,^{50, 74-77} and as shape memory materials.⁷⁸

Functional endowments are occurring when the final material is enriched with some intrinsic properties of the oxocluster itself. A hybrid material can be processed as polymer albeit having the properties of an inorganic material. Schubert *et al.* reported the study of the magnetic behavior of the hybrid polymer obtained by copolymerization of $Mn_{12}O_{12}(acrylate)_{16}$ with ethyl acrylate.⁴³ This was the first case that the functional properties of an oxocluster were transferred to the resulting hybrid material. Mn_{12} oxoclusters are well known as magnetic molecular clusters, and similar results were obtained by Willemin *et al.*⁷⁹ Furthermore, the work by Sessoli *et al.*⁸⁰⁻⁸³ disclosed the possibility to use Mn oxoclusters for storing information at molecular level, because of the slow relaxation of the magnetization. Hybrid polymer nanoparticles based on Mn_{12} and Mn_8Fe_4 oxoclusters were also adopted as potential magnetic imaging agents by Stoll *et al.*^{33, 84} Mn oxoclusters were polymerized with styrene, being the first time that a metal oxocluster based hybrid/polymer nanomaterial was prepared by using the confinement environment of miniemulsion droplets.

In the field of optics, the incorporation of heavier metals (such as Zr and Hf) in oxoclusters results in an increase of the refractive index of the polymer matrix. Since the incorporation of oxocluster is generally quite low (up to 10 wt%), no relevant change are observed in the optical properties.⁸⁵⁻⁸⁸ In contrast, about optical properties induced directly from the nature of the cluster, Sanchez *et al.* have described the photochromicity observed in hybrid materials produced by the embedding Ti oxoclusters into poly(hydroxyethyl-methacrylate).^{12, 89}

Regarding electric properties, the investigation of dielectrical properties for the development of field effect transistor (FET) using zirconium- and hafnium oxoclusters-based hybrid materials has been assessed.^{47, 49, 64, 90-92} The dielectric performances of the material have been proven to be strongly affected by the presence and the amount of the inorganic cross-linker, which does not migrate within the polymer matrix and endows it with very low dielectric constant values.

Recently, the use of hybrid materials containing metal oxocluster of Zr and Hf as heterogeneous catalysts was also highlighted. In particular, due to the ability to activate hydrogen peroxide, these materials were used for the oxidation of sulfur compounds (*e.g.*, methyl *p*-tolylsulfide and dibenzothiophene).^{51-52, 93} A detailed study of this topic is reported in Section 4.1.

2.2. Synthetic Approach for Metal Oxocluster/Polymer Hybrids

The formation of strong bonds between the organic and inorganic BB can be done following two ways:

- Building block approach: during the reaction and afterwards in the final material, the well-defined preformed starting BB maintains their structural and compositional integrity.
- *In situ* formation of the components: one or both structural counterparts are formed through the chemical transformation of the precursors used for the hybrid materials preparation.⁹ Typically this is the case of sol-gel processing, where the majority of the materials are based on polysiloxane backbones.^{38, 94}

The synthesis of metal oxocluster/polymer hybrids belong to the first strategy: the building block approach. The properties of the final material are the result of the synergistic combination of both separate constituents. The formation of the chemical bond between the oxocluster and the monomers takes place by copolymerization, thus allowing the metal oxocluster to be firmly grafted into the polymer latex and providing enhanced chemical stability to the resulting hybrid. Depending on the number and symmetry of the functional groups present around the cluster that can interact, these BB are able to modify a polymer matrix forming linear, partially, or fully cross-linked materials.

An advantage of the building block approach is a better structure–property predictions, possibly due to the absence of significant structural changes during matrix formation. Furthermore, the BB can be designed in order to get the best assembly (*e.g.*, tuning the solubility of inorganic compounds in organic monomers through the choice of different surface groups with different polarity), and consequently give the best performance.

2.2.1. Polymerizations Techniques

For the covalent incorporation of the oxocluster, classical free radical copolymerization is widely used, typically by using carboxylates cluster ligands containing a vinyl group (*i.e.* acrylate- or methacrylate) with organic comonomers, such as acrylates or styrene.^{15, 43, 45, 47-49, 52, 63-64, 68, 70, 90, 92} The polymerization of metal oxoclusters to a polymer matrix has also been extended to other polymerization techniques: atom transfer radical polymerizations (ATRP) with 2-bromoisobutyrate-substituted metal oxoclusters as macroinitiators for the synthesis of hybrid inorganic–organic core–shell nanoparticles,⁹⁵ ring-opening metathesis polymerization (ROMP) with norbornene carboxylate-substituted clusters,⁹⁶ and also thiol–ene free radical reaction.^{62, 97} Moreover, as reported in detail in Section 4.3, an important role is played by the different way of polymerization initiation, activated either by light or by heat.

2.2.2. Solution Polymerization

Trimmel *et al.* were the first to report the synthesis of hybrid materials based on zirconium oxoclusters by using the building block approach of *in situ* functionalized metal oxocluster/polymer hybrid materials.⁹⁸ The study of the cross-linking efficiency of $Zr_6(OH)_4O_4(\text{methacrylate})_{12}$ oxocluster in a poly(methyl methacrylate) matrix was reported. Further studies were also carried out by using $Zr_4O_2(\text{methacrylate})_{12}$ oxocluster, with investigations of swelling behavior and thermal properties.^{47, 63} The synthetic procedure adopted was a free radical polymerization between the Zr oxoclusters and methyl methacrylate, initiated by benzoyl peroxide and triggered by heat. The polymerization was performed in solution using benzene as a solvent. Different polymer morphologies could be obtained by changing the solvent.⁴⁵ Further examples of Zr and Ti oxoclusters-based hybrids synthesized by using solution polymerization and toluene as a solvent are also present in the literature.^{45, 49, 90}

2.2.3. Bulk Polymerization

Although the first attempts in the early 2000s were done by using solution polymerization, bulk polymerization became immediately quite common in the synthesis of metal oxocluster/polymer hybrid materials.^{15, 68, 70-71, 78, 93} The main advantages of this approach are (i) the use of a liquid organic monomers able to solubilize metal oxoclusters and the initiators, and (ii) the purity of the obtained materials (with no solvent entrapped in the matrix). The materials, prepared in absence of a solvent, appear as hard transparent glasses; moreover, they tend to swell less in the presence of an organic solvent. The need to replace the solution method was mainly originated from the inefficacy of the polymerization. The presence of residual unreacted double bonds affects the macroscopic properties, such as mechanical and thermal. Furthermore, the bulk polymerization approach, not involving solvents and volatile organic compounds, is much more sustainable, also from the economic point of view. The initiator benzoyl peroxide was replaced by lauroyl peroxide, with a lower decomposition temperature, first allowing the heat to be released during the reaction, and then avoiding heterogeneous polymerization. It is important to mention the introduction of a pre-polymerization step, followed by quenching in an ice bath. The materials synthesized by using this novel approach showed higher glass transition temperatures and optimized thermal stability. Moreover, the enhanced cross-linking extent had an impact on the swelling behavior of the final materials.⁷⁰

2.2.4. Thermal and UV Curing

Relevant perspectives in the synthesis of metal oxocluster/polymer hybrid materials are further disclosed by the use of UV^{58, 69, 76-77, 97, 99} and thermal curing.^{50, 75} Considerable contributions on the field were done by Di Maggio *et al.* for the synthesis of zirconium oxoclusters based inorganic–organic hybrid coatings for wood^{50, 75} and aluminum.⁷⁷ The technique allows a homogenous deposition of the film in the desired materials.

2.2.5. Miniemulsion Polymerization

Details of miniemulsion, stabilization of miniemulsion, and miniemulsion polymerization of metal oxocluster/polymer hybrid materials are mentioned in the following Section 2.3.

2.3. Miniemulsion

The term emulsion refers to a dispersed liquid (dispersed phase) in another non-miscible liquid (continuous phase). According to size and stability, emulsions can be divided in three major subgroups: *macroemulsions*, *miniemulsions*, and *microemulsions*.¹⁰⁰ In most of the cases the presence of surfactants is required to make these emulsions stable over time. However, in some cases, to avoid further complexities in the oil-water or water-oil interphases, surfactant-free approaches are used.¹⁰¹⁻¹⁰² Hereafter the principal features of the three different kind of emulsions are presented:

- Macroemulsions are kinetically stabilized for short periods (order of magnitude of hours) because of the high amount of surfactants. Furthermore, they need an energy input to be formed. The droplet size is varying from 0.1 and 10 μm .
- Microemulsions are instead thermodynamically stable, therefore they usually form spontaneously. The droplet size range is between 10 and 100 nm. The surfactant concentration is always above the critical micelle concentration (CMC), and to further decrease the interfacial tension a co-surfactant is usually present. The system is characterized by high dynamic processes, and exchange of materials between the droplets is occurring.
- Finally, miniemulsions perfectly fit in between macro- and micro-: the droplets are in the size range 50 to 500 nm. Unlike microemulsions, miniemulsions droplets are kinetically stable, but for periods usually longer than macroemulsions. Miniemulsions are characterized by high values of interfacial tension, the incomplete droplets coverage by the surfactant molecules is due to lower concentration of the surfactant (below the CMC). The droplets required high shear forces to be formed (*e.g.*, ultrasonication), where fusion and fission phenomena are occurring. The formed droplets are in a metastable state. The exchange of material between the droplets is almost absent or (ideally) suppressed (otherwise it would lead to a destabilization). Therefore, the droplets can be considered like close batch reactors.¹⁰³⁻¹⁰⁶ The stabilization mechanism of miniemulsion will be discussed in the following Section 2.3.1.

A further classification could be done considering the chemical properties of both continuous and dispersed phase. Typically, *direct emulsions* refers to oil-in-water (O/W) dispersions, and water-in-oil (W/O) emulsions are defined as *inverse emulsions*.¹⁰⁰

Depending on the chemical nature of the system considered, hydrophilic and hydrophobic monomers are polymerized in W/O and O/W emulsions, respectively. The choice of the appropriate surfactant, initiator, and hydrophobic agent is made according to the emulsion type (direct or the inverse) and to the chemical nature of the dispersed phase.

2.3.1. Stability of Miniemulsion

A miniemulsion, being a metastable state, has to be stabilized against phenomena like coalescence and Ostwald ripening. Coalescence between droplets is suppressed by the use of surfactants. Ostwald ripening (*i.e.*, the diffusion of material from smaller to bigger droplets) can be avoided by the addition of an osmotic agent (Figure 2.4).

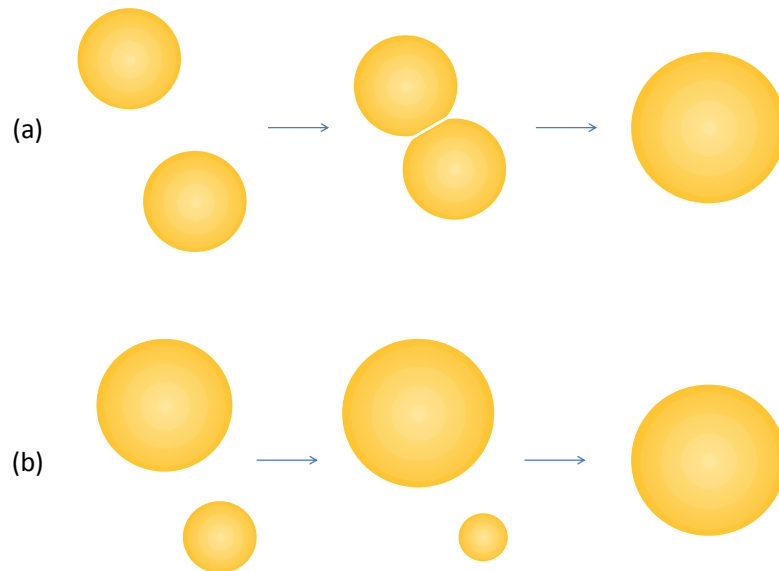


Figure 2.4. Schematic illustration of (a) coalescence and (b) Ostwald ripening in miniemulsion system.

2.3.1.1. Surfactants

A surfactant (*surface active agent*) is a substance that lowers the surface tension of the medium in which is dissolved, as well as the interfacial tension between two different phases.¹⁰⁷ Surfactants are amphiphilic molecules: they contain both water-soluble (called head) and oil-soluble (or water insoluble, called tail) moieties. Surfactants are also used as emulsifiers: they are assembled at the liquid/liquid interface, thus being able to keep separate moving droplets that collide because of Brownian motion or stirring. Surfactants can be classified in two main classes:¹⁰⁸

- *Ionic surfactants* are characterized by the presence of ionic (either anionic or cationic) heads, and they provide an electrostatic kind of stabilization. Typical

examples are sulfates, phosphates or carboxylates as anionic groups, and ammonium as cationic ones. Because of the identical surface charge between the droplets, Coulomb repulsion forces avoid droplets to collide.

- *Non-ionic surfactants*, such as block copolymers of poly(ethylene/butylene) and poly(ethylene oxide), provide instead a steric stabilization. For non-ionic surfactants, there are two main effects to produce repulsion: (i) because of the presence of a high number of polymer chains between two droplets, an osmotic pressure leads the droplets to separate; (ii) the decrease of free space and number of possible polymer chain configuration leads to a decrease of entropy.

The choice of the surfactants is done according to the type of emulsion: surfactants with a more pronounced hydrophilic and hydrophobic character are used for direct and inverse miniemulsion, respectively. The balance between the hydrophilic head and hydrophobic tail can be empirically estimated with the so-called HLB (hydrophilic-lipophilic balance) proposed by Griffin:¹⁰⁹

$$\text{HLB} = \frac{20 \cdot M_h}{M} \quad (2.1)$$

where M_h is the molecular mass of the hydrophilic part and M is the mass of the entire molecule. The HLB for non-ionic surfactants is number on a scale of 0 to 20, where 0 ($M_h = 0$) corresponds to hydrophobic and 20 ($M_h/M = 1$) to hydrophilic character. However, this method cannot be applied to ionic surfactants, where their higher hydrophilicity yield values well over 20. Therefore, the HLB value for the latter can be calculated by means of an incremental method:

$$\text{HLB} = 7 + \sum (m \cdot H) + \sum (n \cdot L) \quad (2.2)$$

where H and L are tabulated increments values, and m and n the number, for hydrophilic and lyophilic groups, respectively (*e.g.*, in case of sodium dodecyl sulfate: SO_4^- head with an H of 38.7 and twelve $-\text{CH}_2-$ groups in the tail with an L of 0.47 each, thus leading to a HLB value of 40).

As mentioned at the beginning of this section, another parameter to take into account is the so-called critical micelle concentration (CMC). The CMC is defined as the concentration above which surfactant micelles form. At concentration below the CMC, the surfactant molecules are behaving as a normal solute in the medium; instead, by increasing the concentration above the CMC, all the additional surfactant molecules

added to the system will form micelles. As a consequence, the interfacial tension decreases strongly with the increase of the surfactant concentration below the CMC, whereas above it remains nearly constant. The kinetic stabilization of miniemulsion systems is given by the concentration of the surfactant below the CMC value, thus leading to incomplete droplet coverage by the surfactant molecules.^{103, 108}

2.3.1.2. Oswald Ripening

Ostwald ripening is a thermodynamically-driven spontaneous process that leads to the diffusion of material from smaller to bigger droplets.¹⁰³ The driving force of this phenomenon is the Laplace pressure Δp_L , *i.e.* the pressure difference between the inside and the outside of a curved surface (in our case, a droplet).¹¹⁰ The Laplace pressure can also be calculated taking into account the interfacial tension γ between the two phases and the radius r of the droplet:

$$\Delta p_L = \frac{2 \cdot \gamma}{r} \quad (2.3)$$

Smaller particles are energetically less favored because of the higher Laplace pressure. Therefore, molecules in the disperse phase are molecularly diffusing from smaller droplets (higher Δp_L) to bigger droplets (lower Δp_L) through the continuous phase, until small droplets disappear in favor of the big ones.¹¹¹

In miniemulsions, where it is particularly important to suppress any exchange of material between the droplets, an osmotic agent is added. This agent has to be soluble in the dispersed phase, and it should be characterized by a stronger apolar (or polar for inverse miniemulsion) character. Considering a direct miniemulsion system, so-called ultrahydrophobes are used (*i.e.* long alkanes like hexadecane). To explain the suppression of the Ostwald ripening, let us consider the example of a miniemulsion comprised of styrene/hexadecane as a dispersed phase and a surfactant aqueous solution as a continuous phase.

Because of the higher hydrophobicity, hexadecane has a lower solubility, thus making the diffusion of styrene molecules preferential through the continuous phase. When diffusion occurs, two phenomena happen at the same time:

- Smaller droplets decrease in size: the Laplace pressure contribution tends to increase their internal pressure.

- The concentration of the osmotic agent in the smaller droplets is increasing; therefore a pressure difference, called osmotic pressure Π_{osm} , is formed between smaller (P_1, c_1) and bigger droplets (P_2, c_2):

$$\Pi_{\text{osm}} = P_1 - P_2 = R \cdot T \cdot (c_1 - c_2) \quad (2.4)$$

where P_1 and P_2 indicate the pressure of the small and big droplets, respectively; c_1 and c_2 indicate the concentration of the small and big droplets, respectively; and R is the universal gas constant.

These two opposing phenomena are then counteracting each other: smaller droplets cannot further decrease their size as far as they are not exceeding the osmotic pressure barrier.^{103, 111} As a result, the mean droplet size of the emulsion will change only slightly before stabilization against Ostwald ripening is achieved.

2.3.2. Miniemulsion Polymerization of Metal Oxocluster/Polymer Hybrids

Miniemulsion polymerization is a versatile technique to synthesized structured polymer nanoparticles and nanocapsules.¹⁰³⁻¹⁰⁵ As reported in Section 2.1.2, Stoll *et al.* in 2011 firstly reported miniemulsion as a preparative technique for polymer/oxocluster-based hybrid nanobeads.³³ The novelty of the work was the copolymerization between two type of oxoclusters, either $\text{Mn}_{12}\text{O}_{12}(4\text{-vinylbenzoate})_{16}(\text{H}_2\text{O})_4$ or the iron-substituted version $\text{Mn}_8\text{Fe}_4\text{O}_{12}(4\text{-vinylbenzoate})_{16}(\text{H}_2\text{O})_4$, with styrene as an organic comonomer. As an initiator, these authors used azobisisobutyronitrile (AIBN). Magnetic susceptibility studies confirmed that the Mn_{12} and Mn_8Fe_4 clusters retained their integrity after polymerization. Miniemulsion allowed the production of nanometer-sized paramagnetic nanobeads (~ 70 nm diameter); because of the specific dimensions, these particles presented a high potential as MRI contrast agent for magnetic resonance bioimaging.⁸⁴

Hydrophobic metal oxocluster/polymer hybrid nanoparticles can be synthesized by using miniemulsion polymerization in a two steps process (an example of direct process is shown in Figure 2.5). In the first step, two immiscible phases, namely a surfactant aqueous solution and the organic mixture (composed by metal oxocluster, organic monomer, ultrahydrophobe, and initiator), are homogenized by means of high shear forces; and after the formation of the miniemulsion, polymerization is taking place either by thermal or by photo-induced activation.

Miniemulsion droplets are acting as independent batch reactors: the polymerization is taking place independently in confined space, thus ensuring the direct formation of polymer nanoparticles with an “almost” 1:1 ratio between droplets and particles. In this way, ideally, polymerization can be initiated, propagated, and terminated in every single droplet separately. The polymerization of hybrid materials in confinement guarantees a homogeneous distribution of metal oxocluster in every droplet, and as a consequence in every hybrid/polymer particles formed. Therefore, the hybrid/polymer composition is constant in each particle. Another important parameter in case of thermo-initiated processes is the control of the temperature. In miniemulsion, the continuous phase ensures also a homogeneous heat distribution. On the other hand, in case of photo-initiated process, it is important to have an efficient stirring. Indeed, miniemulsions creates a high scattering of the incident UV light, thus decreasing the light effectively reaching the inner droplets.

Free radical polymerization associated with both direct and inverse miniemulsion techniques has been used in this thesis for the synthesis of metal oxocluster/polymer hybrid nanoparticles.

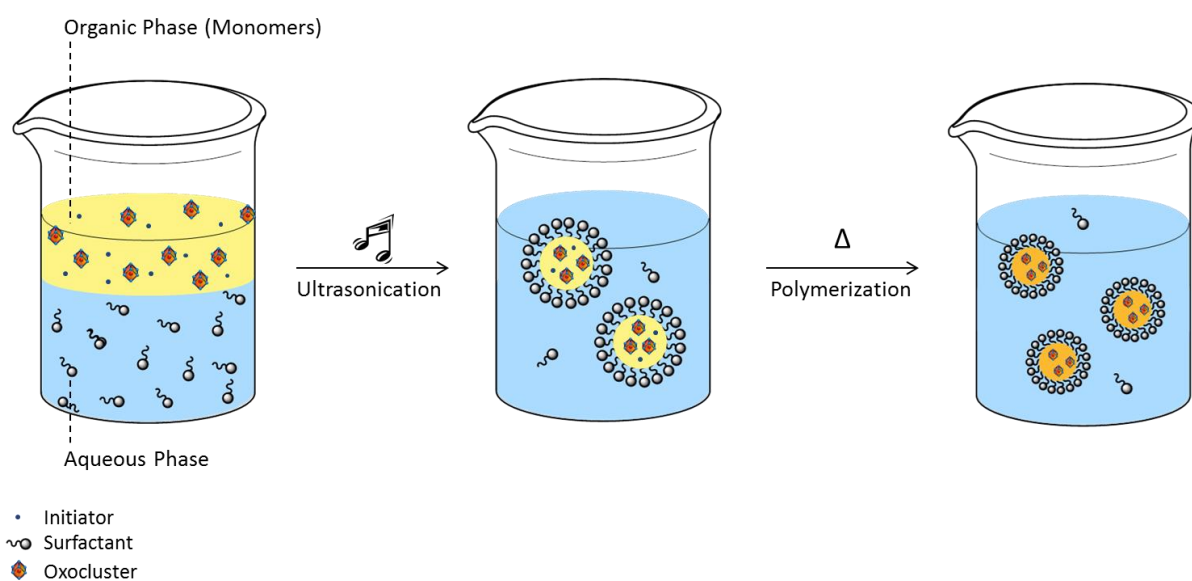


Figure 2.5. Schematic representation for the preparation of metal oxocluster/polymer hybrid nanoparticles by using miniemulsion polymerization technique.

3. Characterization Techniques

3.1. Gel Permeation Chromatography (GPC)

Gel permeation chromatography (GPC) is a size-exclusion chromatography (SEC) technique: the analytes are separated according to their size and/or molecular weight. The separation occurs through the interaction of the analytes with the porous beads of the stationary phase. As a result, smaller components can easily enter in the pores, thus having higher retention times and, consequently, be the last to be eluted. On the other hand, bigger analytes are retained for shorter times by the stationary phase and they are faster eluted.¹¹²

Herein, GPC was used for determining the amount of soluble fraction in hybrid particles cross-linked with metal oxocluster. The aim was to calculate the cross-linked particles fraction, and then to determine the efficiency of the metal oxocluster as a cross-linker. Hybrid nanoparticles with different amount of cluster were dissolved in an organic solvent (either THF or DMF for particles synthesized in direct or inverse miniemulsion, respectively), and then are centrifuged. In this way, it is possible to separate the cross-linked part, which is precipitating, from the soluble particles part which remains in the supernatant. The analysis of supernatant gives the amount of soluble fraction (Figure 3.1).

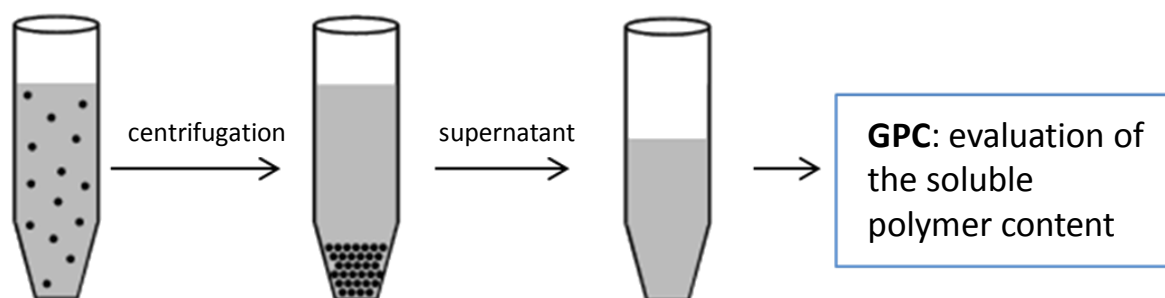


Figure 3.1. Evaluation of the soluble part content in hybrid particles cross-linked with metal oxocluster: after centrifugation the supernatant solution is analyzed by GPC.

3.2. Inductively Coupled Plasma Optical Emission Spectrometry (ICP-OES)

ICP-OES is a powerful analytical tool to quantify element traces (elemental analysis) in a variety of different sample matrices. This technique is based on the spontaneous emission of photons from atoms and ions that have been excited in a radiofrequency (RF)-induced argon plasma discharge. Liquid and gas matrix can be analyzed with ICP-OES; therefore, solid samples have to be dissolved, extracted or acid digested, thus forming a homogeneous solution. After the injection, the sample is (i) passed through a nebulizer for the formation of an aerosol and (ii) then directed to the plasma channel. At its core, the inductively-coupled plasma (ICP) sustains a temperature of approximately 10,000 K, so the aerosol is quickly dried (the solvent is removed from the droplets), vaporized, and atomized. Then, the analyte elements are present as free atoms in the gaseous state. Since enough energy is present in the plasma, further collisional excitation turn atoms into ions, and consequently both species are promoted to the excited states. The excitation is followed by a relaxation to the ground state by emission of a photon. The emitted photon is related of the quantized energy level structure for the atoms or ions: the wavelength is characteristic of the element investigated. The detection occurs by using optical spectroscopy photodetectors, such as charge coupled devices (CCDs). Finally it is possible to calculate from the total number of photons emitted the concentration of the originating element in the sample.¹¹³

The quantification of the amount of oxocluster in metal oxocluster/polymer hybrid nanoparticles was done by using ICP-OES. Hybrid particles dispersions were analyzed using the procedure developed by Vogel *et al.*¹¹⁴. Since the ICP-OES is detecting in this case the amount of metal atoms, it is important to know the exact stoichiometric structure to calculate the relative quantity of metal oxocluster present.

3.3. Electron Microscopy

The main peculiarity of an electron microscope is the resolution in the nanometer range, and, therefore, the possibility to reveal the structure of nanoparticles and nanocapsules. Because of the electron beam used as source of illumination, which has 100.000 times shorter wavelength than visible light photons, a higher resolution can be achieved. There are two main type of electron microscopy: transmission electron microscopy (TEM) and

scanning electron microscopy (SEM). TEM usually has a higher resolution and allows the investigation of the inner part of a determined system; instead SEM gives mainly information about the structure of the surface.

3.3.1. Scanning Electron Microscopy (SEM)

The scanning of a sample by using an electron focused beam that produces secondary electrons, which are finally detected, is the basic principle of SEM. In contrast to the TEM, the SEM detector is positioned sideways above the sample, thus giving the opportunity to generate a three-dimensional image of the sample surface; SEM can only scan point by point and not the whole section at once like the TEM; therefore, the image is assembled afterwards. The detected secondary electrons give information about external morphology (texture), chemical composition, and crystalline structure and orientation of the materials. Generally, the quality of the imaging depends on the signal intensity, *i.e.* on the number of emitted electrons, and on the material properties. Low voltage SEM imaging is useful to observe polymer-based nanoparticles, and also the structure of the metal oxocluster hybrid nanoparticles.

3.3.2. Transmission Electron Microscopy (TEM)

In TEM, the accelerated electron beam transmits through thin sample materials. The imaging depends on the ratio between scattered and transmitted electrons caused by the thickness and the composition of the sample. Thus, thicker parts and areas with the presence of heavier atoms (high electron density) appear darker due to the fewer electrons that reach the CCD detector.

Scanning transmission electron microscopy (STEM) is distinguished from conventional TEM by focusing the electron beam into a narrow spot which is scanned through the sample. By using a STEM it is possible to have higher contrast directly related to the atomic number and, therefore atomic resolution images can be taken. Consequently, STEM was used to detect the presence of metal oxoclusters and evaluate their distribution in the cross-section of hybrid nanoparticles, either by using dark field or bright field imaging.

3.4. X-ray Absorption Spectroscopy (XAS)

Functional properties of metal oxocluster/polymer hybrid materials are strictly related to the chemical nature of the embedded cluster. Therefore, it is crucial to ensure its structural integrity and chemical composition after the copolymerization. Generally, free radical copolymerization between metal oxoclusters and organic comonomers yields to atactic and amorphous polymers. These materials are not presenting a long-range structural order because of the small size of the cluster molecules, thus making techniques like XRD not appropriate. Therefore, conventional spectroscopic methods cannot provide any information about the retention of the cluster structure in the polymer matrix. Consequently, other spectroscopic methods need to be applied for the analysis of metal oxocluster/polymer hybrid materials, such as X-ray absorption spectroscopy (XAS). For XAS measurements, synchrotron light is needed, since they require a high intense and tunable beam. This technique can be used when there is an X-ray absorbing metal atom, and it measures the variation of the absorption coefficient of a particular atom as a function of the incident beam energy.¹¹⁵ In the context of this thesis, information about the metallic atom of the metal oxocluster embedded in the polymer matrix can be provided: geometry of surrounding atoms, atomic intermolecular distances, oxidation state, and the coordination number of the investigated atom.

X-ray absorption spectroscopy is based on the Lambert-Beer's law, that is, the intensity of a monochromatic beam passing through a homogenous sample is attenuated according to the following equation:

$$I(E) = I_0(E)e^{(-\mu(E)\cdot d)} \quad (3.1)$$

where $I(E)$ and $I_0(E)$ are the incident and transmitted X-ray intensities, $\mu(E)$ is the linear absorption coefficient, and d is the thickness of the sample. $\mu(E)$ decreases with increasing energy of the incident photon until a certain level of energy, called absorption edge, sufficient to eject a core electron is reached. Consequently, the absorption coefficient μ increases drastically and afterwards decreases monotonically again.

XAS spectra can be divided in two regions, characterized by different effects and provided information: the XANES (X-ray absorption near edge structure) region, covering the edge and the subsequent 30 eV, and the EXAFS (extended X-ray absorption

fine structure) region, starting at about 30 eV after the edge, and extending for further 800-1000 eV. The terminology XAFS (X-ray absorption fine structure) generally includes both region, even though EXAFS region is mainly dominated by single-scattering effects of the electron wave propagating through the electronic potential. In contrast, XANES is dominated by multi-scattering due to the low kinetic energy of the photoelectron.

After the X-ray absorption by the metal center of the metal oxocluster, the emitted photo-electrons collide to the neighboring atoms causing then a back scattered. Hence, these atoms have an oscillation in terms of X-ray absorption coefficient. The structure of the spectra is related to the nature, number and distances of neighboring atoms from the central atom. After the Fourier transfer of the EXAFS function, information about the surrounding of the absorbing atom can be obtained.

3.5. Dynamic Light Scattering (DLS)

Size and size distribution of nanoparticles can be measured by DLS. Suspended nanoparticles in solution are subjected to the Brownian motion. Therefore, when a laser beam is passing through a nanoparticles dispersion, the scattered light produced is subjected to intensity fluctuations. The motions of the particles depend on their size (and temperature and viscosity), so that small particles diffuse faster than bigger ones. As a consequence, the intensity due to scattering from small particles fluctuates in time more rapidly. The time autocorrelation function of the scattered intensity contains all the information about particle sizes and size distribution:

$$g^2(K; \tau) = \frac{\langle I(t)I(t + \tau) \rangle}{\langle I(t) \rangle^2} \quad (3.2)$$

where $g^2(K; \tau)$ is the autocorrelation function considering the scattering vector, K , and evolution time, τ , I is the intensity and t is the starting time. It is possible to see that at small time scales (τ), the correlation is close to one, as particles do not move much on this short time scale. For an ideal solution of monodisperse particles the function reduces to a single exponential decay described by:¹¹⁶

$$g^1(K; \tau) = e^{(-\Gamma\tau)} \quad (3.3)$$

where Γ is the relaxation rate and is connected to the translational diffusion coefficient D_t :

$$\Gamma = D_t K^2 \quad (3.4)$$

where K is the scattering vector. For diluted samples it is straightforward to assume that D_t is equal to the self-diffusion coefficient D of the microgel particles. Knowing the value of D , the hydrodynamics radius (R_h) of the scattering particle can be calculated by applying the Stokes-Einstein equation:

$$R_h = \frac{kT}{6\pi\eta D} \quad (3.5)$$

where, k is the Boltzmann constant, T the absolute temperature, η the dynamic viscosity of the system, and R_h is calculated by assuming the particles spherical (or the particles of the samples behave as if they are spheres with given R_h). The R_h value encompasses the presence of surfactants or ligands around the particles, thus influencing the layer of water dragged around by the particles.

3.6. Attenuated Total Reflectance (ATR)

Besides the standard Fourier transform infrared spectroscopy (FTIR), in Section 4.3 infrared spectroscopy in attenuated total reflection (ATR) mode has also been used. ATR allowed the direct analysis on drops deposited on the ATR crystal. The ATR crystal has a higher refractive index than the sample, thus allowing the reflection of the beam for several times before reaching the detector. The samples reflection forms the evanescent wave that penetrates into the sample. Penetration depths are usually in the range of 0.5 and 2 micrometers, and can be calculated taking into account the wavelength of the light, the angle of incidence, and the refraction indices of the ATR crystal and the sample. The outgoing light can be processed with Fourier transform to obtain infrared absorption spectra.

Precisely, ATR was used to evaluate the polymerization kinetics of PMMA and metal oxocluster/polymer hybrid nanoparticles synthesized with both thermal- and photo-initiate polymerization.

4. Results and Discussion

4.1. Dual Role of Zirconium Oxoclusters in Hybrid Nanoparticles: Cross-Linkers and Catalytic Sites^v

Organic–inorganic hybrid nanoparticles are prepared by free radical copolymerization of methyl methacrylate (MMA) with the structurally well-defined methacrylate-functionalized zirconium oxocluster $Zr_4O_2(\text{methacrylate})_{12}$. The polymerization process occurs in the confined space of miniemulsion droplets, which provides a certain degree of control on size and size distribution of the resulting hybrid particles. The formation of covalent chemical bonds between the organic and the inorganic counterparts provides structural stability and improves the distribution of the guest species (oxoclusters) in the polymer particles, overcoming problems related to migration and leaching. Because of the presence of a high number of double bonds (12 per oxocluster), the oxoclusters act as efficient cross-linking units for the resulting polymer matrix, thus ruling its swelling behavior in organic solvents. Moreover besides being a cross-linker unit, the oxoclusters act also a catalytic site for the oxidation of an organic sulfide to the corresponding sulfoxide and sulfone by activation of hydrogen peroxide (Figure 4.1). Therefore, the synthesized hybrid nanostructures are applied as heterogeneous systems, displaying quantitative sulfide conversion in 4–24 h, with overall turnover numbers (TON) up to 8000 after 4 catalytic cycles.

4.1.1. Introduction

The desulfurization of gasoline is a crucial step in the oil refinery process, since sulfur-containing compounds are responsible for the emission of the harmful air pollutant SO_2 after the combustion.¹¹⁷⁻¹¹⁸ Currently, the hydrodesulfurization (HDS), consisting in a hydrogen-based reduction at high operating temperature and pressure, is the mostly used process to remove sulfur from petroleum substrates. Although HDS is very efficient in

^v This section is based on the publication “Dual Role of Zirconium Oxoclusters in Hybrid Nanoparticles: Cross-Linkers and Catalytic Sites” by Cesare Benedetti, Alessandro Cazzolaro, Mauro Carraro, Robert Graf, Katharina Landfester, Silvia Gross, and Rafael Muñoz-Espí published in 2016 in *ACS Applied Material and Interfaces*, volume 8, issue 39, pages 26275-26284; DOI: 10.1021/acsami.6b07023. Copyright © 2016 American Chemical Society

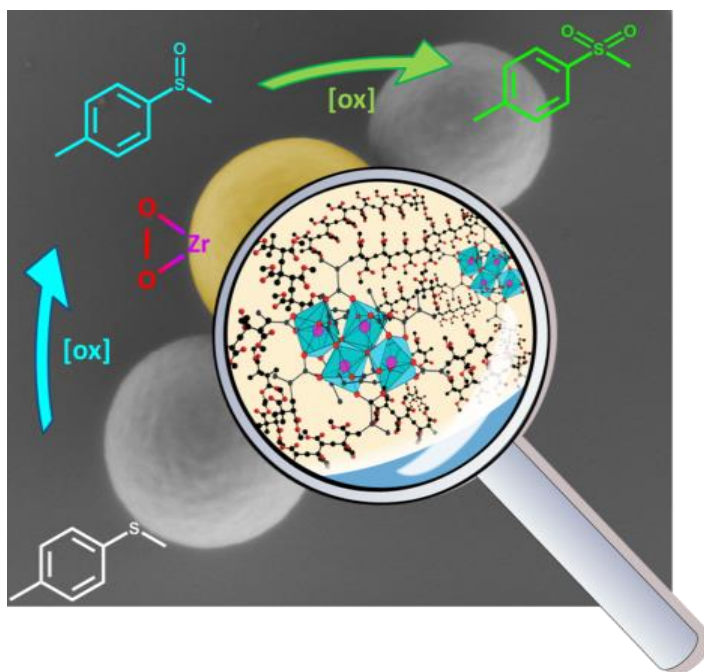


Figure 4.1. Schematic illustration of the dual role of $Zr_4O_2(\text{methacrylate})_{12}$ in hybrid nanoparticles: cross-linker and catalytic site.

the low-boiling petroleum fractions, its efficacy is drastically decreased for high-boiling fractions.¹¹⁷⁻¹²⁰ In addition, sulfur based compounds are responsible for the poisoning of the noble metal catalysts and various corrosion processes during the desulfurization. As a result, the process is relatively expensive, also because of the high amount of catalysts necessary.

An appealing alternative for the removal of sulfur-containing compounds from oil substrates is represented by the use of catalytic oxidations.^{52, 93, 121-122} Owing to the different chemical properties and solubility of the oxidized products (sulfoxides and, in particular, of sulfones), these can be efficiently removed by solvent extraction or upon distillation of the fuel.

It has been widely reported that complexes containing early transition metals in their highest oxidation state (d^0) display interesting catalytic properties.¹²³⁻¹²⁵ They have been shown to activate hydrogen peroxide or organic peroxides and promote the oxidation of different substrates, such as olefins, sulfides, sulfoxides, and alcohols.¹²⁶⁻¹³¹ A process based on the oxidation of sulfur compounds using peroxide would be more environmental friendly and based on milder conditions (especially in term of lower temperature and pressure) compared to the HDS.

The application of zirconium-based oxoclusters for the homogeneous catalytic oxidation of sulfur-based substrates, in the presence of hydrogen peroxide, has been already reported by Faccioli *et al.*⁵². However, the oxoclusters showed low oxidative and

hydrolytic stability under the explored conditions. Therefore, embedding into a polymer matrix was used to enhance inherent stability of the catalytically active species. The heterogenization of zirconium oxoclusters into a polymeric bulk matrix has been recently demonstrated to increase their overall stability, thus increasing their catalytic performances and enabling recovery and recycling.⁹³

A step further in this framework would be to pursue a better control on the catalytic process by enhancing dispersibility of the hybrid catalyst. To accomplish this task, the use of colloidal-based method was explored. This PhD work is based on the use of miniemulsion polymerization as a versatile technique³⁰⁻³⁷ to produce hybrid nanoparticles. In particular in this section is reported the incorporation of functional Zr-based oxoclusters acting both as oxygen transfer catalysts as well as structural BB, with tunable behavior in terms of dimensions, cross-linking degree, and swelling. The successful radical copolymerization between the oxocluster $\text{Zr}_4\text{O}_2[\text{O}(\text{C}(\text{CH}_3)=\text{CH}_2)]_{12}$ (in the following labeled as **Zr₄**)⁴⁷ and methyl methacrylate in a direct (oil-in-water) miniemulsion system was performed, and the resulting materials thoroughly characterized. The oxocluster was chosen based on the promising catalytic performances shown by **Zr₄**-based bulk hybrid materials in heterogeneous oxidation reactions.⁹³ The dispersed monomer droplets, stabilized by nonionic or anionic surfactants, act as independent confined nanoreactors and are ideally converted into particles after polymerization. The synthesized hybrid systems, featuring higher surface area and an enhanced dispersibility, are applied as nanosized heterogeneous catalysts for the oxidation of an organic sulfide to the corresponding sulfoxide and sulfone by hydrogen peroxide.

4.1.2. Particle Synthesis and Composition

After the synthesis of inorganic comonomer **Zr₄** by reaction of zirconium butoxide with methacrylic acid (as reported in the experimental Section 6.1.2), cross-linked hybrid poly(MMA-*co*-**Zr₄**) nanoparticles were prepared by free radical copolymerization performed in miniemulsion (Figure 4.2).

Different amounts of **Zr₄** (1, 3, 5, 7 and 10 wt%) and two different surfactants (the anionic sodium dodecyl sulfate, SDS, and the nonionic Lutensol AT50) were used (Table 4.1). The concentration of surfactant was chosen to have similar sizes of the final

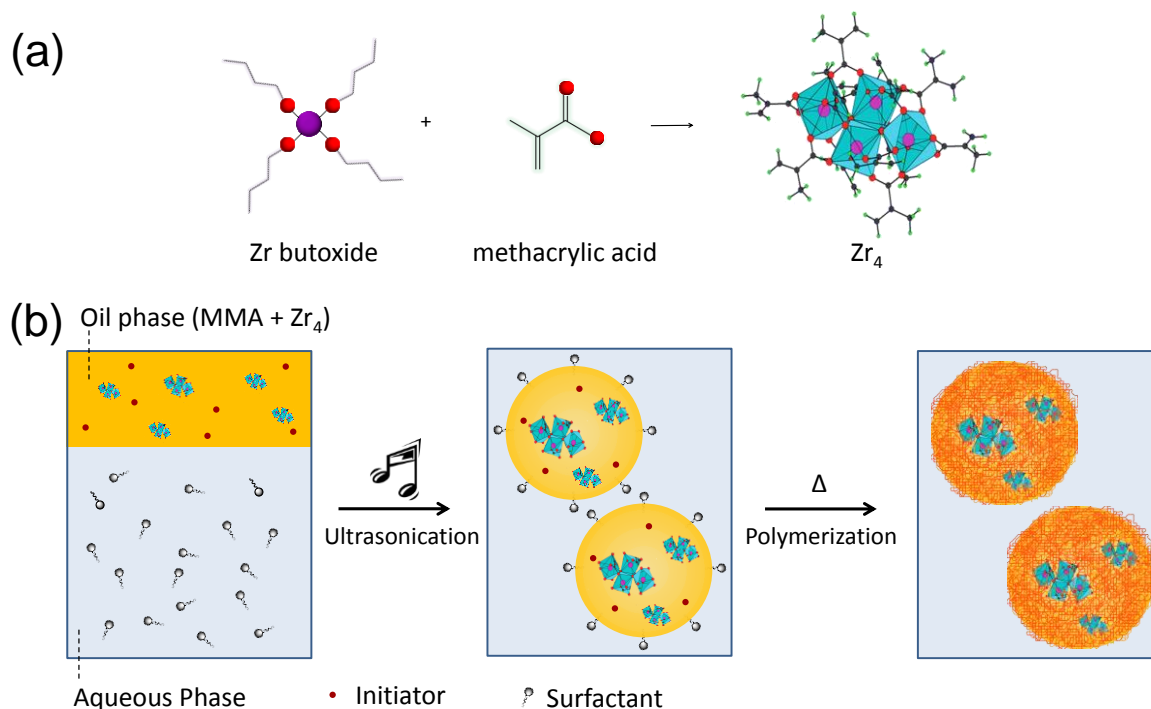


Figure 4.2. Preparation of the cross-linked hybrid poly(MMA-*co*-Zr₄) nanoparticles: (a) synthesis of zirconium oxocluster Zr₄O₂(methacrylate)₁₂, (b) copolymerization with MMA in miniemulsion droplets.

particles, taking into account that the critical micelle concentrations of both surfactants are different.¹³²

To assess the composition of the hybrid materials, a first investigation was performed by using infrared vibrational spectroscopy. FTIR spectra of pristine Zr₄, PMMA and hybrid nanoparticles are reported in Figure 4.3. Either by using SDS or Lutensol AT50 as surfactant, the spectra of the hybrid particles contain both the signal of Zr₄ and PMMA particles.

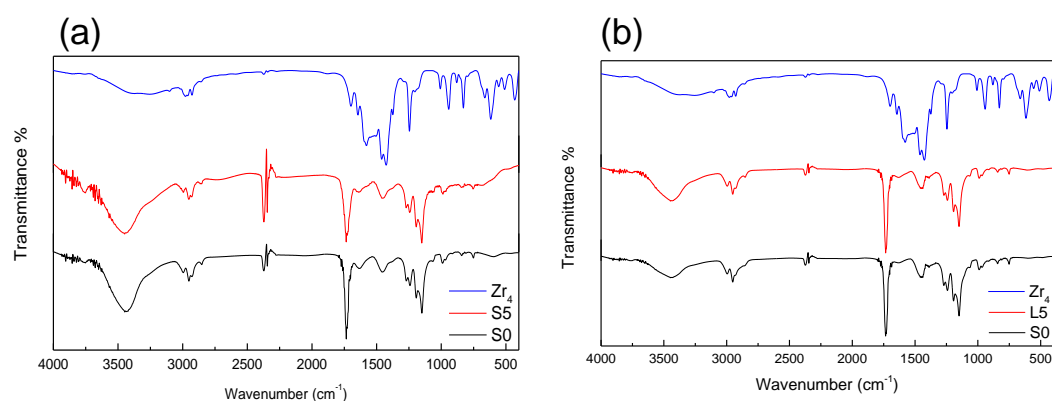


Figure 4.3. FTIR spectra of (a) Zr₄, S0, S5 and (b) Zr₄, L0, L5.

Table 4.1. Synthetic details for the preparation of poly(MMA-*co*-Zr₄) nanoparticles.

Samples ^a	Surfactant	Zr ₄ content as comonomer (wt%)	Actual Zr ₄ content (wt%) ^b
S0	SDS	0	0
S1	SDS	1	0.7 ± 0.5
S3	SDS	3	3.2 ± 0.4
S5	SDS	5	4.6 ± 0.5
S7	SDS	7	6.9 ± 0.5
S10	SDS	10	10.5 ± 0.5
L0	Lutensol AT50	0	0
L1	Lutensol AT50	1	0.9 ± 0.4
L3	Lutensol AT50	3	2.2 ± 0.4
L5	Lutensol AT50	5	4.3 ± 0.4
L7	Lutensol AT50	7	6.6 ± 0.4
L10	Lutensol AT50	10	6.6 ± 0.5

^[a] The letters in the sample codes refer either to Lutensol AT50 (**L**) or to SDS (**S**), used as surfactants; the numbers refer to the Zr₄ weight percent (*e.g.*, **S1** represents the sample prepared with SDS and 1 wt% of Zr₄). ^[b] Determined by ICP-OES.

A main issue in this case was to assess whether and to which extent the oxocluster was effectively incorporated in the hybrid matrix. Therefore, after polymerization, the actual content of Zr₄ in the synthesized hybrid nanoparticles was determined by inductively coupled plasma optical emission spectrometry (ICP-OES).¹¹⁴ In Figure 4.4, the starting amounts of Zr₄ (as a comonomer) are plotted against the contents detected in the hybrid nanoparticles. While the detected values of zirconium content are consistent with the initially introduced oxocluster for contents up to 10 wt% for the case of SDS, in the case of Lutensol AT50 the sample prepared with 10 wt% of oxocluster (sample **L10** in Table 4.1) showed approximately the same amount as for the one prepared with 7 wt% (sample **L7**), indicating that a maximum incorporation was reached.⁹⁹ The lower stability when using Lutensol AT50 is confirmed by the higher amount of coagulum formed during the polymerization (ca. 9.4 wt% with respect to the monomer content, with a content of Zr₄ around 40 wt% for sample **L10**), in comparison with the corresponding sample with SDS (ca. 5.2 wt%).

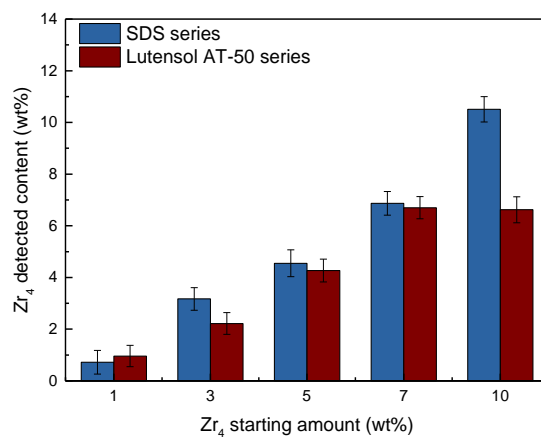


Figure 4.4. Zr₄ content detected by elemental analysis (ICP-OES) of hybrid poly(MMA-*co*-Zr₄) nanoparticles prepared using either SDS or Lutensol AT50 as surfactants.

4.1.3. Morphology and Structure

The droplet stabilization in the system is not only affected by the different nature of the surfactants, but also by the amount of Zr₄ oxocluster. A systematic increase of size is observed with increasing amounts of Zr₄, as shown by dynamic light scattering (DLS, Table 4.2 and Figure 4.5) and scanning electron microscopy (SEM) measurements (Figure 4.6). The increase of particle size and polydispersity at higher amounts of Zr₄ can be explained by considering that the oxocluster, likely interacting with the surfactants, lowers the efficiency of the latter in stabilizing the miniemulsion. Accordingly, an increase of average particle size was observed.¹⁰⁴

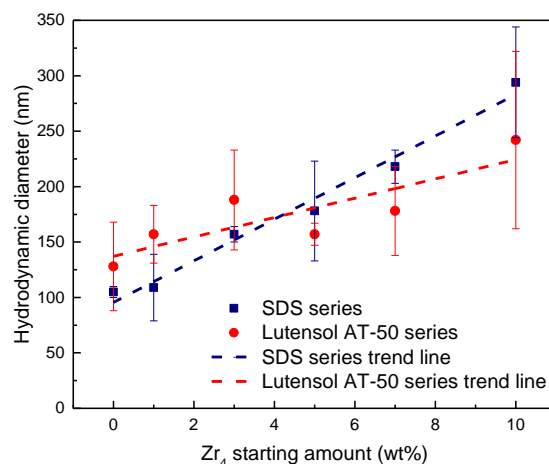


Figure 4.5. DLS measurement of the water suspension as a function of the hydrodynamic diameter of hybrid poly(MMA-*co*-Zr₄) nanoparticles prepared using either SDS or Lutensol AT50 as surfactants.

Table 4.2. Main features of the cross-linked hybrid poly(MMA-*co*-Zr₄) nanoparticles.

Samples	Hydrodynamic diameter in water (nm) ^a	Hydrodynamic diameter in acetonitrile (nm) ^a	Hydrodynamic diameter in THF (nm) ^a	Cross-linked fraction (wt%) ^b
S0	105 (±6%)	-	-	0
S1	109 (±28%)	-	-	6 ± 4
S3	157 (±5%)	-	481 (±22%)	39 ± 2
S5	178 (±27%)	-	456 (±26%)	79.9 ± 0.2
S7	218 (±7%)	-	559 (±26%)	90.5 ± 0.4
S10	294 (±18%)	-	610 (±13%)	96.5 ± 0.3
L0	128 (±32%)	-	-	0
L1	157 (±16%)	279 (±28%)	-	10 ± 3
L3	188 (±26%)	333 (±23%)	680 (±12%)	29 ± 4
L5	157 (±8%)	284 (±29%)	463 (±31%)	33 ± 4
L7	178 (±26%)	306 (±16%)	621 (±31%)	50 ± 1
L10	242 (±34%)	498 (±23%)	791 (±8%)	51 ± 2

^[a] Determined by DLS; ^[b] determined by GPC on supernatants.

The distribution of the oxoclusters within the particles was evaluated by transmission electron microscopy (TEM). The samples with the highest oxocluster content were chosen to highlight the different oxocluster incorporation (samples **S10** and **L10**; Figure 4.7, panels *a* and *b*, respectively). The dark spots in the bright-field images are due to the presence of heavier atoms of the inorganic comonomer (because of the lower electron transmission), indicating the areas with a higher concentration of Zr₄. In addition, scanning transmission electron microscopy (STEM) dark-field images of the same sample positions (Figure 4.7c–d) show the zirconium distribution in the nanoparticles hybrid matrix. **S10** is characterized by an even distribution of Zr₄ inside the polymer matrix, with a higher concentration at the particle surface. In contrast, when using Lutensol AT50 (**L10**), the oxocluster is not homogeneously distributed in the particle network, but it forms aggregates within their cores. The different distribution of Zr₄ within the nanoparticles matrix is due to the different interaction with the two surfactants as reported in Section 4.1.7.

A further relevant issue in this case was also to assess that the oxocluster, *i.e.* the catalytically active species, was retaining its structural stability upon embedding into the polymer matrix. X-ray absorption spectroscopy (XAS) is an effective analytical tool to investigate the structural preservation of the oxocluster.¹³³ In case of structural

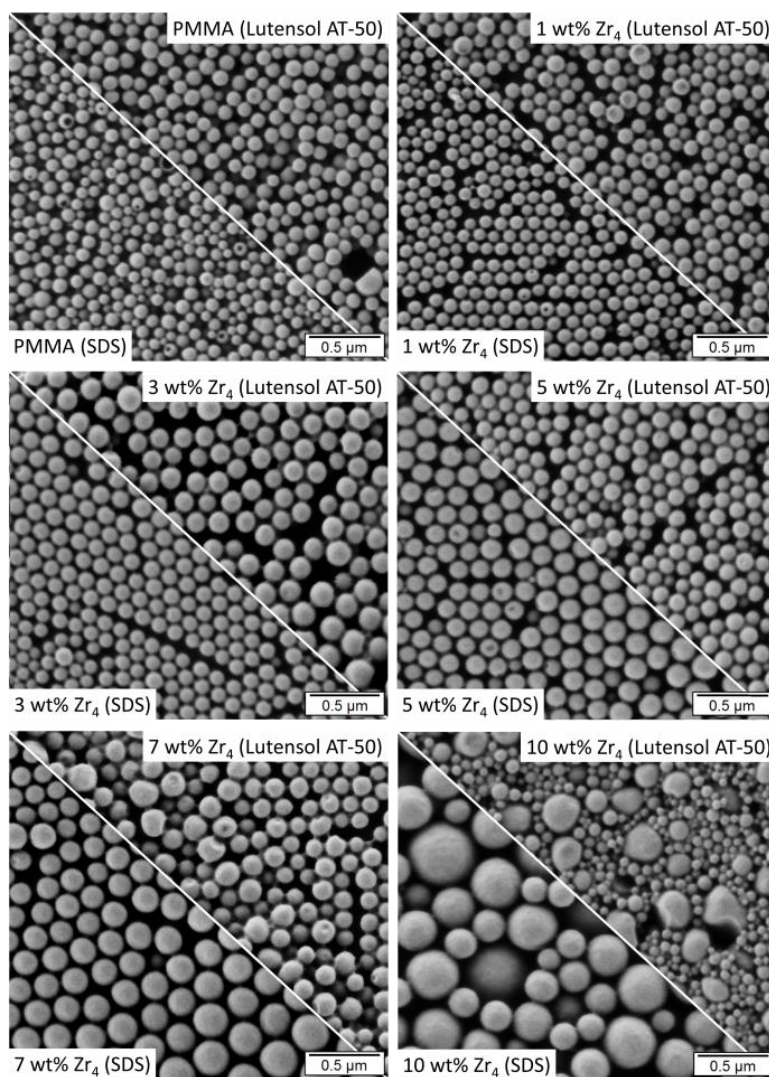


Figure 4.6. SEM images of hybrid poly(MMA-*co*-Zr₄) nanoparticles prepared using either SDS or Lutensol AT50 as surfactants.

modification (*e.g.*, decomposition, formation of oligomers), significant variations would be observed in the corresponding XAS spectra. To confirm the structural integrity of the Zr₄ oxocluster after the polymerization, the hybrid poly(MMA-*co*-Zr₄) nanoparticles were analyzed by X-ray absorption measurements at Zr K-edge and the spectral output compared with that of pristine Zr₄ oxocluster. Fourier transforms of the X-ray absorption fine structure (EXAFS) region of the collected spectra for the samples prepared with different contents of Zr₄, compared to the pristine oxocluster, are shown in Figure 4.8. The difference between the reference Zr₄ and L3 is minimal, which indicates that there is no relevant distortion in the oxocluster structure upon embedding. For sample S3, a small contraction in the first shell distance (corresponding to the Zr–O coordination polyhedra) and a broader peak are observed (Figure 4.8a). The hybrid samples L5 and L7 and the

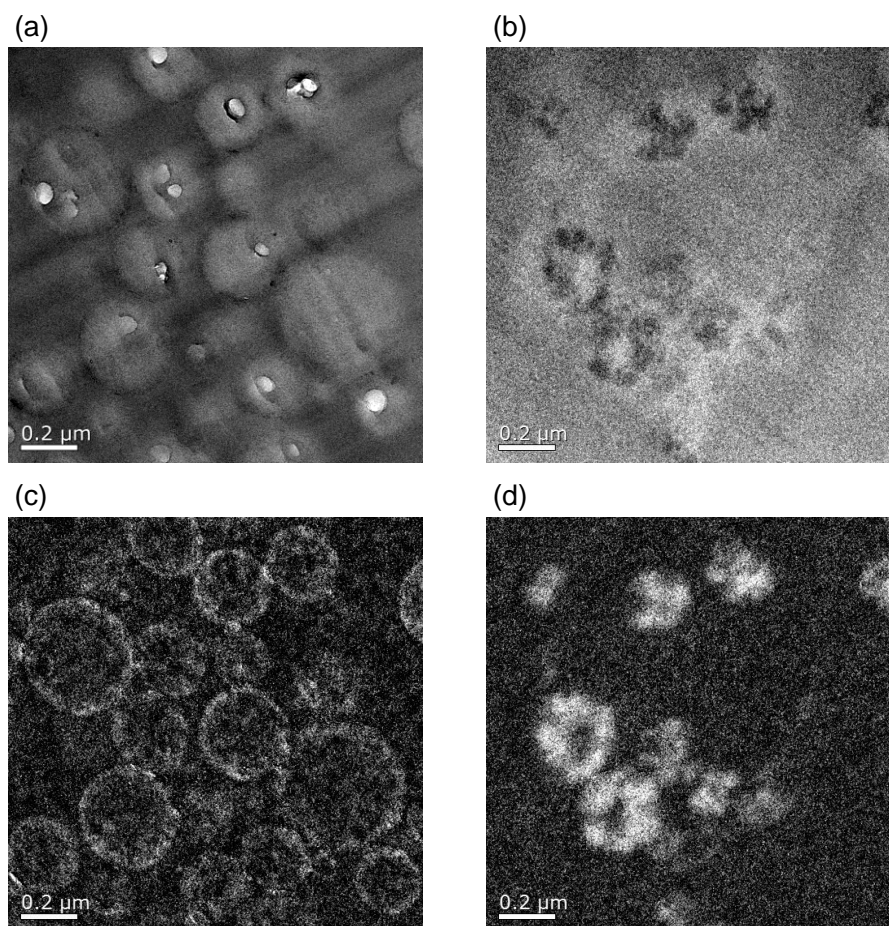


Figure 4.7. TEM images of hybrid poly(MMA-*co*-Zr₄) nanoparticles with 10 wt% of Zr₄. Bright field images of (a) sample **S10** and (b) sample **L10** and corresponding zirconium mapping (c) and (d), respectively. (The white spots in panel (a) are due to measuring artifacts caused by the cutting procedure).

analogous samples prepared with SDS (samples **S5** and **S7**) show a coherency with the samples prepared using the 3 wt% of Zr₄ (Figure 4.8b and 7c, respectively). This result is an indication that in the SDS samples the zirconium atoms in the embedded oxocluster have a more disordered environment in the first Zr–O coordination shell, with slightly distorted coordination geometry and slightly longer bond lengths with respect to the pure oxocluster and to the samples obtained with Lutensol AT50, which however are still compatible with those of the pristine oxocluster. In fact, though this minor distortion, the second shell (at roughly 3.5 Å, corresponding to Zr–Zr bond lengths) of the embedded samples closely resembles the one of the pure oxocluster (indeed, the coordination number and distances of the further zirconium atoms are nearly unchanged), thus suggesting that the oxocluster has retained its structure upon embedding. In contrast, for samples prepared with the highest amount of oxocluster (**S10** and **L10**), there is a slight increase in the first shell distance for both the samples, witnessing some distortion for both samples (Figure 4.8d).

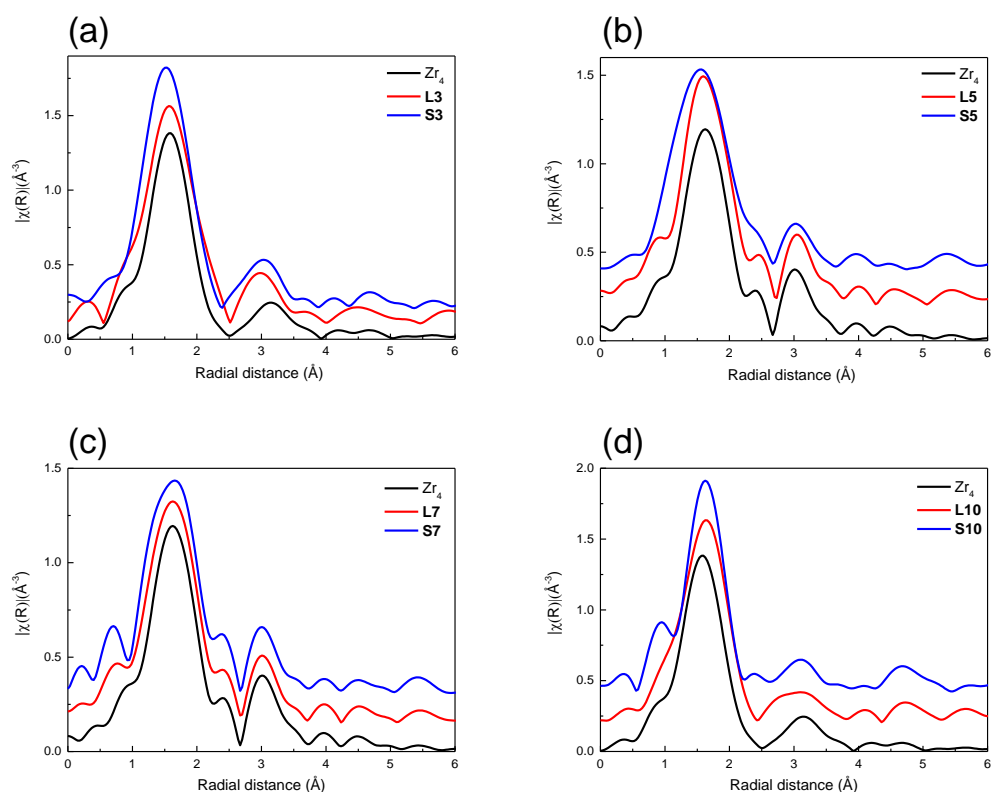


Figure 4.8. Fourier transforms of the EXAFS spectra for the cross-linked hybrid poly(MMA-*co*-Zr₄) nanoparticles compared to the Zr₄ as a reference. The samples with (a) 5 wt% and (b) 10 wt% of Zr₄ (synthesized using either SDS or Lutensol AT50 as surfactants) are shown.

X-Ray photoelectron spectroscopy (XPS) analyses were performed on samples **L7** and **S7** to assess whether the bulk and the surface composition of the prepared materials are the same, which is a relevant information for applications in catalysis. XPS is indeed a highly surface sensitive method (the mean free path of outgoing electrons is typically less than 10 nm) that provides a compositional characterization of the surface of a sample. The detected atomic percentages are reported in Table 4.3. The experimental values for Zr are slightly lower than those calculated on the basis of the nominal composition of the formulation (i.e., 0.1 instead of 0.3 at. %). However, the results can be rationalized considering that the error is relatively high for such a low amount and that the surface of the particles is still partially covered by surfactants molecules. It can be also observed that, in both analyzed samples, the carbon and oxygen contents are much higher than the expected ones based on nominal compositions of the starting formulation, which can be again ascribed to the presence of the surfactant.

Table 4.3. Atomic percentages obtained by XPS. In brackets: theoretical values.

Samples	%C	%O	%Zr
L7	73.6 (66.3)	26.4 (33.4)	0.1 (0.3)
S7	75.2 (66.3)	24.7 (33.3)	0.1 (0.3)

4.1.4. Cross-Linking, Swelling, and Thermal Properties

Freeze-dried nanoparticles were redispersed in THF and then centrifuged. The sedimentation of the cross-linked nanoparticles allows the evaluation of the soluble fraction in the supernatant by gel permeation chromatography (GPC). Figure 4.9 and Table 4.2 report the calculated insoluble cross-linked fraction of poly(MMA-*co*-**Zr₄**) nanoparticles (freeze-dried) as a function of **Zr₄** content. A general increase in the cross-linked fraction is observed at higher amounts of **Zr₄** in the nanoparticles, which is in agreement with previous work reporting an increase of cross-linking with increasing amount of oxocluster.⁴⁷ A higher cross-linking efficiency is observed using SDS, and complete cross-linking can be observed for **S10**. This result is in agreement with a recently published work of Kreutzer *et al.*⁹⁹, in which a cluster amount higher than 10 wt% represents a cross-linker overloading. In contrast, for Lutensol AT50 the cross-linking efficiency is about half of that observed for SDS at the highest **Zr₄** content; a plateau region is observed after 7 wt%, which is related with the maximum incorporation of oxocluster according to ICP-OES results. The lower cross-linking efficiency using Lutensol AT50 is explained by the lower and less homogeneous incorporation of **Zr₄** within the hybrid nanoparticles, as shown by ICP-OES and STEM results.

The cross-linking extent of **Zr₄** in the freeze-dried samples **S3**, **S5**, and **S7** was estimated through the quantitative evaluation of the relative amount of **Zr₄** free (unreacted) double bonds on the prepared hybrid poly(MMA-*co*-**Zr₄**) nanoparticles by means of solid-state NMR spectroscopy. ¹³C CP-MAS NMR spectra of non-copolymerized mixtures of **S0** and **Zr₄**, in the same weight ratio as **S3**, **S5** and **S7**, were also analyzed. The broad signal at about 18 ppm arises from the superposition of the intrinsically broad methyl signal of PMMA and the narrow one of **Zr₄**. The main chain signals of PMMA appear between 40 and 60 ppm, together with that of the methoxy carbon. Two weak ¹³C NMR signals, at 125 and 140 ppm, can be assigned to the olefinic carbons of **Zr₄**. The COO ester group of PMMA is observed at 178 ppm. The

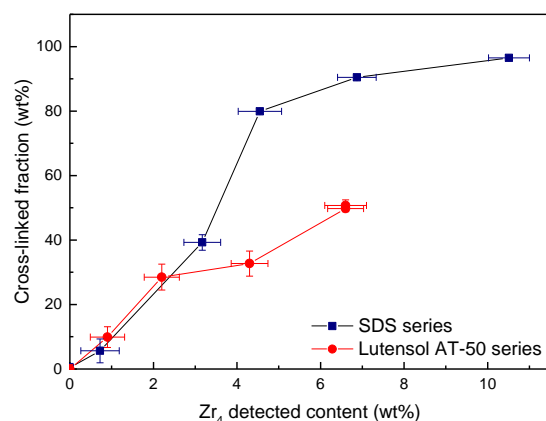


Figure 4.9. The poly(MMA-*co*-Zr₄) nanoparticles cross-linked fraction as a function of the Zr₄ detected content through ICP-OES. The cross-linked fraction was determined as the inverse of the soluble fractions, the latter being obtained through GPC on the supernatants. The cross-linker efficiency and the incorporation of Zr₄ are higher using SDS as a surfactant.

comparison NMR spectra of hybrid poly(MMA-*co*-Zr₄) nanoparticles with the NMR spectra of pristine Zr₄ and S0 provides information on the modifications occurring upon hybrid formation. PMMA signals in the spectra of the hybrid and of pristine polymer appear substantially identical, indicating the similarity of the main structural features of PMMA in the presence or absence of the oxoclusters. In the spectrum of the pristine oxocluster Zr₄ every signal corresponding to a certain carbon nucleus appears structured in a variable number of peaks. Because of the low amount of oxoclusters embedded in the hybrid materials, their signals are largely decreased in intensity, and the spectral resolution between different sites of the oxoclusters is almost completely lost due to local heterogeneities of the hybrid materials.

Finally, the NMR signals of the free Zr₄ double bonds observed at 140 ppm were evaluated by integration and normalized to the signal of the COO ester group of PMMA at 178 ppm. The signals of S3, S5, and S7 are compared with the ones of the unreacted mixtures containing S0 in addition to 3, 5, and 7 wt% of Zr₄, respectively. Since, the mixtures of S0 and Zr₄ have not been polymerized, the signal intensity of the Zr₄ double bonds are considered fully unreacted. The amount of reacted Zr₄ double bonds can be estimated from the ratio between signal intensities in the hybrid samples and in the mixture.

The comparison of the spectra of the hybrid samples with the non-polymerized mixtures shows that all polymerized hybrid samples have an amount of Zr_4 free double bonds in the range ~35–60% (Figure 4.10 and Table 4.4)

Table 4.4. Evaluation of the unreacted double bonds through ^{13}C CP-MAS.

Content of Zr_4 (wt%)	Poly(MMA-co- Zr_4) nanoparticles (%)	Mixture of Zr_4 and $S0$ nanoparticles (%)	Unreacted Zr_4 double bonds (%)
3	0.47 (S3)	1.05	45%
5	1.04 (S5)	3.02	35%
7	0.97 (S7)	1.60	60%

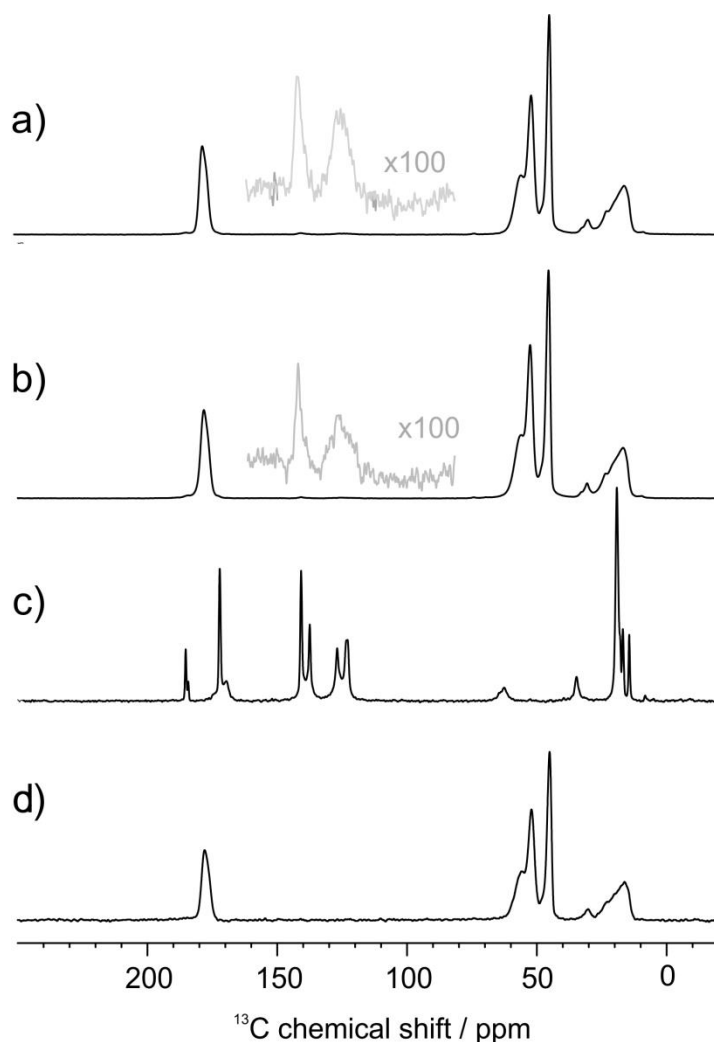


Figure 4.10. ^{13}C CP-MAS spectra of (a) a mixture of $S0$ (PMMA nanoparticles) and Zr_4 5%, (b) $S5$, (c) Zr_4 oxocluster and (d) $S0$.

Pristine PMMA and hybrid poly(MMA-*co*-**Zr₄**) nanoparticles present relevant structural differences, which is reflected in their swelling behavior. The linear structure of PMMA allows its solubilization in different organic solvents (*e.g.*, acetonitrile, THF, ethyl acetate or DMSO), whereas the cross-linked poly(MMA-*co*-**Zr₄**) particles are not soluble and swell in such solvents. As already observed for the homologues hybrid bulk materials,⁴⁷ the degree of swelling depends on the content of **Zr₄**, which influences the reticulation of the polymer chains. The swelling behavior of the freeze-dried particles was determined by DLS in water, THF, and acetonitrile. In acetonitrile, only samples prepared with Lutensol AT50 were studied, since the samples prepared by SDS do not yield stable dispersions to allow DLS measurements. The swelling behaviors in water, acetonitrile, and THF are reported in Figure 4.11 and Table 4.2. Because of the hydrophobic character of the polymeric matrix, for all hybrid samples an increase of the particle diameter in acetonitrile or THF is observed with respect to the diameters in water. Concerning the swollen particles in THF, the particles synthesized using SDS present a smaller diameter with respect to the Lutensol AT50 series. The lower swelling of SDS particles is due to a higher and more efficient cross-linking, thus resulting in a more rigid structure with a lower capability to uptake solvent.⁴⁷

The copolymerization of MMA with **Zr₄** affects the thermal properties. The glass transition temperature (T_g) was analyzed through differential scanning calorimetry (DSC). The zirconium cross-linkers increase the glass transition temperature of the nanoparticles polymer matrix, as shown in Figure 4.12. The T_g of PMMA particles (as dried sample) synthesized in miniemulsion under the reported conditions is around 100 °C, which is lower than the atactic PMMA synthesized in bulk conditions (105 °C) because of the presence of additives used in the miniemulsion polymerization (hexadecane, surfactant, remains of the initiator, etc.).³⁷ In **S1** the T_g increases about 6 °C, and at the highest amount of oxocluster it reaches 111 °C (**S10**). T_g measurements of the samples synthesized with Lutensol AT50 are affected by the plasticizer activity of the additives. Indeed, polyethylene glycol ethers have been reported to act as plasticizers.¹³⁴

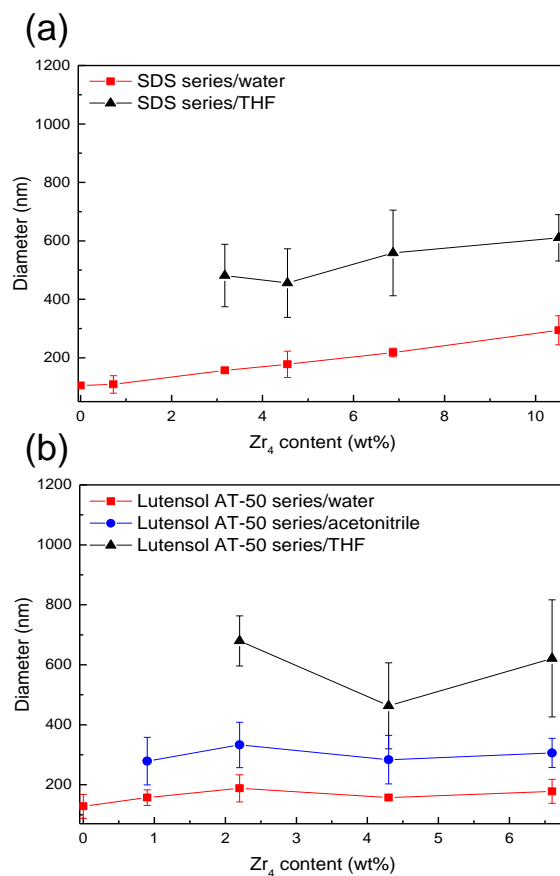


Figure 4.11. DLS measurement of the hydrodynamic diameter of hybrid poly(MMA-*co*-Zr₄) nanoparticles (a) in water and THF for SDS samples and (b) additionally in acetonitrile for Lutensol AT50 samples as a function of Zr₄ content.

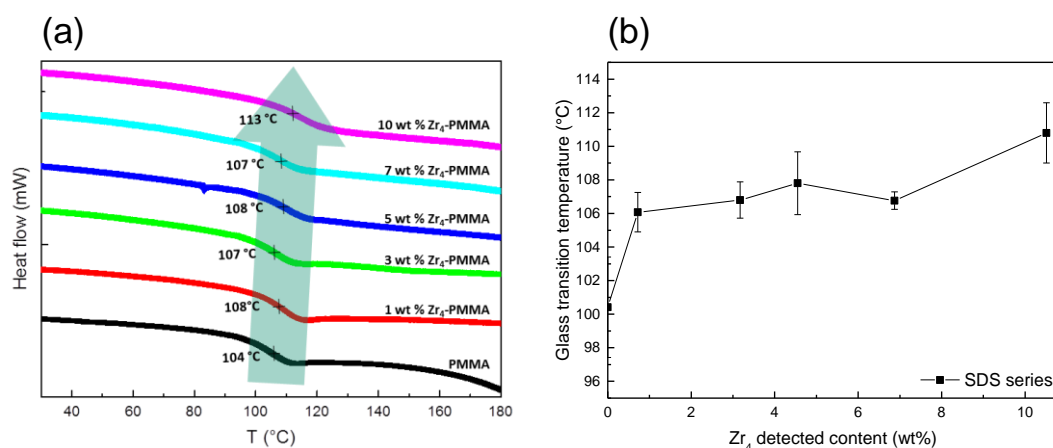


Figure 4.12. DSC curves (a) and glass transition temperature as a function of the Zr₄ content (b) of hybrid poly(MMA-*co*-Zr₄) nanoparticles prepared with SDS. The glass transition temperature of the samples shown is calculated from the first derivative.

4.1.5. Catalysis: Oxidation of Methyl *p*-Tolylsulfide

The hybrid poly(MMA-*co*-Zr₄) nanoparticles were tested for the two-step oxidation of methyl *p*-tolylsulfide (S) to the corresponding sulfoxide (SO) and sulfone (SO₂) by hydrogen peroxide (Scheme 4.1). The oxidations occur in 4–24 h, with turnover numbers (TON) up to 2000 and a marked selectivity toward the formation of the sulfone (Figure 4.13 and Figure 4.14). Peroxides coordinated to Zr oxocluster, indeed, display an high reactivity toward sulfoxide oxidation,⁵² and this selectivity is further enhanced by the presence of the polymeric matrix, owing to the higher affinity for the oxidized substrates.^{93, 122} The internal catalytic sites are still accessible in the supported catalyst due to the swelling of the polymer matrix in acetonitrile (catalysis medium), which enables the diffusion of both substrate and H₂O₂. As a result of this synergistic behavior, a faster conversion to the sulfone can be obtained.

Yield, selectivity, total turnover number (TON, number of converted moles of H₂O₂ per mole of catalyst), turnover frequency (TOF, catalytic cycles per minute), kinetic constants (k_1 and k_2) are listed in Table 4.5.

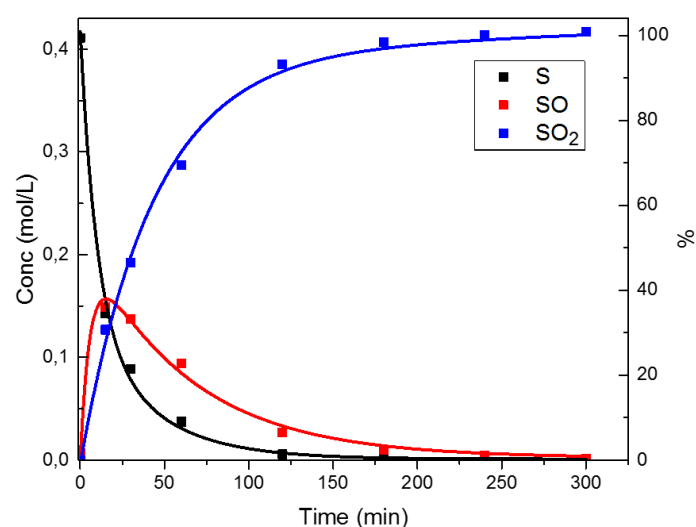
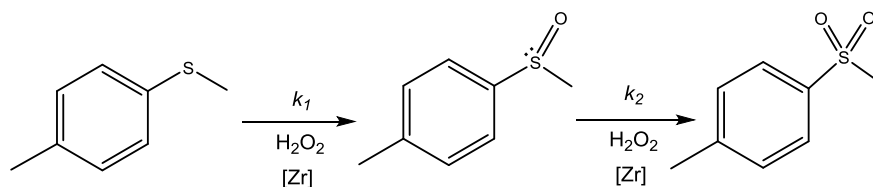


Figure 4.13. Kinetic trace for the oxidation of methyl *p*-tolyl sulfide (S, black squares) to its sulfoxide (SO, red squares) and sulfone (SO₂, blue squares) by hydrogen peroxide in the presence of **L10** as heterogeneous catalyst at 50 °C. The Zr₄ is present in 0.1 mol% with respect to the methyl *p*-tolyl sulfide. The continuous lines show second order kinetic fittings.



Scheme 4.1. Oxidation of methyl *p*-tolylsulfide to the corresponding sulfoxide and sulfone by using hydrogen peroxide as a oxidant and hybrid poly(MMA-*co*-**Zr₄**) nanoparticles as a catalyst.

Table 4.5. Oxidation of methyl *p*-tolylsulfide with H₂O₂ in the presence of Zr oxoclusters into nanoparticles.

# ^a	Samples	Conversion (SO:SO ₂) t = 1 h	Conversion (SO:SO ₂) t = 4 h	Conversion (SO:SO ₂) t = 24 h	TOF (min ⁻¹) ^b	TON (4h) ^c	k_1 (M ⁻¹ s ⁻¹)	k_2 (M ⁻¹ s ⁻¹)	k_1/k_2
1 ^d	-	33 (100:1)	72 (100:0)	90 (100:0)	-	-			
2	S5	68 (56:44)	96 (17:83)	100 (0:100)	20	1830	4.2×10^{-4}	3.3×10^{-4}	1.3
3	S7	71 (65:35)	95 (29:71)	100 (0:100)	16	1626	5.6×10^{-4}	3.2×10^{-4}	1.8
4 ^e	S7		93 (45:55)	100 (<1:>99)		3066			
5	S10	80 (49:51)	98 (15:85)	100 (0:100)	21	1808	7.7×10^{-4}	5.9×10^{-4}	1.3
6 ^e	S10		88 (71:29)	100 (6:94)		2868			
7	L5	80 (42:58)	97 (13:87)	100 (0:100)	25	1870	8.7×10^{-4}	8.6×10^{-4}	1.0
8	L7	81 (49:51)	98 (13:87)	100 (0:100)	22	1840	9.5×10^{-4}	6.6×10^{-4}	1.4
9 ^e	L7		92 (35:65)	100 (1:99)		3360			
10	L10	91 (25:75)	100 (1:99)	100 (0:100)	28	1990	1.3×10^{-3}	1.3×10^{-3}	1
11 ^e	L10		95 (4:96)	100 (0:100)		3850			

^[a] Reaction conditions: the suitable amount of heterogeneous catalyst, to provide 0.41 mM of **Zr₄**, was added to 2.4 mL of acetonitrile containing 0.41 M of methyl *p*-tolyl sulfide and H₂O₂ (1.025 M, added from a 30% aqueous solution); T = 50°C; ^[b] number of catalytic cycles per minute (number of converted moles of substrate per mole of catalyst, per minute), measured at < 30% substrate conversion; ^[c] total turnover number (number of converted moles of substrate per mole of catalyst), after one or two reaction runs, calculated at t=4h; ^[d] blank reaction without nanoparticles. A similar result was obtained upon addition of oxocluster-free polymeric nanoparticles; ^[e] recycled catalyst (after a first 24 h run).

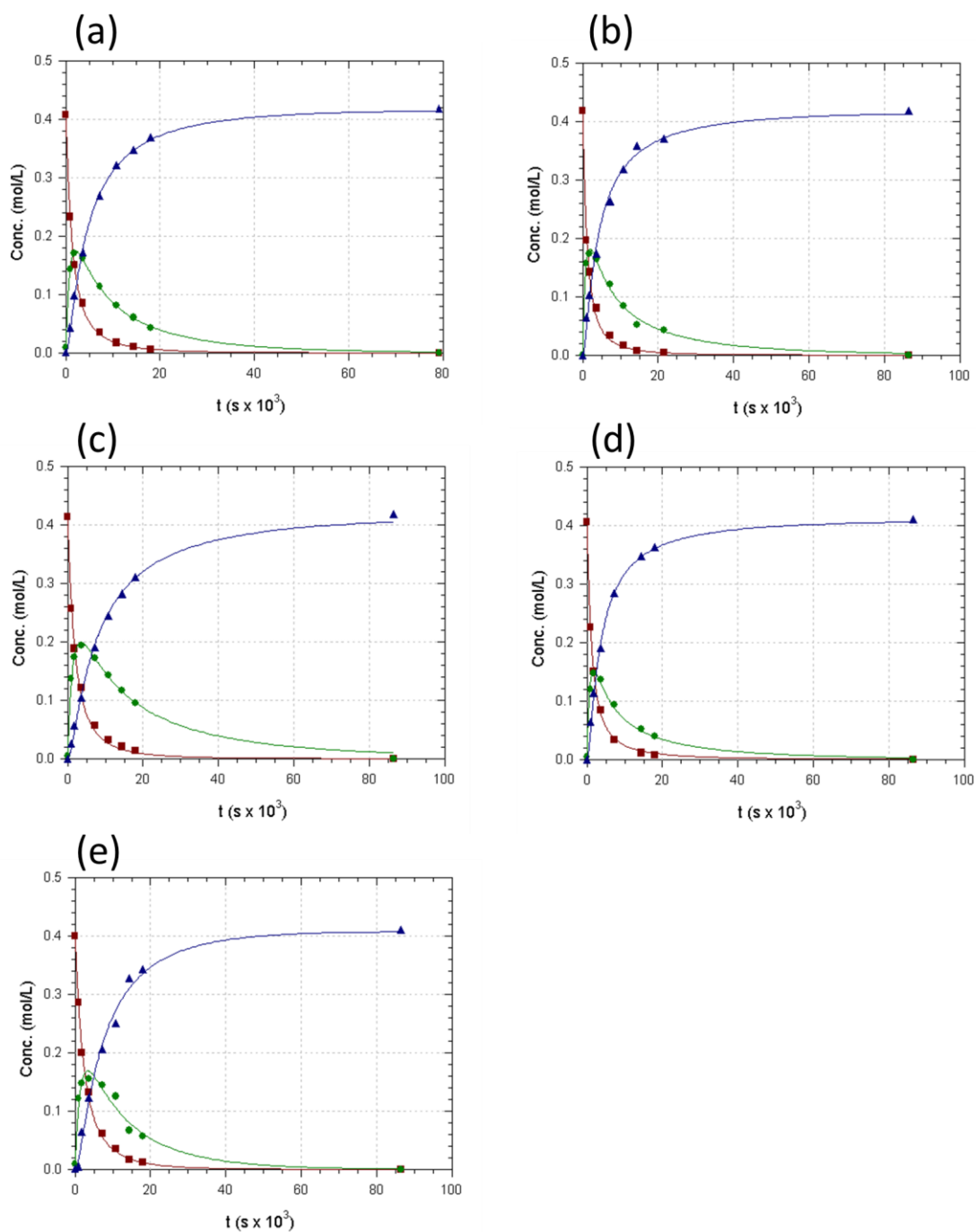


Figure 4.14. Kinetic traces for the oxidation of methyl *p*-tolyl sulfide (red squares) to its sulfoxide (green circles) and sulfone (blue triangles) by hydrogen peroxide in the presence of (a) **S10**, (b) **L7**, (c) **S7**, (d) **L5**, (e) **S5** as heterogeneous catalyst at 50 °C. The **Zr₄** is present in 0.1 mol% respect to the methyl *p*-tolyl sulfide. Symbols: experimental points; lines: second order kinetic fitting.

As a general trend, the systems prepared with Lutensol AT50 (entries 7, 8, 10) are more efficient than the corresponding SDS-based systems (entries 2, 3, 5), with initial TOF >20, sulfide conversion >80% after 1h, >50% sulfone selectivity. The worse dispersibility of the SDS nanoparticles may affect the catalytic behavior (see previous subsection). In addition, the lower cross-linking degree within the Lutensol AT50 series is likely pivotal for an easier substrate access towards the catalytic sites. As a matter of fact, despite the stronger aggregation state of **Zr₄** the swelling capability of Lutensol AT50-based samples is higher than those of the corresponding SDS-based samples (Table 4.2).⁴⁷ On the other hand, an increasing **Zr₄** content also favors the reaction (entries 5 and 10). In particular, the superior activity of **L10** (Figure 4.13) is demonstrated by the quantitative conversion of the substrate to the corresponding sulfone within 4 h, with TON = 1990. Although other d⁰ transition metal catalysts (Mo, W, V, and Ti) show generally better sulfoxidation performances, with complete conversion of sulfides into sulfones in less than 1 h and with TONs > 10⁵,^{128, 135-139}, the **Zr₄**-based hybrid catalytic system is much more efficient than mononuclear Zr compounds.¹⁴⁰ In addition, the nanodimensional morphology enables a TON increase of two orders of magnitude with respect to the corresponding bulk polymer.⁹³ The results are comparable with those obtained with soluble Zr-oxoclusters,⁵² with the advantages of increasing catalyst stability and offering the relevant opportunity of catalyst recovery by membrane filtration or centrifugation. The quasi-homogenous behavior of all systems is highlighted by the possibility to fit the kinetic traces by means of second order kinetic constants (k_1 and k_2) for both oxidation steps (Table 4.5 and Figure 4.14). Considering the selectivity of the reaction, the relatively high reactivity towards the less reactive sulfoxide is thus highlighted by the ratio k_1/k_2 , with values ranging between 1 and 1.8, being the lower value (corresponding to a faster sulfoxide oxidation) observed for the highest **Zr₄** content. The high efficiency of **L10** is underlined by the highest kinetic constants for both steps, resulting in a selectivity ratio of $k_1/k_2=1$.

The samples **S10** and **L10** were checked after the catalysis by means of FTIR, SEM imaging, and ICP-OES. As confirmed by the identical spectral features (signal position and relative intensities) before and after catalysis, the results provided by FTIR spectroscopy are in agreement with the intactness of the polymeric network (Figure 4.15).

SEM analysis was performed on the solid collected after catalysis and recovery through high speed centrifugation (Figure 4.16). While the higher cross-linking efficiency of **S10** guaranteed to preserve the entire nanoparticles matrix, in the case of **L10** the lower cross-linking results in the appearance of a porous morphology (see SEM image in Figure 4.16b), because of the solubilization of non-cross-linked parts of the matrix during the initial washing step.

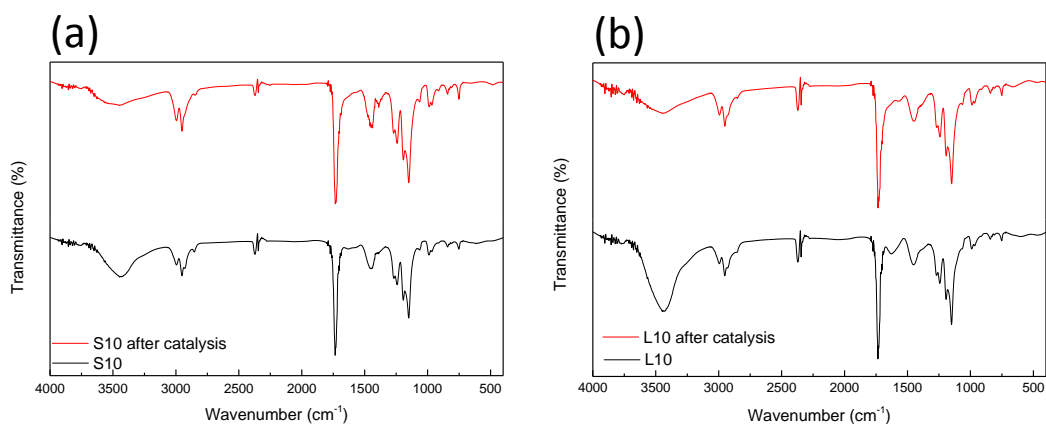


Figure 4.15. FTIR spectra of (a) **S10** before and after catalysis and (b) **L10** before and after catalysis.

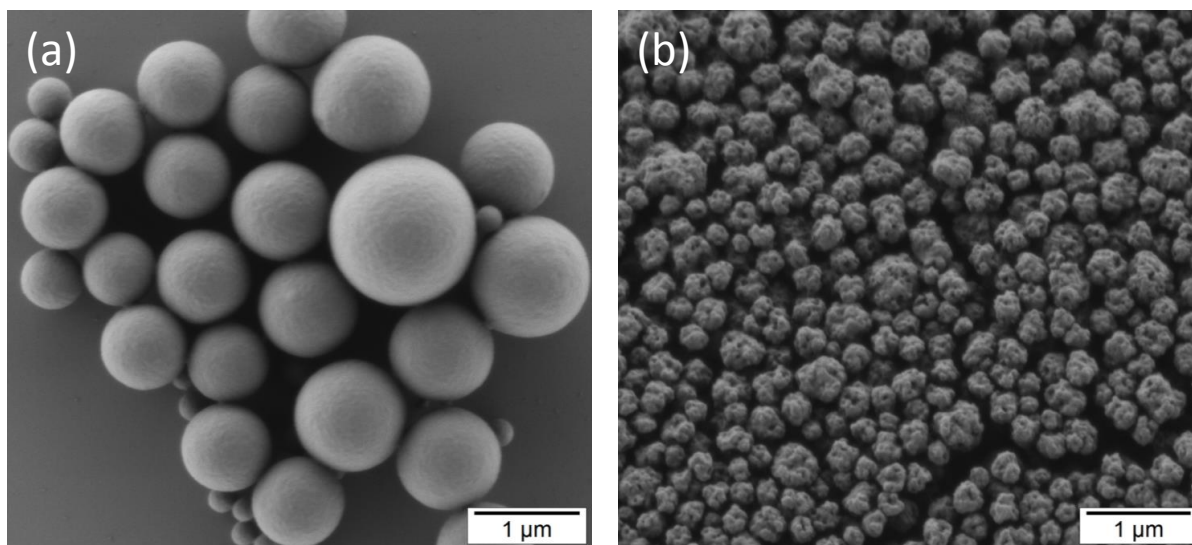


Figure 4.16. SEM images of the sample (a) **S10** and (b) **L10** after catalysis. The picture on the right clearly show the consequence of the lower cross-linking efficacy of **L10**.

Nevertheless, the efficient immobilization of the catalyst within the bulk matrix is confirmed by ICP-OES measurements for both samples after catalysis: After the initial washing step, the catalysis and recover of the catalyst by centrifugation the non-cross-linked part of the nanoparticles matrix is not present anymore due to the solubility of the linear polymer. Therefore, the ICP measurements done are referred to the **Zr₄** content in

only the cross-linked part. The Zr_4 contents after the catalysis are in agreement to calculated ones. The Zr content in the hybrid solids was constant before and after the reaction (Table 4.6), while no Zr was detected in solution.

A further proof of the intactness of the structure of the hybrid nanoparticles was obtained by monitoring the reaction after removal by centrifugation of the nanoparticles (**L10** and **L7**) after 30 min. The lack of residual reactivity of the resulting homogeneous phase (Figure 4.17) rules out the release of Zr-based active species in solution.

Table 4.6. Theoretical and determined Zr_4 content of the particles after catalysis.

Samples	Calculated Zr_4 content in the cross-linked part (wt%)	Zr_4 content by ICP after the catalysis (wt%) ^a
S10	10.9 ± 0.1	10.5 ± 0.5
L10	13.1 ± 0.1	14.7 ± 0.5

^[a] Determined by ICP-OES.

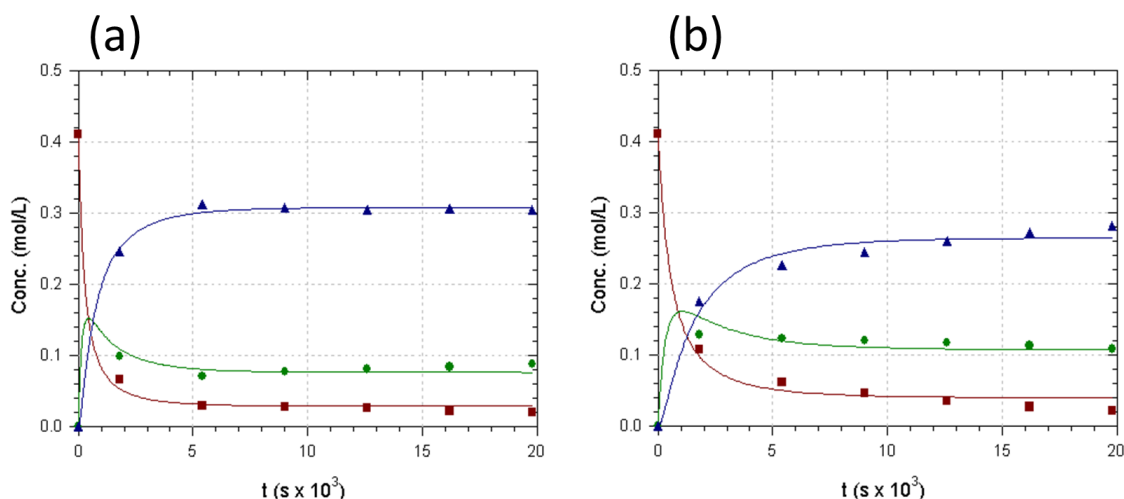


Figure 4.17. Kinetic traces for the oxidation of methyl *p*-tolyl sulfide (red squares) to its sulfoxide (green circles) and sulfone (blue triangles) by hydrogen peroxide in the presence of (a) **L10** and (b) **L7** as heterogeneous catalyst at 50 °C. The Zr_4 is present in 0.1 mol% respect to the methyl *p*-tolyl sulfide. The catalysts were removed after 30 min by high speed centrifugation.

For the representative catalysts **S7**, **L7**, **S10**, and **L10**, recycling of the heterogeneous catalyst was performed after high speed centrifugation of the suspensions (both Lutensol and SDS particles can be successfully recovered), followed by removal of the solution and recharge with a fresh mixture of sulfide and H_2O_2 . Again, all recycled catalysts lead to complete sulfide oxidation (entries 4, 6, 9, 11 in Table 4.5, Figure 4.18 and Figure 4.19). Despite a general decrease of sulfone yield observed after 4 h, all tested catalysts allow to obtain the complete sulfoxide oxidation to sulfone after 24 h. In addition, in the

presence of **L10**, most of the initial activity is retained during a total of 4 reaction runs (Figure 4.19), thus reaching 8000 catalytic cycles, with only a minor reactivity decrease.

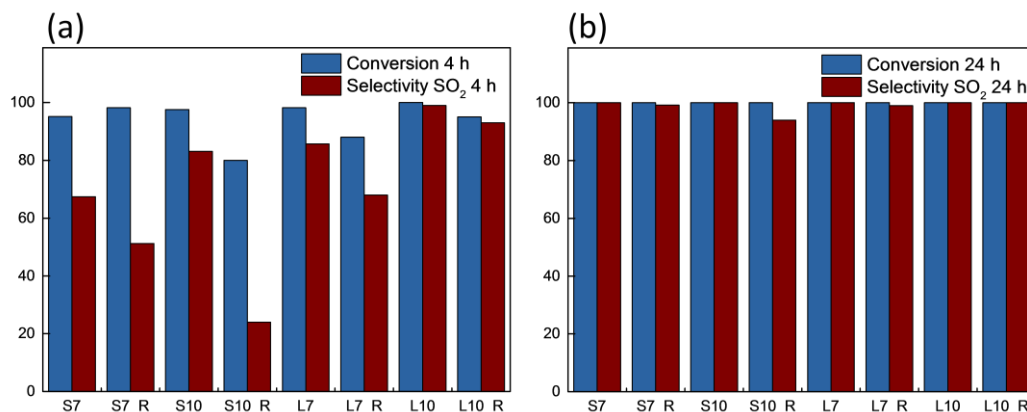


Figure 4.18. The methyl *p*-tolyl sulfide conversion and the selectivity to the sulfone at (a) 4 h and (b) 24 h in the presence of **S7**, **S10**, **L7** and **L10** in the first cycle and after recycling of the catalysts with a fresh mixture of sulfide and H₂O₂ (labeled as “_R”).

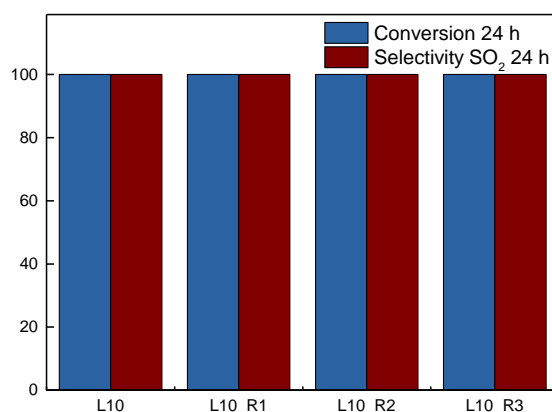


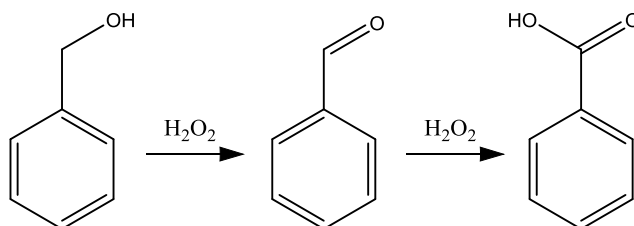
Figure 4.19. The methyl *p*-tolyl sulfide conversion and the selectivity towards the sulfone at 24 h in the presence of **L10** in the first cycle and after three recycles of the catalysts with a fresh mixture of sulfide and H₂O₂ (labeled as “_R1”, “_R2”, “_R3” for the first, second and third recycle, respectively).

4.1.6. Other Catalytic Trials

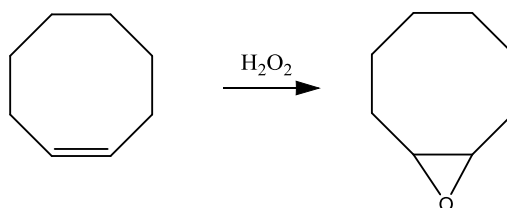
Since the hybrid poly(MMA-*co*-Zr₄) nanoparticles were proven to be endowed with high catalytic activity for the activation of hydrogen peroxide towards the oxidation of sulfur based compounds, other catalytic oxidation were also investigated: in particular, the oxidation of benzylic alcohol (Scheme 4.2) and the oxidation of the cyclooctene (Scheme 4.3). Oxidation of primary and secondary alcohols^{128, 141-143} and epoxidation of olefins¹⁴⁴ are among the most important reactions in organic chemistry. The obtained products

aldehydes, carbocyclic acids¹⁴⁵ and epoxides are important intermediates in the synthesis of many fine chemicals and pharmaceuticals.

Hybrid poly(MMA-*co*-**Zr₄**) nanoparticles were used as heterogeneous catalyst for the oxidation of benzylic acid and for the epoxidation of cyclooctene in presence of hydrogen peroxide. In both cases, **Zr₄** based hybrid nanoparticles displayed no catalytic activity for the activation of hydrogen peroxide towards these oxidation reactions (conversion 0%).



Scheme 4.2. Oxidation of benzylic alcohol to the corresponding benzaldehyde and benzoic acid by using hydrogen peroxide as oxidant and Ti based catalyst.



Scheme 4.3. Oxidation of cyclooctene to the corresponding cyclooctene oxide by using hydrogen peroxide as oxidant and Ti based catalyst.

4.1.7. **Zr₄-Surfactants Interaction**

The use of two different surfactants was explored, showing significant effects on morphology, cross-linking efficiency and catalytic performances. The ionic surfactant SDS provided better results in terms of cross-linking and oxocluster incorporation than the non-ionic Lutensol AT50. However, the use of a non-ionic surfactant provided a better dispersibility in the catalysis media and, consequently, a higher catalytic activity. The surfactant plays a key role and the different results obtained could be lead to the different nature of the surfactants (anionic and non-ionic for SDS and Lutensol AT50, respectively), with the different stabilization mechanisms and, consequently, with the different interactions with the system.

To evaluate the interactions between **Zr₄** and the surfactants, ¹H NMR spectra of the pristine cluster, SDS, Lutensol AT50 and mixture between **Zr₄** and surfactant were recorded either in THF or toluene. Shifts in the proton signals belonging to the vinyl

group of the methacrylate ligand are observed when the spectra is recorded in presence of Lutensol AT50 with respect to the pristine cluster (Figure 4.20 and Figure 4.21 for the spectra recorded in toluene and THF, respectively). While in the case of SDS no chemical shift are observed (Figure 4.22 and Figure 4.23 for the spectra recorded in toluene and THF, respectively). The chemical shifts observed, in presence of Lutensol AT50, is due to the possible coordination of Zr_4 by the polyether backbone of Lutensol AT50 which may explain the lower reactivity of the vinyl group during the polymerization and consequently the aggregates distribution of Zr_4 in the particles matrix (Figure 4.7b-c), the lower incorporation and finally the lower cross-linking efficiency observed in these samples.

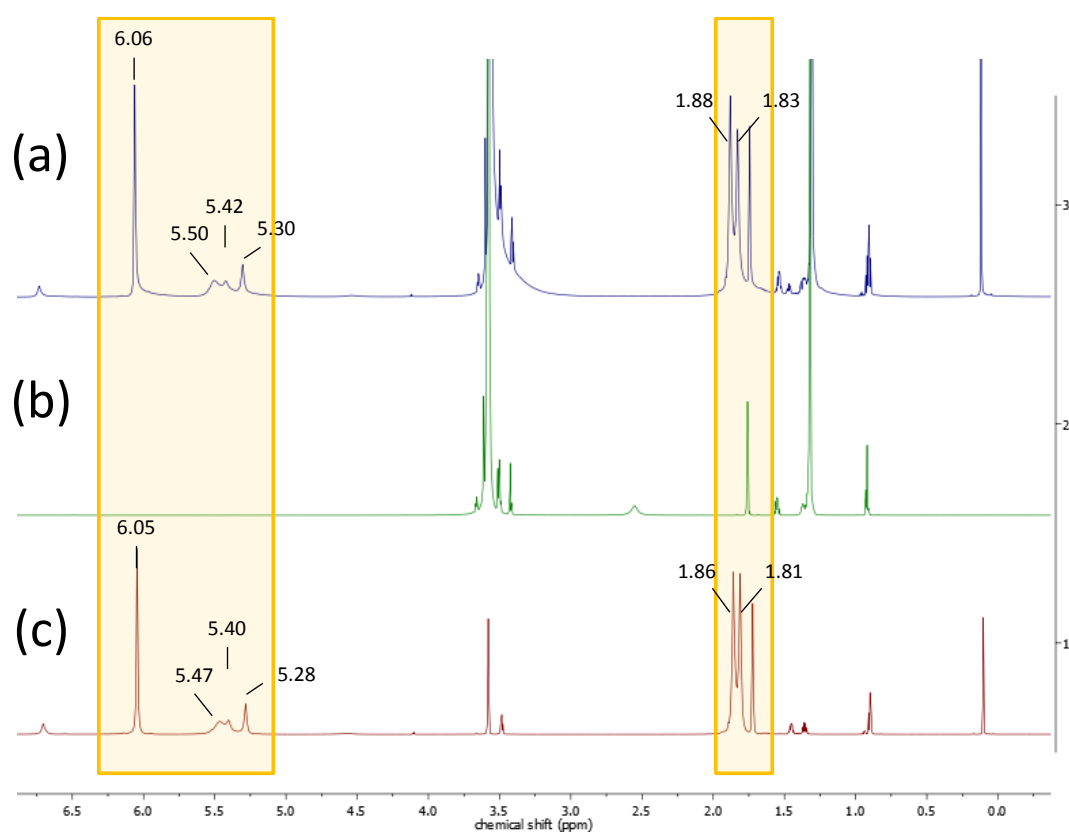


Figure 4.20. ^1H NMR spectra of (a) a mixture of Zr_4 and Lutensol AT50, (b) Lutensol AT50, and (c) Zr_4 , all in THF.

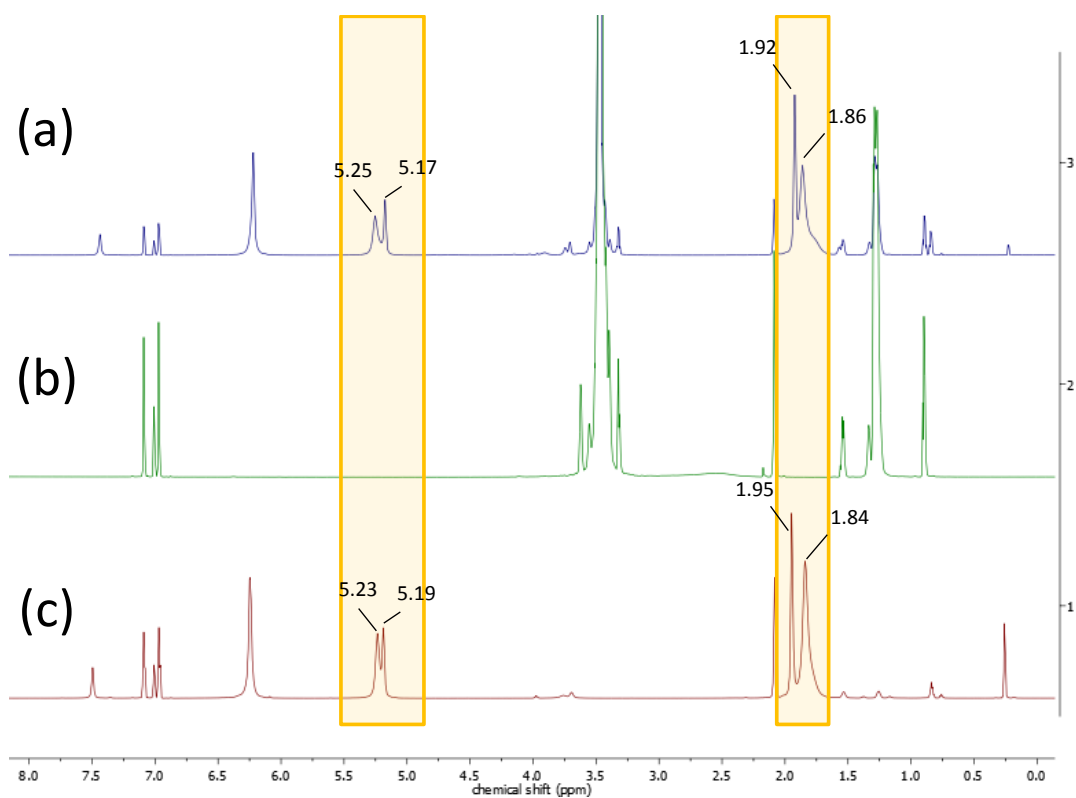


Figure 4.21. ^1H NMR spectra of (a) a mixture of Zr_4 and Lutensol AT50, (b) Lutensol AT50, and (c) Zr_4 , all in toluene.

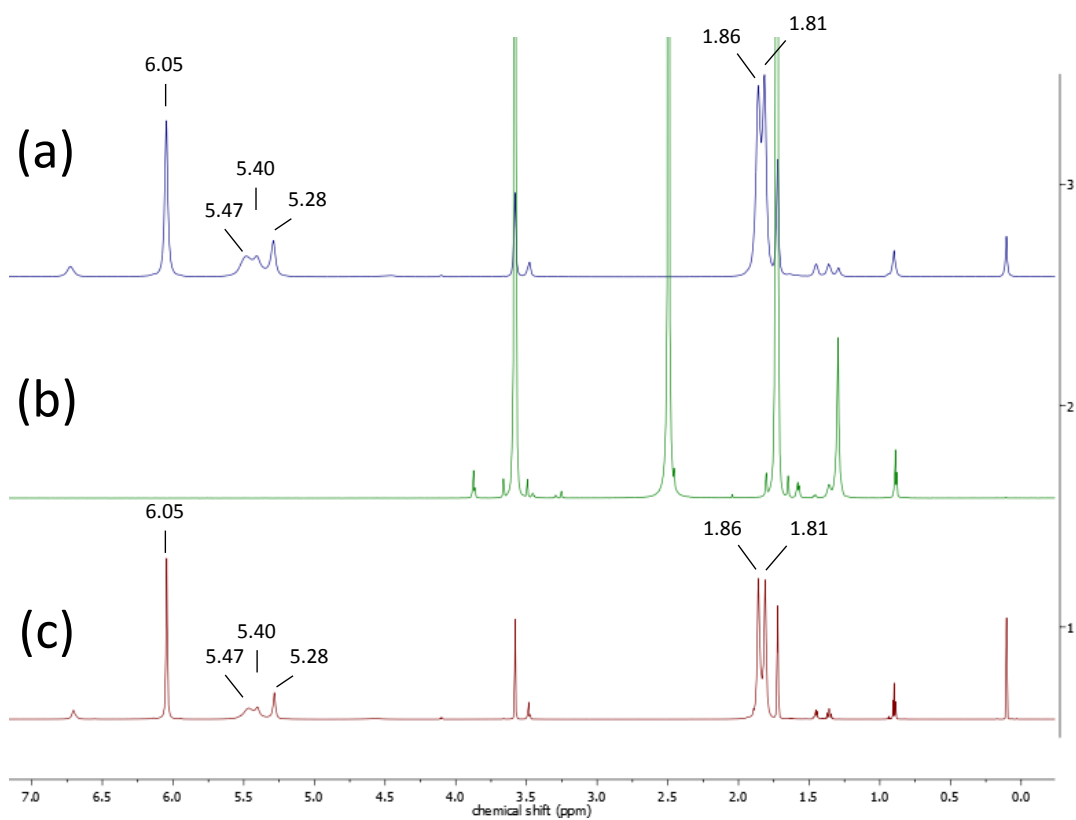


Figure 4.22. ^1H NMR spectra of (a) a mixture of Zr_4 and SDS, (b) SDS, and (c) Zr_4 , all in THF.

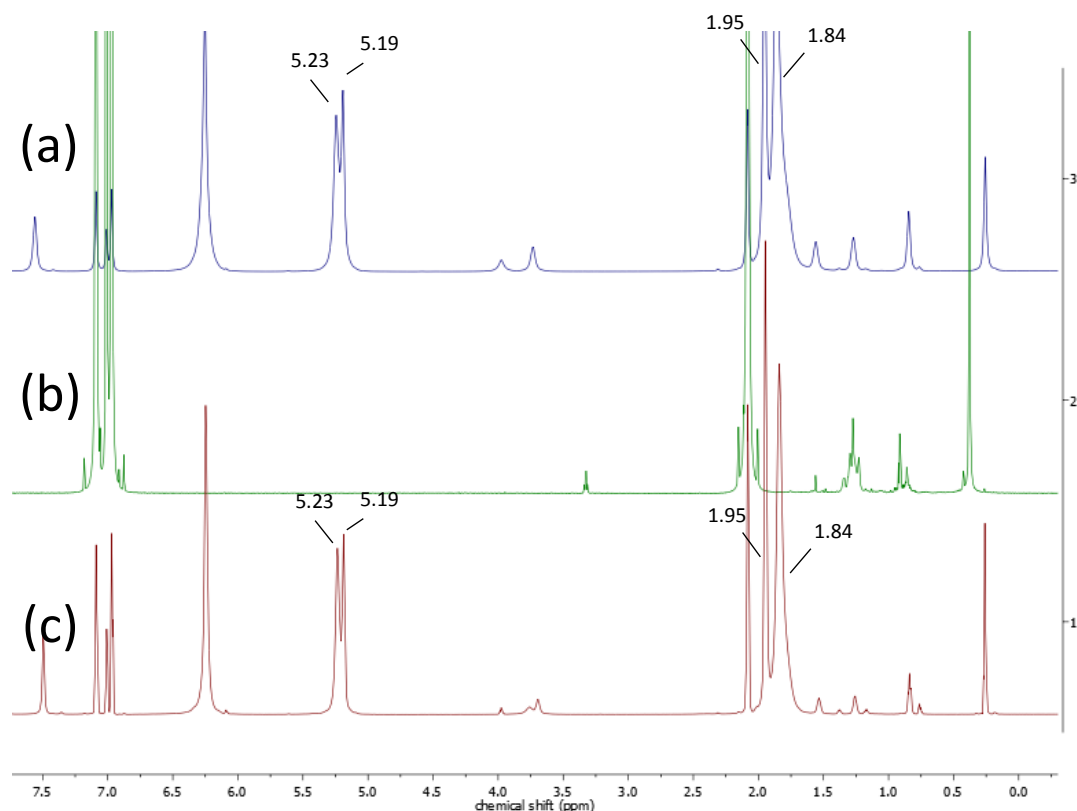


Figure 4.23. ^1H NMR spectra of (a) a mixture of Zr_4 and SDS, (b) SDS, and (c) Zr_4 , all in toluene.

In case of SDS, full incorporation (Figure 4.4) combined with a molecular distribution of Zr_4 led to a higher cross-linking efficiency (Figure 4.9). The results obtained with SDS are due to the lack of interactions by this surfactant with the double bonds of the oxocluster, indeed confirmed by no shifts observable in the ^1H NMR spectra. Although SDS is not affecting the polymerization ligands and the Zr_4 is molecularly distributed, the STEM cross-sections in Figure 4.7a-c show a gradient in Zr_4 concentration: higher at the particles edge and lower going to the inner part. The higher concentration of Zr_4 at the particles surface suggests an affinity between the oxocluster and the anionic surfactant, confirmed by the higher incorporation of SDS in presence of Zr_4 in the nanoparticles matrix. The experiment was done evaluating the amount of SDS in solution (not adsorbed on the nanoparticles) using Stains-All dye, as suggested by F. Rusconi *et al.*¹⁴⁶ All particles used in the work were washed as reported in the experimental Section 6.1.3; comparisons with unwashed samples for samples **S0**, **S5** and **S10** are shown in Table 4.7. Taking into account the initial amount used in the miniemulsion process, the unwashed samples should contain an amount of surfactant of about 1.10 wt%, but lower values were obtained for the samples, which indicates that part of the surfactant is entrapped in the nanoparticles and cannot be detected. An interesting outcome is the

increase of the non-detectable surfactant content with the amount of \mathbf{Zr}_4 in the nanoparticles matrix. This effect could be ascribed to the affinity between the surfactant and the oxocluster, and it could explain the higher concentration of SDS at the particle surface observed for sample **S10** in Figure 4.4. Regarding the detected SDS content (or SDS in solution), we could also observe a decrease in the amount of “removed SDS” at higher amount of \mathbf{Zr}_4 , therefore confirming a probable further interaction between the SDS and \mathbf{Zr}_4 .

Table 4.7. Evaluation of SDS amount by using Stains-All dye.

Samples	Theoretical SDS content (%) ^b	Detected SDS content (%) ^c	Non-detectable SDS content (%) ^d	Removed SDS (%) ^e
S10 ^a	1.10	0.02	1.08	—
S10	nd	0.02	—	34
S5 ^a	1.10	0.13	0.97	—
S5	nd	0.02	—	82
S0 ^a	1.10	0.36	0.75	—
S0	nd	0.02	—	95

^[a] Before the surfactant removal. ^[b] Calculated taking into account the starting amounts in the miniemulsion process. ^[c] By absorbance measurements recorded at 438 nm on a Tecan Infinite M1000 plate reader. The SDS trapped in the nanoparticles cannot be detected with this method. ^[d] Difference between the theoretical and the detected SDS contents. ^[e] Ratio in % between the sample after and before surfactant removal.

4.1.8. Conclusions

The synthesis of hybrid poly(MMA-*co*- \mathbf{Zr}_4) nanoparticles by miniemulsion and their successful application in heterogeneous catalysis have been investigated. The two-fold role of the inorganic comonomer \mathbf{Zr}_4 , acting both as catalytically active species and as cross-linking units of the nanoparticles network, endows the hybrid nanoparticles with a high potential for heterogeneous catalysis. Indeed, the thermal properties and the swelling behavior in organic solvent of the cross-linked polymer matrix were shown to be enhanced by the presence of the oxocluster. The use of two different surfactants was explored, showing significant effects on morphology, cross-linking efficiency and catalytic performances. In all cases, the miniemulsion technique provides nanoparticles with high active surfaces, whose catalytic behavior approaches the homogeneous one. The hybrid poly(MMA-*co*- \mathbf{Zr}_4) nanoparticles were tested for the oxygen transfer to methyl *p*-tolylsulfide, highlighting the advantages of the polymeric matrix on reaction

selectivity, leading to the preferential formation of methyl *p*-tolysulfone. Remarkably, the catalytic activity after several cycles could be preserved, with only a minor reactivity decrease, which demonstrates an effective recyclability of the catalysts.

4.2. Titanium Oxocluster-based Thermoresponsive Hybrid Nanoparticles for Catalysis Applications

In Section 4.1.6, hybrid poly(MMA-*co*-Zr₄) nanoparticles displayed absent catalytic activity for the activation of hydrogen peroxide towards the oxidation of benzylic acid and the epoxidation of cyclooctene. For this reason, in this section, a Ti-based oxocluster is investigated as alternative catalyst. In particular, the pristine Ti₉O₈(OPr)₄(OMc)₁₆ oxocluster and Ti₉O₈(OPr)₄(OMc)₁₆/polymer hybrid nanoparticles are used as homogeneous and heterogeneous catalysts, respectively, for the oxidation reactions of benzylic acid and for the epoxidation of cyclooctene. The synthesis of the polymer/inorganic hybrid nanoparticles occurs in the confined space of inverse miniemulsion droplets. Free radical polymerization is used to prepare thermoresponsive nanoparticles based on the amphiphilic comonomers *N*-isopropylacrylamide (NIPAM), *N*-acryloyl glycinamide (NAGA) or *N*-methacryloyl glycinamide (NMGA). Although Ti₉O₈(OPr)₄(OMc)₁₆ is characterized by the presence of 16 double bonds, it has been found that its methacrylate moieties are not participating in the reactions, thus allowing only a physical incorporation of the oxocluster. Therefore, the absence of stability against the acid environment of H₂O₂ in homogenous catalysis conditions leads to low catalytic activity also in heterogeneous conditions.

4.2.1. Introduction

PNIPAM is well-known to have both hydrophilic and hydrophobic character depending on the temperature, thus showing interesting stimuli-responsive properties in aqueous solution.¹⁴⁷⁻¹⁵² Above the so-called *lower critical solution temperature* (LCST) (~32 °C), PNIPAM particles undergo a volume phase transition (VPT), in which the water is expelled from the polymer network and the swollen state at low temperature evolves into a shrunken state at high temperature.¹⁴⁹⁻¹⁵¹

The volume phase transition of PNIPAM used as supporting matrix for heterogeneous catalyst could give the possibility to modulate (*i.e.*, switching “on” and “off”) the catalytic activity, simply by adjusting the temperature.¹⁵³ A remarkable example was

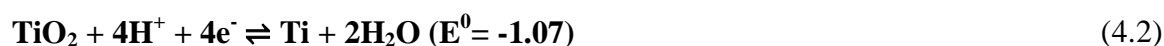
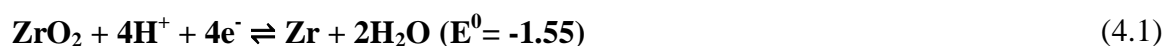
reported by Jiang *et al.* for the model reduction reaction of 4-nitrophenol with NaBH₄ to 4-aminophenol.¹⁵³⁻¹⁵⁵ A thermoresponsive hybrid nanocomposite was used as a catalyst. In particular, the nanocomposite was comprised of a gold nanoparticle (15 nm diameter) core surrounded by a thermoresponsive hydrogel of cross-linked poly(glycidyl methacrylate-*co*-*N*-isopropylacrylamide) (PGMA-*co*-PNIPAM). The nanoparticles were swollen (280 nm diameter) below the LCST, and they were able to shrink to 113 nm at 75 °C. Because of the homogenous-like catalysis condition, at $T < \text{LCST}$ the catalyst was active. At temperature higher than the LCST the reduction rate was instead significantly decreased because of the slow diffusion of the reactants through the shrunken hydrophobic thermoresponsive polymer shell.¹⁵⁵

Heterogeneous catalysts based on an LCST-polymer supporting matrix could prevent the reaction from accelerating out of control: once the temperature is higher than the LCST, the shrunken polymer matrix would make the catalytic sites not accessible anymore.^{153, 156-157} Exothermic industrial processes are difficult to handle once they reach the so-called thermal runaway, because the heat produced is accelerating the overall process rate, thus developing in turn higher heat flows, finally leading to a thermal explosion.¹⁵⁸⁻¹⁶¹ Therefore, by using LCST-polymer-based heterogeneous catalysts, exothermic reaction rates would be conveniently controlled, especially for scaled-up catalytic reactions.

Polymers displaying *upper critical solution temperature* (UCST) in a suitable range of temperature could be also used as heterogeneous catalyst matrix. In contrast to the LCST-polymers, their thermoresponsive behavior would be useful for the recovery of the catalyst, just by decreasing and making the polymer not soluble anymore: in this way, the catalyst could be separated and recovered.¹⁶²⁻¹⁶³ In this regard, poly(*N*-acryloyl glycinamide) (in the following labeled as PNAGA) showed a sharp UCST in pure water.¹⁶⁴⁻¹⁶⁵ Thermally reversible hydrogen bonding within the polymer chain are responsible of the volume phase transition: a hydrogen bond between carbonyl group (hydrogen bond acceptor) and the amide (hydrogen bond donor) can be formed at temperature below the UCST.¹⁶⁶ Therefore, shrunken and swollen states are possible to be observed at temperatures below and above the UCST, respectively. PNAGA was first synthesized in 1964 by Haas and Schuler.¹⁶⁷⁻¹⁶⁸ The first hint that the homopolymer of PNAGA might show a UCST behavior was given by Ohnishi *et al.*¹⁶⁹⁻¹⁷⁰ However, the UCST-type phase transition of the PNAGA homopolymer has only been reported by Agarwal *et al.* in 2010. They described the cloud points from 0.03 to 5.4 wt%, the gel

melting points up to 14 wt% of PNAGA in water, and the fact that traces of ionic groups in the polymer dramatically suppress the UCST.¹⁶⁴⁻¹⁶⁵

In this section, a Ti-based oxocluster was investigated as alternative catalyst for oxidation reactions in presence of hydrogen peroxide. Titanium, being a transition metal of the fourth group, displays higher tendency to change its coordination upon reaction, and moreover it is able to form peroxide species with H₂O₂ without being extracted from its framework. In contrast to Zr^{IV}, Ti^{IV} has a higher reduction potential because of the lower dimensions, thus allowing it to be easier reduced and, as a consequences, a better catalyst in oxidation reactions:



The higher reduction potential is what makes Ti-containing molecular sieves among the best catalysts for selective oxidation with H₂O₂.¹⁷¹⁻¹⁷²

Herein we report the use of Ti₉O₈(OPr)₄(OMc)₁₆ (in the following labeled as **Ti₉**) oxocluster, first as a homogenous and then as a heterogeneous catalyst for the oxidation of benzylic acid and for the epoxidation of cyclooctene in the presence of hydrogen peroxide. NIPAM as LCST comonomer, and NAGA and NMGA (the latter with methacrylate instead of acrylate) as UCST comonomers were used as a supporting thermoresponsive matrix for the resulting hybrid catalyst. Free radical polymerization within inverse miniemulsion droplets ensures a physical incorporation of the oxocluster **Ti₉** in the thermosensitive polymer matrix. In contrast to **Zr₄**,⁵¹ the titanium oxocluster is not participating in the polymerization (although the presence of polymerizable methacrylate moieties), thus showing a high catalytic activity before the degradation of its cluster core.

4.2.2. Homogeneous Catalysis with Ti₉O₈(OPr)₄(OMc)₁₆

The catalytic activity of **Ti₉** for the oxidation of benzylic acid (Scheme 4.2) and for the epoxidation of cyclooctene (Scheme 4.3) in the presence of hydrogen peroxide was initially investigated in homogenous conditions, displaying an initial reactivity followed by a plateau (Figure 4.24). However, complete oxidation to benzoic acid and to cyclooctene oxide could not be observed. The reaction was conducted either with half equivalent or with two equivalents of hydrogen peroxide with respect to the reagents, in

order to evaluate a possible degradation of the Ti_9 . Although for the oxidation of benzyl alcohol no relevant changes were displayed, the kinetic traces for the oxidation of cyclooctene, catalyzed by half equivalent of hydrogen peroxide, showed a higher conversion over the time for the first 100 min, followed then by a plateau region (Figure 4.25).

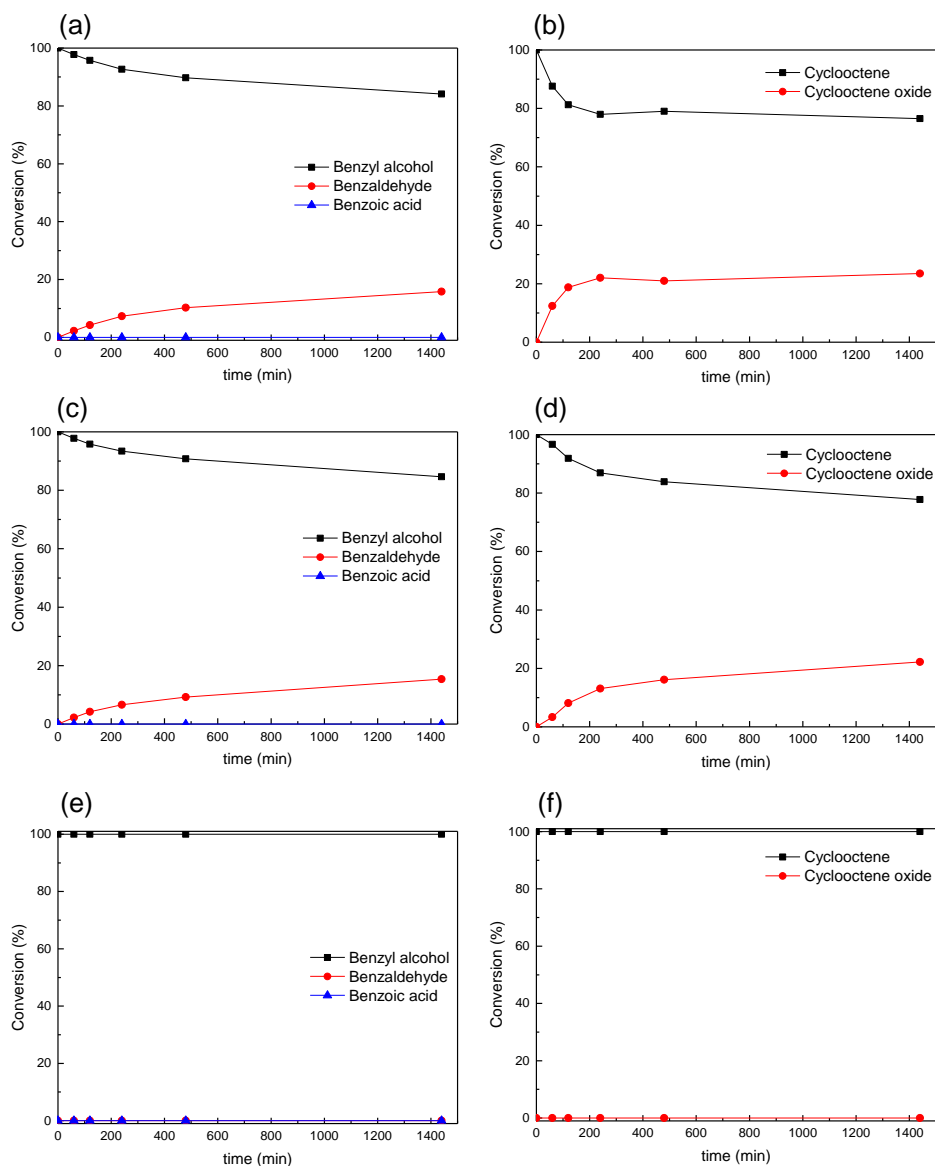


Figure 4.24. Kinetic traces for (a), (c), and (e) the oxidation of benzylic alcohol (black squares) to its benzaldehyde (red circles) and for (b), (d), and (f) the epoxidation of cyclooctene (black squares) to its oxide (red circles) by hydrogen peroxide in the presence of $\text{Ti}_9\text{O}_8(\text{OPr})_4(\text{OMc})_{16}$ oxocluster as homogeneous catalyst at 50°C . The Ti_9 is present in 0.1 mol% with respect to the reagents, the reaction was conducted using either (a) and (b) half equivalent or (c) and (d) two equivalents of H_2O_2 with respect to the reagents. Charts (e) and (f) represent the blank in presence of two equivalents equivalent H_2O_2 and without Ti_9 .

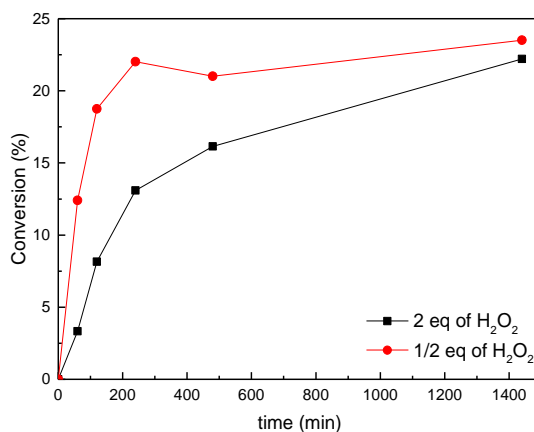


Figure 4.25. Kinetic traces for the epoxidation of cyclooctene by hydrogen peroxide in the presence of $\text{Ti}_9\text{O}_8(\text{OPr})_4(\text{OMc})_{16}$ oxocluster as homogeneous catalyst at 50 °C. The Ti_9 is present in 0.1 mol% respect to the reagents, the reaction was conducted either using half equivalent (red circles) or two equivalents of H_2O_2 (black squares) respect to the reagents.

The higher reactivity at the initial stages of the reaction in the presence of a lower amount of oxidizer could be attributed to the degradation of the Ti_9 in the presence of peroxide. In contrast, the plateau region is due to the full consumption of hydrogen peroxide. In both cases, the maximum conversion is around 20%. Additionally, when the reaction was conducted with double amount of oxidizer, a drastic darkening of the reaction solution was observed. Ti_9 appears as orange-yellow crystals: these crystals give initially a yellowish color to the solution that evolves to brownish in presence of H_2O_2 . The degradation of the cluster by hydrogen peroxide is also confirmed by FTIR (Figure 4.26). In particular, the strong and broad absorption bands centered at 3300 cm^{-1} and at 1600 cm^{-1} suggest the presence of water molecules in the precipitate. Moreover, the lowering in intensity of other signals belonging to the methacrylate ligands (below 1400 cm^{-1}) is due to the hydrolysis mechanism of the oxocluster in presence of H_2O_2 .

4.2.3. Heterogeneous Catalysis with Hybrid Poly(NAGA-co-Zr₄), Poly(NMGA-co-Zr₄) and Poly(NIPAM-co-Zr₄) Nanoparticles

Based on the encouraging results described in the previous Section 4.2.2, and in order to prevent the degradation of Ti_9 core, hybrid nanoparticles based on amphiphilic polymer were synthesized. *N*-isopropylacrylamide (NIPAM), *N*-acryloyl glycineamide (NAGA)

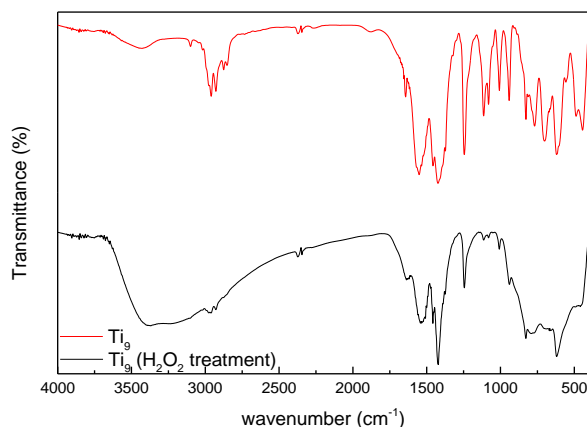


Figure 4.26. FTIR spectra of $\text{Ti}_9\text{O}_8(\text{OPr})_4(\text{OMc})_{16}$ before and after treatment with hydrogen peroxide.

and *N*-methacryloyl glycinamide (NMGA) were combined with 10 wt% of **Ti₉** as inorganic comonomers, thus yielding hybrid poly(NIPAM-*co*-**Ti₉**) (**Ti₉/PNIPAM**), poly(NAGA-*co*-**Ti₉**) (**Ti₉/PNAGA**), and poly(NMGA-*co*-**Ti₉**) (**Ti₉/PNMGA**) nanoparticles. The comonomers were chosen due to the thermoresponsive behavior of the resulting polymer. Inverse miniemulsion polymerization was adopted in the presence of the amphiphilic block copolymer poly(ethylene/butylene)-*block*-poly(ethylene oxide) (P(E/B)-*b*-PEO) as nonionic surfactant.

As reported for poly(MMA-*co*-**Zr₄**) nanoparticles, the cross-linking efficiency and the amount of cluster incorporated was evaluated by ICP-OES and GPC measurements, respectively. The incorporation of the oxocluster was higher in case of **Ti₉/PNIPAM** (8.5 wt%), while for the both UCST matrix was not possible to incorporate more than 6.5 wt%.

Despite having methacrylate ligands available for polymerization, **Ti₉** is not acting as cross-linker for the polymer matrix with none of the comonomer used (Table 4.8). Therefore, based on the results evidencing lacks of cross-linking, it could be concluded that **Ti₉** is only physically embedded into the polymer nanoparticles matrix and not covalently attached.

The thermoresponsive behavior of **Ti₉/PNIPAM**, **Ti₉/PNAGA**, and **Ti₉/PNMGA** was also investigated by evaluation of the hydrodynamic diameter with DLS (Table 4.9). The expected behavior for PNIPAM was observed, with an initial decrease in size followed by particles aggregation by increasing the temperature from 20 to 60 °C.

Table 4.8. Main features of poly(NAGA-*co*-Ti₉), poly(NMGA-*co*-Ti₉) and poly(NIPAM-*co*-Ti₉) nanoparticles.

Samples ^a	Ti ₉ content as comonomer (wt%)	Actual Ti ₉ content (wt%) ^b	Cross-linked fraction (wt%) ^c
Ti ₉ /PNIPAM	10	8.5 ± 0.5	0
Ti ₉ /PNAGA	10	5.7 ± 0.5	0
Ti ₉ /PNMGA	10	6.5 ± 0.4	0

^[a] The letters in the sample codes refer either to poly(NAGA-*co*-Ti₉), poly(NMGA-*co*-Ti₉) and poly(NIPAM-*co*-Ti₉) nanoparticles. ^[b] Determined by ICP-OES; ^[c] Determined by GPC on supernatants.

Unexpectedly, also in the case of UCST polymers, a decrease in size was observed. As reported by Agarwal *et al.*,¹⁶⁴ any ionic species present in the system could interact with the amide group (H-bonding donor), thus suppressing the volume phase transition. The cluster synthesis is happening in acidic environment because of the presence of methacrylic acid. Consequently, acid moieties could still be present in the interstitial positions of the crystal lattice when Ti₉ is used as a comonomer and is dissolved in the miniemulsion dispersed phase. Temperature-dependent measurements were also performed for the neat polymer nanoparticles (without the presence of cluster embedded) poly(*N*-isopropylacrylamide) and poly(*N*-acryloyl glycinamide) (PNAGA and PNMGA, respectively). Unfortunately, also in this case, no specific trend was detected.

Having proven the presence of the catalytically active species Ti₉ in the polymer matrix (only by physical incorporation), the hybrid poly(NMGA-*co*-Ti₉) and poly(NIPAM-*co*-Ti₉) nanoparticles were investigated for the epoxidation of cyclooctene and the oxidation of benzyl alcohol (Figure 4.27). Regarding the epoxidation of cyclooctene, by using poly(NMGA-*co*-Ti₉) nanoparticles the reaction did not take place, whereas by using poly(NIPAM-*co*-Ti₉) nanoparticles no considerable improvement was observed in the conversion degree with respect to the homogeneous condition. In contrast, for the oxidation of benzyl alcohol in acetonitrile, poly(NIPAM-*co*-Ti₉) nanoparticles showed an increase of conversion over time with respect to the homogeneous condition by a factor of two. However, the maximum conversion achievable was only 34%. Although the oxocluster is not acting as a cross-linker, the embedding in the PNIPAM matrix is actually retarding the degradation of Ti₉. As in homogeneous catalysis, the darkening of the reaction solution, evolving to brownish in the presence of H₂O₂, was also observed in this case. Differently, using poly(NMGA-*co*-Ti₉) nanoparticles, no relevant catalytic improvement was observed with respect to the

homogeneous case. The oxidation of benzyl alcohol using either Ti_9 /PNMGA or Ti_9 /PNIPAM was also performed in water, as reaction solvent. In case of Ti_9 /PNMGA the reaction did not take place, whereas using Ti_9 /PNIPAM, a noticeable decrease in conversion was observed, compared to the reaction conducted in acetonitrile.

Table 4.9. Thermoresponsive behavior of hybrid poly(NIPAM-*co*- Ti_9), poly(NAGA-*co*- Ti_9), poly(NMGA-*co*- Ti_9), poly(N-acryloyl glycinamide) and poly(N-methacryloyl glycinamide) nanoparticles.

Temperature (°C)	Ti_9 /PNIPAM hydrodynamic diameter in water at R.T. (nm) ^a	Ti_9 /PNAGA hydrodynamic diameter in water at R.T. (nm) ^a	Ti_9 /PNMGA hydrodynamic diameter in water at R.T. (nm) ^a	PNAGA hydrodynamic diameter in water at R.T. (nm) ^a	PNMGA hydrodynamic diameter in water at R.T. (nm) ^a
20	105 (±6%)	937 (±28%)	480 (±21%)	449 (±14%)	216 (±10%)
30	102 (±11%)	605 (±15%)	552 (±17%)	-	-
40	turbid	435 (±12%)	298 (±16%)	305 (±16%)	344 (±16%)
50	turbid	439 (±11%)	251 (±10%)	-	-
60	turbid	353 (±10%)	175 (±13%)	413 (±20%)	226 (±11%)

^[a] Determined by DLS: Samples were diluted and filtered through a 5µm SV Filter (Millipore) before the analysis.

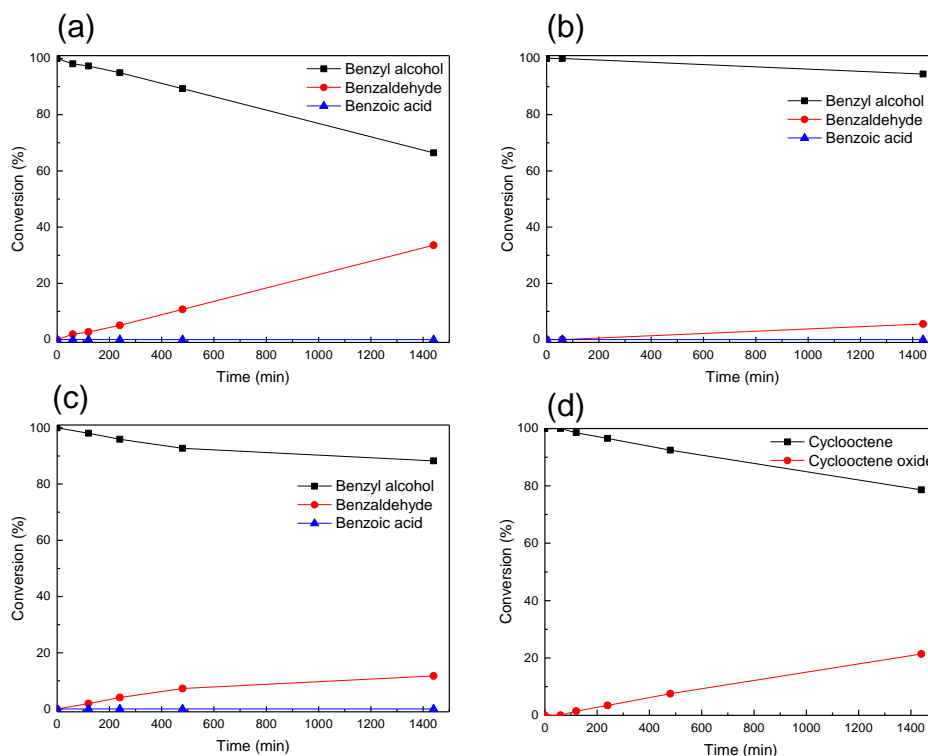


Figure 4.27. Kinetic traces for (a), (b), and (c) the oxidation of benzylic alcohol (black squares) to benzaldehyde (red circles) and for (d) the epoxidation of cyclooctene (black squares) to its oxide (red circles) by hydrogen peroxide at 50 °C. The reactions are conducted in presence of (a), (c), and (d) poly(NIPAM-*co*- Ti_9) nanoparticles and (b) poly(NMGA-*co*- Ti_9) nanoparticles. Ti_9 is present in 0.1 mol% and 2 equivalents of H_2O_2 with respect to the reagents are used. The reaction solvent is either (a), (b), and (d) acetonitrile or (c) water.

4.2.4. Conclusions

In this section, we reported the application of $\text{Ti}_9\text{O}_8(\text{OPr})_4(\text{OMc})_{16}$ as a homogeneous catalyst and as a heterogeneous catalyst. In heterogeneous conditions, $\text{Ti}_9\text{O}_8(\text{OPr})_4(\text{OMc})_{16}$ has been embedded in the amphiphilic polymers *N*-acryloyl glycinamide, *N*-methacryloyl glycinamide, and *N*-isopropylacrylamide. The oxidation of benzylic alcohol and the epoxidation of cyclooctene were investigated as model oxidation reactions. Both in homogeneous as well as in heterogeneous conditions, the degradation of the catalytic site by hydrogen peroxide prevented the formation of the product with a conversion higher than 34%. The physical incorporation of the $\text{Ti}_9\text{O}_8(\text{OPr})_4(\text{OMc})_{16}$ resulted in the degradation of the oxocluster core in presence of H_2O_2 during the catalytic reactions. Indeed, the lack of a covalent bonding with the polymer matrix prevents to $\text{Ti}_9\text{O}_8(\text{OPr})_4(\text{OMc})_{16}$ to be firmly attached, and therefore to act as a cross-linker of the resulting hybrid polymer matrix. Finally, the protecting action of the matrix, based on the “freezing” of the oxocluster structure, could not be pursued.

4.3. Zirconium Oxocluster/Polymer Hybrid Nanoparticles Prepared by Photoactivated Miniemulsion Copolymerization

Photoactivated free radical miniemulsion copolymerization of methyl methacrylate (MMA) and the zirconium oxocluster $\text{Zr}_4\text{O}_2(\text{methacrylate})_{12}$ is used as an effective and fast preparation method of polymer/inorganic hybrid nanoparticles (Figure 4.28). The oxoclusters, covalently anchored to the polymer network, are acting as metal-organic cross-linkers, thus improving the thermomechanical properties of the resulting hybrid nanoparticles. Three different benzoin carbonyl radical photoinitiators are investigated and a kinetic study on the copolymerization process is reported. The obtained materials are compared in terms of cross-linking, effectiveness of cluster incorporation, and size distribution with the analogous nanoparticles produced by using conventional thermally-induced free radical miniemulsion copolymerization in Section 4.1.

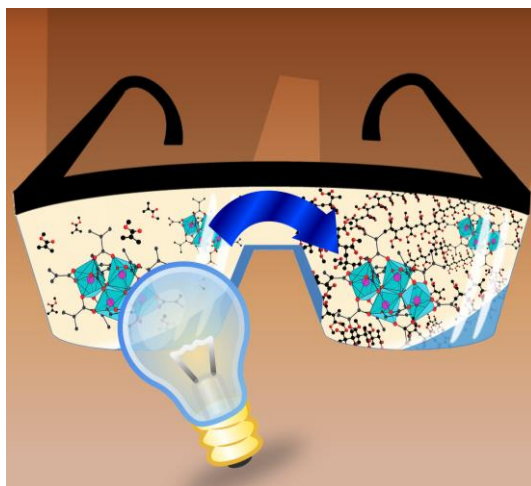


Figure 4.28. Schematic illustration of photoactivated copolymerization between methyl methacrylate (MMA) and $Zr_4O_2(\text{methacrylate})_{12}$. The copolymerization is occurring in miniemulsion droplets. The lenses of the UV protection glass correspond to the monomer droplets during irradiation (left) and to the polymer particle (right, after polymerization).

4.3.1. Introduction

In a time in which 3D printing is becoming a hot topic,¹⁷³⁻¹⁷⁵ photopolymerization processes are attracting an increasing attention. Photoinduced polymerization is a suitable and viable approach for the so-called additive manufacturing, the principle on which most of 3D printers are based. For this specific purpose, but also for many industrial processes (*e.g.*, UV-curing of polymer coatings),¹⁷⁶⁻¹⁷⁸ photoinduced polymerization is better suited than thermally activated polymerization, because it is characterized by higher reaction rates, milder and more environmental friendly conditions (*e.g.*, the reaction can be conducted at room temperature and in the absence of volatile organic solvents, and it requires typically less energy than the thermally activated ones). Photopolymerization, especially of methacrylates, is also essential for light-curing of dental materials.¹⁷⁹⁻¹⁸² In addition, when considering free radical polymerization, an important aspect to be taken into account is the chemical nature of the initiator. Thermal free radical initiators are mostly based on peroxides and azo-compounds, which are often unstable—even explosive—and reactive at room temperature, thus making their storage and shipping on a big scale highly demanding in terms of safety and energy, since they need to be stored at low temperatures. In contrast, photoinitiators are easier to handle, because only dark conditions are required to ensure stability.¹⁸³⁻¹⁸⁴

Photoinduced photopolymerization is endowed with favorable features for the replacement of many thermally based polymerization processes. However, when exploring its implementation in miniemulsion polymerization conditions, the size of the

particles (typically in the nanometer range) has to be taken into account to limit the UV radiation attenuation by scattering. An efficient irradiation, which should ideally reach every droplet, is the key factor to ensure a faster polymerization rate and comparable solid contents to thermally based miniemulsion polymerization. In this context, continuous flow reactors could effectively substitute traditional stirred tank reactors, because the higher irradiation area for a shorter exposure time (to UV light) would increase the overall process efficiency. Miniemulsion has already been shown to be successful for photoinduced polymerization of organic monomers. Chemtob *et al* investigated the polymerization of acrylate monomers by using a free radical approach,¹⁸⁵ and Tonnar *et al.* controlled the radical polymerization of vinyl acetate in the presence of an iodinate macrophotoinitiator.¹⁸⁶

In Section 4.1 we reported the dual role of **Zr₄** within hybrid nanoparticles: as a catalytic site for sulfur oxidation reactions and as a cross-linking unit for the resulting matrix.⁵¹ Based on these considerations, we apply free radical photopolymerization for the synthesis of an organic–inorganic hybrid poly(MMA-*co*-**Zr₄**) nanoparticles. Three different radical photoinitiators based on carbonyl organic compounds were used. The photopolymerization of the hybrid nanoparticles was carried out in the confined space of direct (oil-in-water) miniemulsion droplets, and a kinetic study on the polymerization process was conducted. The obtained materials were compared with the nanoparticles previously produced by using azo-based thermal initiators.

4.3.2. Initiation of the Copolymerization and Particle Morphology

In Section 4.1, thermally initiated free radical polymerization in miniemulsion has been shown to be a suitable route for the synthesis of metal oxocluster-reinforced hybrid nanoparticles (poly(MMA-*co*-**Zr₄**)).⁵¹ In this section, in contrast, an analogous process was studied under photoactivated polymerization, that is, under the formation of initiator radicals through UV light irradiation. The photoactivated free radical polymerization was carried out by using three benzoin-based initiators (commercially known as Irgacure 2959, Irgacure 754, and Irgacure 369, referred to as **P1**, **P2**, **P3**, respectively). After photon absorption and excitation, these photoinitiators undergo α -dissociation (Norrish-type I cleavage), thus producing benzoyl-substituted benzyl free radicals (Scheme 4.4). The α -cleavage has been shown to proceed through triplet states whose lifetimes are drastically dependent on the substituent R.¹⁸⁷⁻¹⁹⁰ The three initiators were selected to

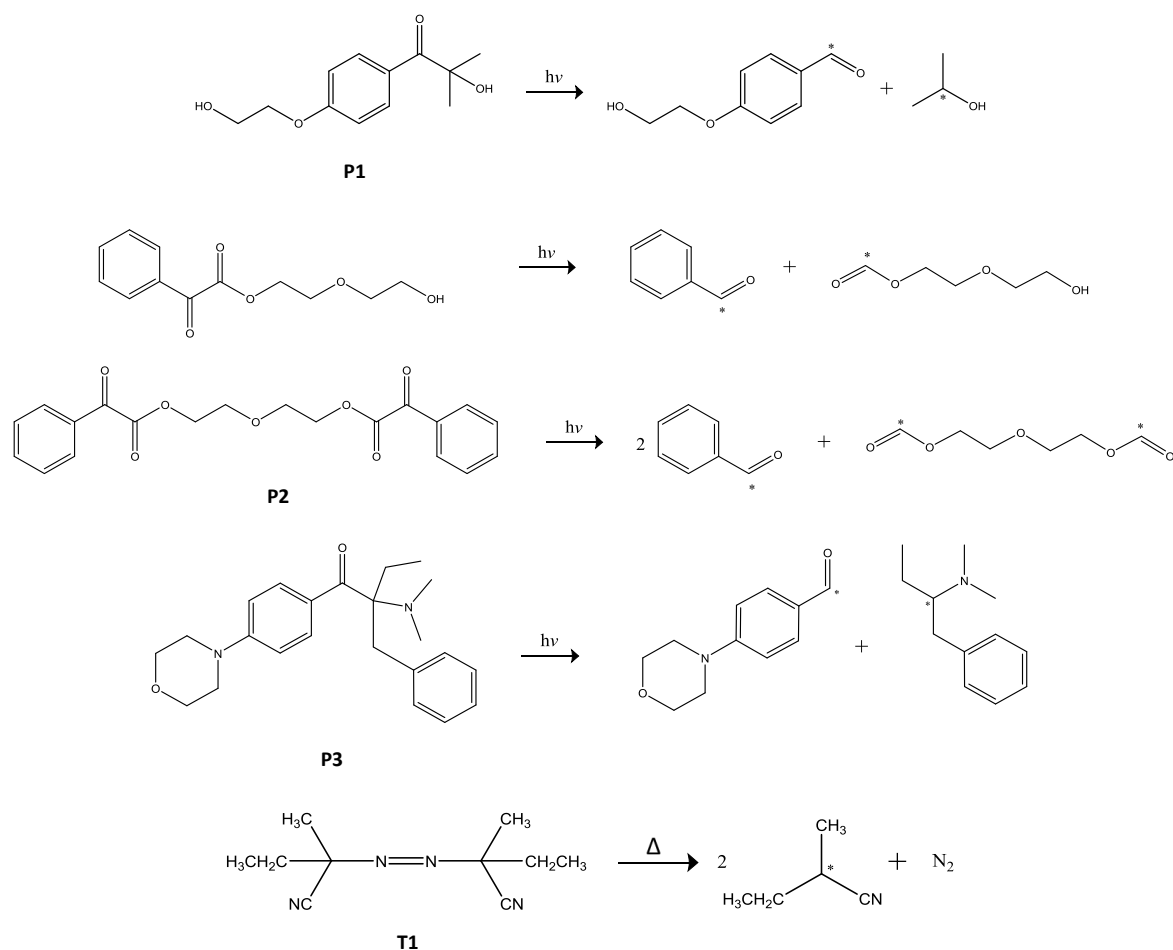
optimize the match between their intrinsic absorption and the emission spectra of the used UV lamp (UV Mercury HBO100 lamp, having the major emission peaks at 254, 297-302, 312-313, 334, 365 and 405 nm). **P1**, **P2**, and **P3** show absorption maxima at 273, 254, and 320 nm, respectively (Figure 4.29). Nanoparticles with different amounts of the oxocluster **Zr₄** (1, 3, 5, 7, and 10 wt% with respect to the total amount of monomers) and the different initiators were prepared, analyzing thereby the kinetics of the process and comparing the results with those obtained by using the thermal azo-initiator 2,2'-azobis-(2-methylbutyronitrile) (AMBN, referred to as **T1**, Scheme 4.4). While the synthesis of poly(MMA-co-**Zr₄**) hybrid nanoparticles with **P1** and **P2** was successful for all **Zr₄** contents (1, 3, 5, 7, and 10 wt%), by using **P3**, polymerization within the miniemulsion droplets was only possible for contents up to 7 wt% of **Zr₄**; differently, the use of 10 wt% of **Zr₄** as a comonomer led to the destabilization of the miniemulsion and to the formation of a coagulum due to polymerization in bulk.

The solid content of the photoactivated samples was in the range 12–17 wt%, values slightly lower when compared to the thermally activated samples (in the range 18–20%). The lower solid content of the photoactivated samples is likely to be caused by a more inhomogeneous initiation in miniemulsion systems when compared to thermal processes. While in the thermal initiation, the initiation step is likely to start homogeneously in each droplet at the same time due to identical temperatures, in the photopolymerization there is a geometrical influence of the position of the irradiation source, so that the initiation is higher in the side close to the lamp. Because of this inhomogeneous initiation, stirring plays an important role and, although the parameters were optimized to a maximum efficiency, a larger amount of coagulum was formed in the side of the cuvette where the UV lamp was placed. In general, a higher amount of coagulum for photoactivated samples was observed when compared to thermal initiation (ca. 10 wt% and 5 wt%, with respect to the monomer content, for photoinitiation and thermally activated samples, respectively), thus yielding a lower solid content.

The particle size is affected by the amount of incorporated **Zr₄** oxocluster, analogously to the results obtained by using thermal initiation. The interaction between the cluster and the surfactant, which lowers the interfacial tension between phases, results in a systematic increase of size with increasing amounts of **Zr₄**,⁵¹ as shown by DLS (Figure 4.30), and SEM measurements (Figure 4.31, Figure 4.32, and Figure 4.33 for nanoparticles synthesized by using **P1**, **P2** and **P3**, respectively). A relevant observation was the appearance of a significant number of particles with hollow structure during the

4.3. Zirconium Oxocluster/Polymer Hybrid Nanoparticles Prepared by Photoactivated Miniemulsion Copolymerization

photoactivated free radical polymerization. Since light is highly scattered by the presence of droplets in the emulsion, the polymerization most likely starts at the monomer–water interphase at the droplets edges, where the first initiator radicals are initiating the polymerization. Consequently, the particle formation will preferentially start from the interface towards the inner part of the monomer droplet, thus resulting in the formation of a shell, causing a hollow structure.



Scheme 4.4. Free radicals mechanisms formation for (a) Irgacure 2959 (**P1**), (b) Irgacure 754 (**P2**), (c) Irgacure 369 (**P3**), and (d) AMBN (**T1**).

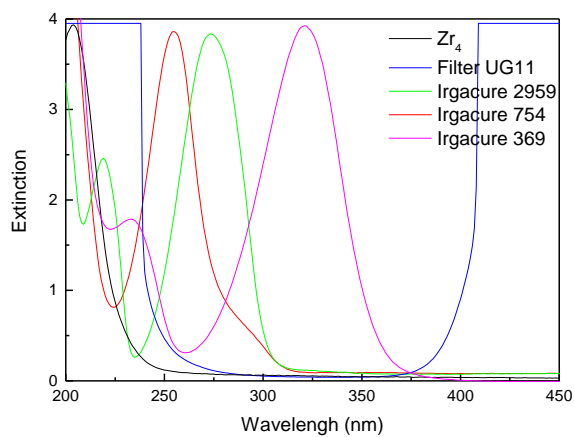


Figure 4.29. UV spectra of Irgacure 2959 (P1), Irgacure 754 (P2), Irgacure 369 (P3), and filter UG11.

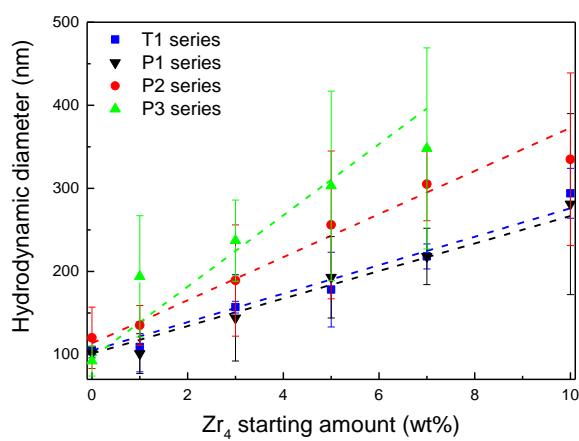


Figure 4.30. Hydrodynamic diameters of hybrid poly(MMA-co- Zr_4) nanoparticles in water suspensions determined by DLS as a function of oxocluster weight content.

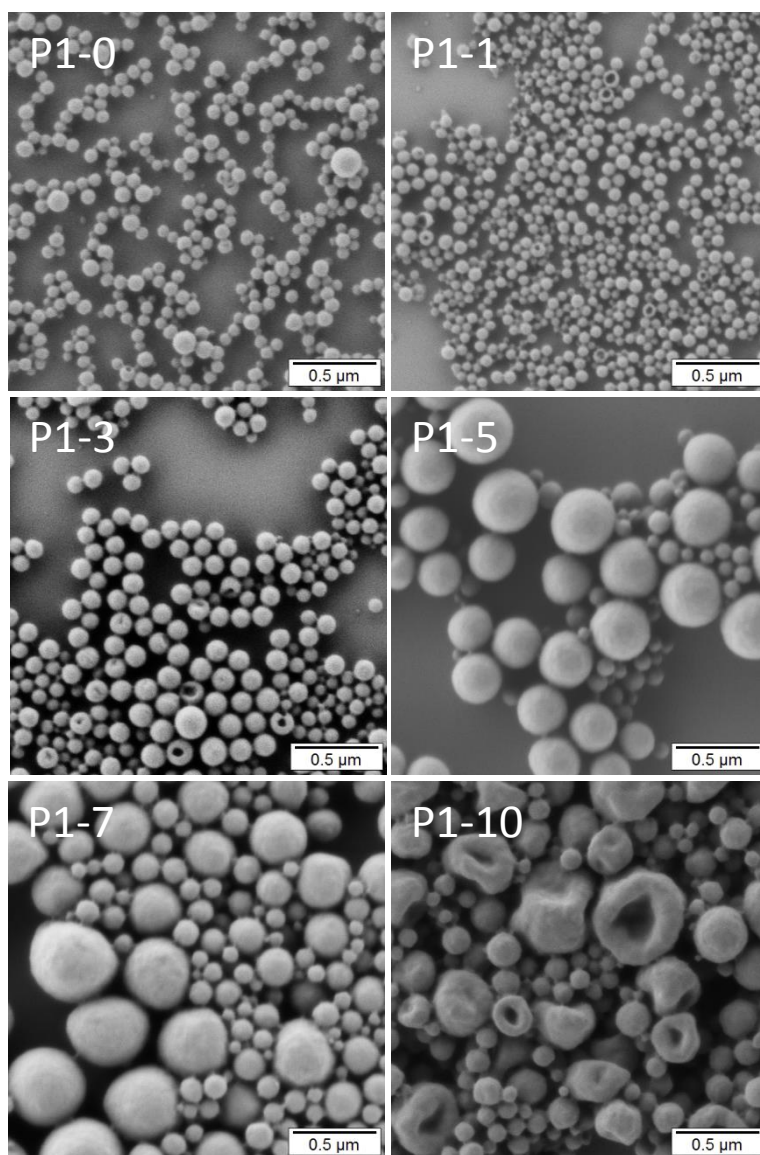


Figure 4.31. SEM images of hybrid poly(MMA-*co*-Zr₄) nanoparticles synthesized using Irgacure 754 (P1).

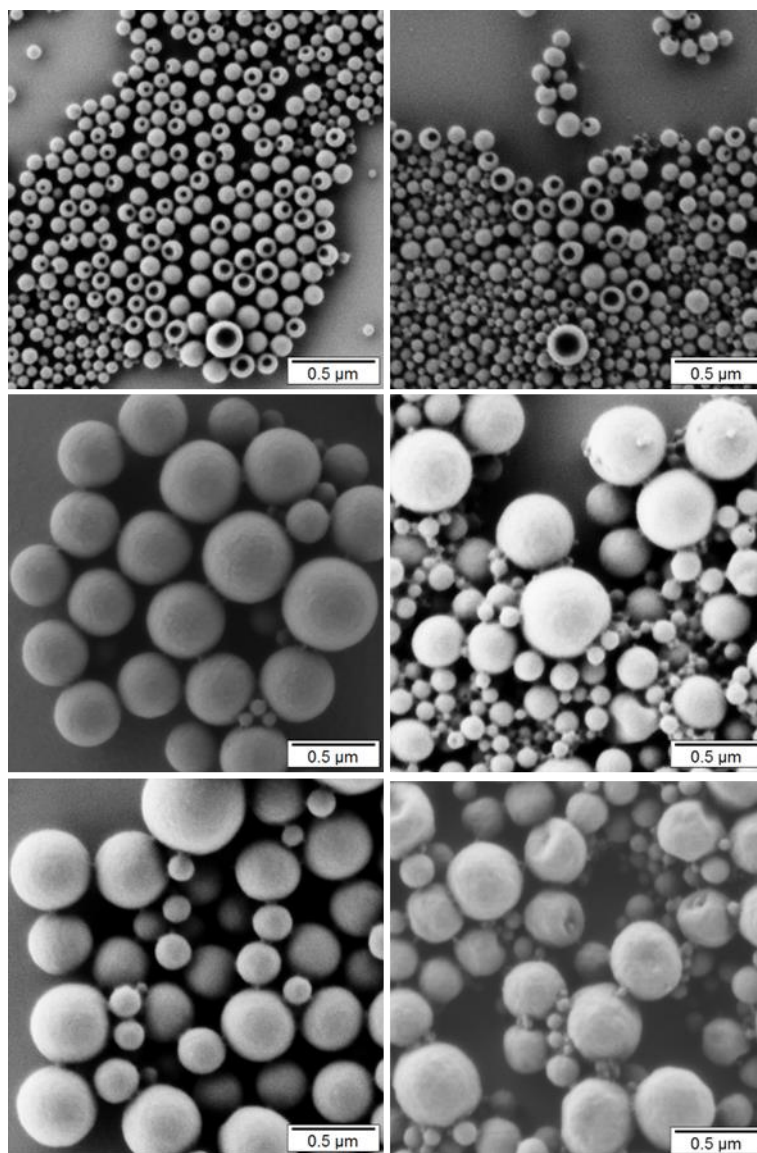


Figure 4.32. SEM images of hybrid poly(MMA-co-Zr₄) nanoparticles synthesized using Irgacure 754 (P2).

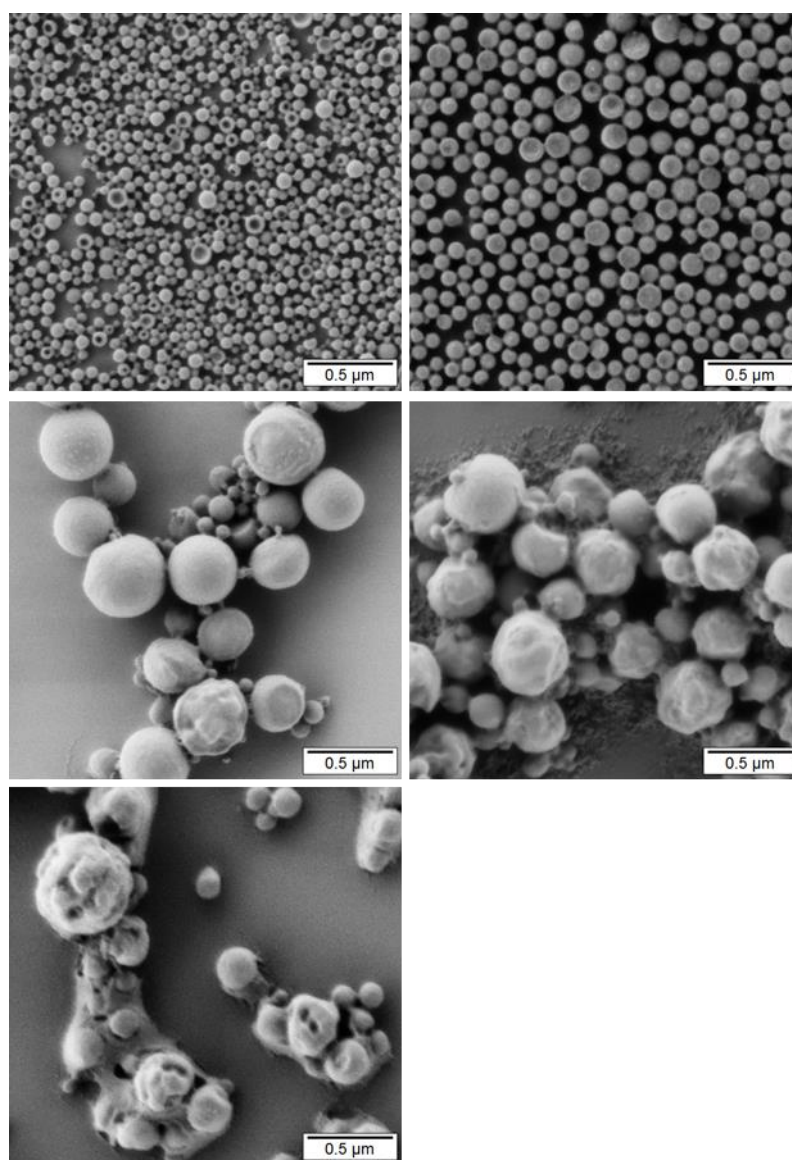


Figure 4.33. SEM images of hybrid poly(MMA-*co*-Zr₄) nanoparticles synthesized using Irgacure 369 (**P3**).

4.3.3. Compositions, Cross-Linking, and Thermal Properties

The actual content of Zr₄ in the synthesized hybrid nanoparticles was determined by inductively coupled plasma–optical emission spectrometry (ICP–OES). The Zr₄ detected values are consistent with the initially introduced contents for **P1-5**, **P2-5** and **T1-5** (where the first part of the sample label represents the initiator used and the following number indicates the nominal amount of Zr₄ in wt.%). A lower value was obtained for sample **P3-5**, which indicates a lower efficiency of the initiator **P3** in the copolymerization system. In contrast, samples prepared with 10 wt% of Zr₄ by photoinduced copolymerization (**P1-10** and **P2-10**) displayed a higher amount of oxocluster than the thermal polymerization sample **T1-10**, and all values were higher

than the nominal ones (Table 4.10), which is explained by the coagulum formed during the synthesis, as mentioned above. Moreover, ICP-OES measurements of the coagulum indicated almost no presence of Zr_4 (<0.3 wt%), which proves the very efficient incorporation of the zirconium oxocluster in the nanoparticles.

The experimental quantification of the insoluble cross-linked fraction was performed by GPC. In Figure 4.34, the cross-linked fractions of poly(MMA-*co*- Zr_4) nanoparticles are plotted as a function of the Zr_4 content. A general increase in the cross-linked fraction is observed when increasing the amounts of Zr_4 in the nanoparticles. Irrespective of the photoinitiator used, all series display a similar trend to the thermal initiation, with an initial increase up to 5% followed by a plateau region.

As expected, the copolymerization of MMA with Zr_4 affects also the thermal properties of the polymeric matrix. The glass transition temperature (T_g) of the samples synthesized with the photoinitiators **P1** and **P2** are in accordance with the one synthesized with **T1**. The zirconium-containing cross-linkers increase the glass transition temperature of the nanoparticle polymer matrix, as shown in Table 4.10. T_g measurements of the samples synthesized with the photoinitiator **P3** are not reported because of the low efficiency of the miniemulsion process when using this initiator.

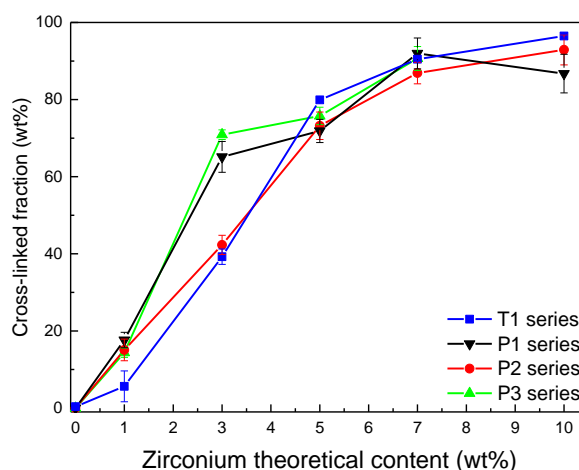


Figure 4.34. Cross-linked fraction (from GPC measurements) of hybrid poly(MMA-*co*- Zr_4) nanoparticles as a function of the Zr_4 content (determined by ICP-OES).

4.3. Zirconium Oxocluster/Polymer Hybrid Nanoparticles Prepared by Photoactivated Miniemulsion Copolymerization

Table 4.10. Synthetic details and main features of the cross-linked hybrid poly(MMA-*co*-Zr₄) nanoparticles presented in this section.

Sample ^[a]	Initiator	Nominal Zr ₄ content [wt%]	Actual Zr ₄ content [wt%] ^[b]	T _g [°C] ^[c]	k × 10 ³ [min ⁻¹] ^[d]	k _m [min ⁻¹ mol ⁻¹] ^[d]
P1-0	Irgacure 2959	0	0	99.3 ± 1.0	1.6	3.2
P1-5	Irgacure 2959	5	5.2 ± 0.5	105.1 ± 1.0	1.5	0.10
P1-10	Irgacure 2959	10	12.0 ± 0.4	111.1 ± 1.0	—	—
P2-0	Irgacure 754	0	0	98.4 ± 1.0	0.19	3.2
P2-5	Irgacure 754	5	4.9 ± 0.5	104.5 ± 1.0	0.21	0.18
P2-10	Irgacure 754	10	12.9 ± 0.5	110.3 ± 1.0	—	—
P3-0	Irgacure 369	0	0	—	—	—
P3-5	Irgacure 369	5	3.3 ± 0.5	—	—	—
T1-0	AMBN	0	0*	100.4 ± 3.0*	0.14	24
T1-5	AMBN	5	4.6 ± 0.5*	106.8 ± 0.5*	0.11	15
T1-10	AMBN	10	10.5 ± 0.5*	110.8 ± 1.8*	—	—

^[a] The first part of the label indicates the used initiator: Irgacure 2959 (**P1**), Irgacure 754 (**P2**), Irgacure 369 (**P3**), AMBN (**T1**); the numbers after the hyphen refer to the nominal Zr₄ weight percent. ^[b] Determined by ICP-OES. ^[c] Determined by DSC. ^[d] Apparent kinetic constants (cf. eq. 4.3–4.6). * Data taken from Benedetti *et al.*⁵¹

4.3.4. Polymerization Kinetics

The emulsions, submitted either to UV irradiation or to heating (72 °C) for the polymerization, were analyzed at different polymerization times up to complete conversion of the present double bonds by attenuated total reflectance infrared (ATR-FTIR) spectroscopy (Figure 4.35). This method has been already extensively used to follow the degree of polymerization as a function of time.^{69, 97, 179} The peak corresponding to the C=C stretching vibration (1638 cm⁻¹) is decreasing in intensity upon polymerization, whereas the peak corresponding to the C=O vibration (1720 cm⁻¹) remains unaffected and, therefore, taken as a reference (see Figure 4.36). MMA conversion vs. time profiles in the absence (samples **P1-0**, **P2-0**, and **T1-0**) and in the presence of the oxoclusters at a nominal content of 5 wt% (samples **P1-5**, **P2-5**, and **T1-5**) are shown in Figure 4.37.

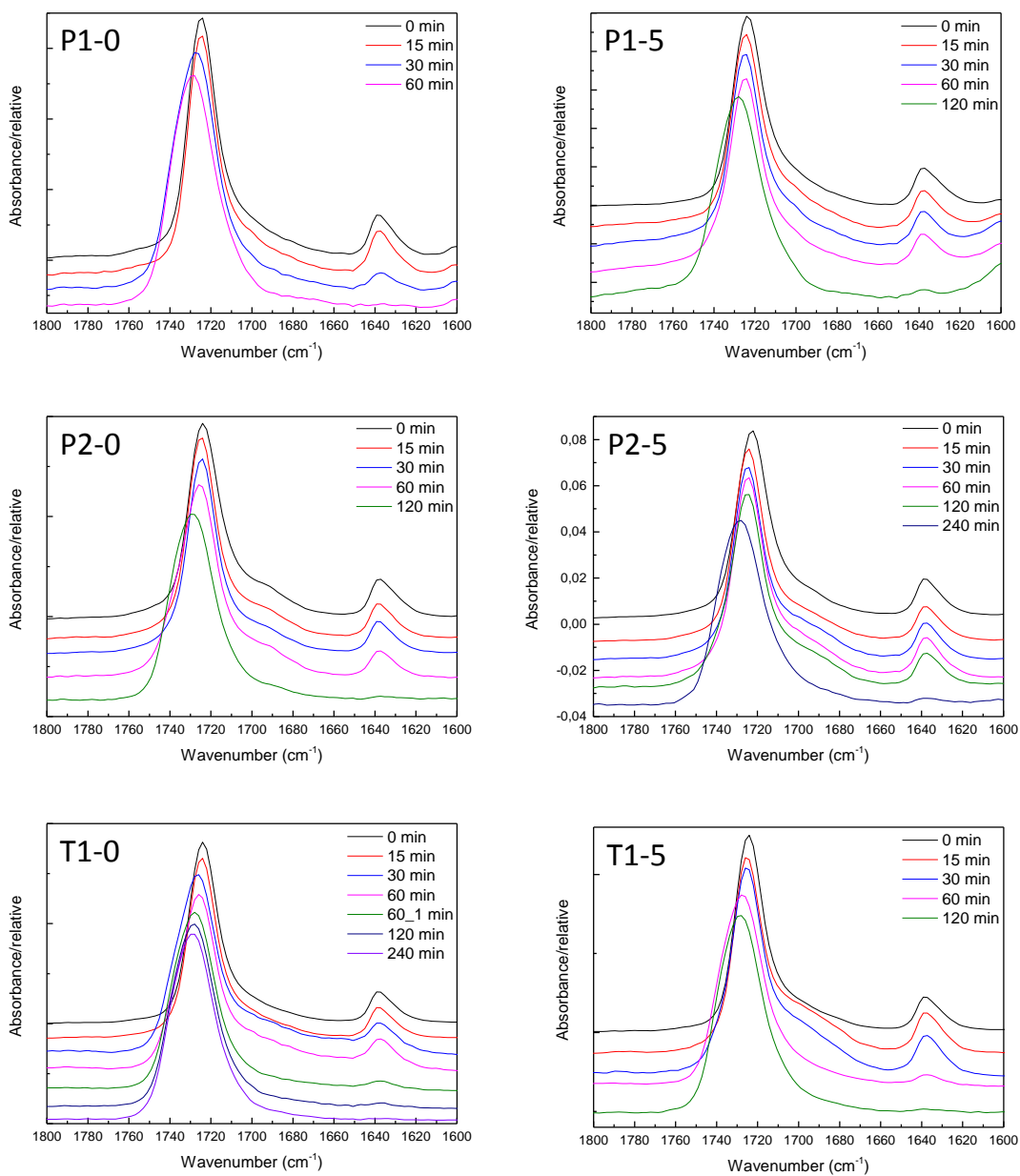


Figure 4.35. FTIR ATR spectra for the samples **P1-0**, **P1-5**, **P2-0**, **P2-5**, **T1-0** and **T1-5**, from 0s to complete polymerization conversion.

4.3. Zirconium Oxocluster/Polymer Hybrid Nanoparticles Prepared by Photoactivated Miniemulsion Copolymerization

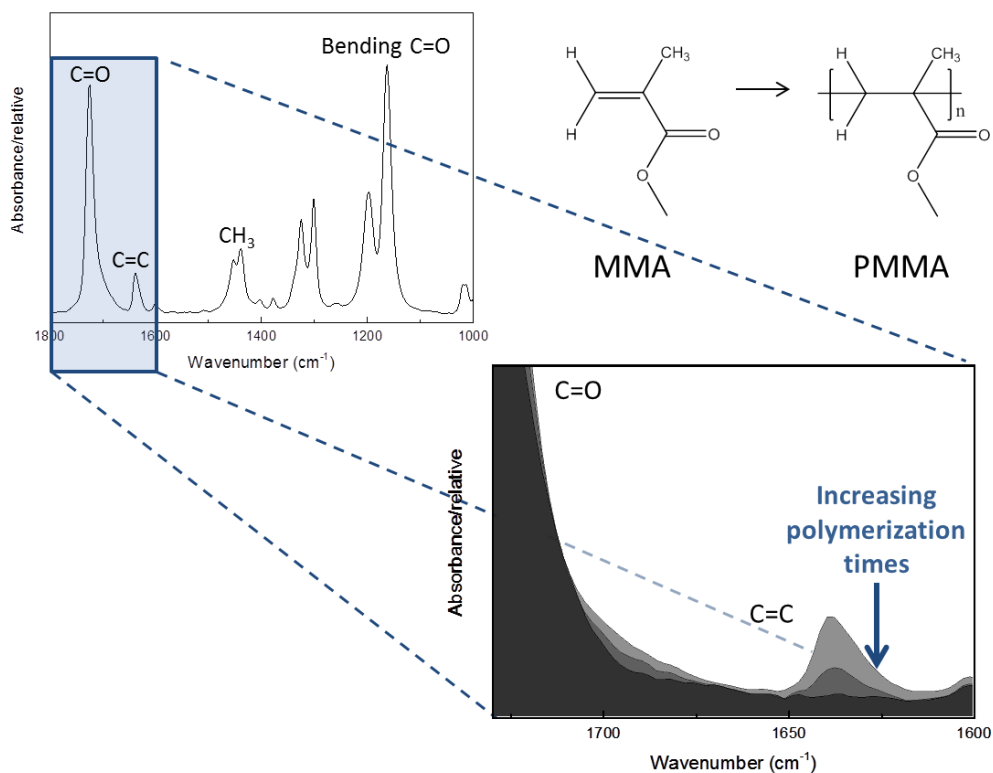


Figure 4.36. Typical IR spectra of poly(MMA-co-Zr₄) nanoparticles (top left) and the evolution of the C=C peak during the polymerization (bottom right).

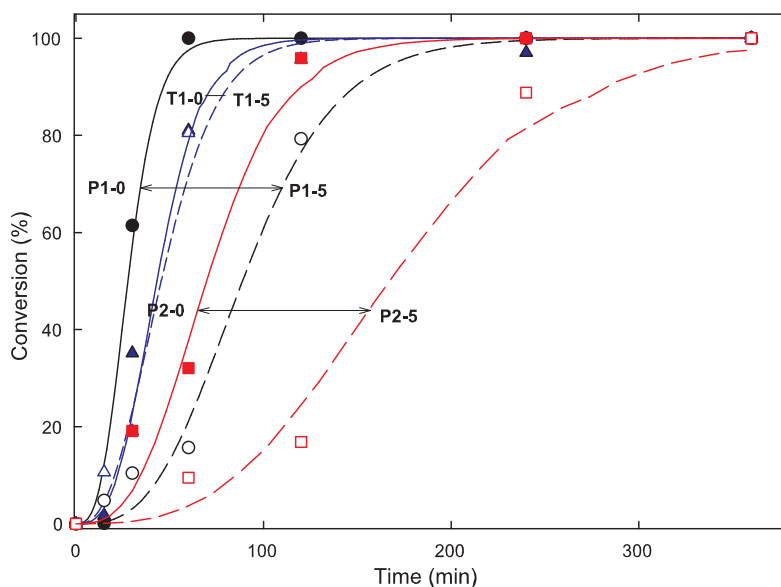


Figure 4.37. MMA conversion as a function of time for the polymerization process in PMMA (samples P1-0, P2-0, T1-0) and hybrid poly(MMA-co-Zr₄) (P1-5, P2-5, T1-5) nanoparticles: P1-0 and P1-5, black full and hollow circles, respectively; P2-0 and P2-5, red full and hollow squares, respectively; and T1-0 and T1-5, blue full and hollow triangles, respectively. Solid curves (polymer samples) and discontinuous curves (polymer/oxocluster hybrid samples) are calculated by least-square fitting of experimental data to the model given by eq. 4.6.

According to the experiments, MMA conversion rate decreases in the orders **P1-0** > **T1-0** > **P2-0** and **T1-5** > **P1-5** > **P2-5**, in the absence and in the presence of the oxocluster, respectively. The following simplified polymerization mechanism is proposed to rationalize the experimental results:



The polymerization mechanism is simplified to three steps: eq. 4.3 corresponds to the radical cleavage of the studied initiators, eq. 4.4 is related to the primary interaction of initiator radicals with a monomer M, and eq. 4.5 indicates the polymer bulk chain propagation itself. The growing polymer chain is represented as PC·. Termination reactions have been omitted, as no information about products is available. In all calculations, the coefficient k_p , related to the bulk propagation, was taken equal to $10^3 \text{ s}^{-1} \text{ mol}^{-1}$, which is a typical order of magnitude for radical chain propagation whereby vinylic units polymerize. The mathematical model associated to the mechanism is given by:

$$\frac{d}{dt} \begin{pmatrix} [A_2] \\ [A \cdot] \\ [M] \\ [PC \cdot] \end{pmatrix} = \begin{pmatrix} -1 & 0 & 0 \\ 2 & -1 & 0 \\ 0 & -1 & -1 \\ 0 & 1 & 0 \end{pmatrix} \times \begin{pmatrix} k[A_2] \\ k_m[A \cdot][M] \\ k_p[PC \cdot][M] \end{pmatrix} \quad (4.6)$$

The value of the apparent rate coefficients, k and k_m , were estimated from the least-squares fitting of experimental conversions to those calculated from MMA concentrations obtained integrating the differential equation of eq. 4.6. Table 4.10 contains the empirical results, which suggest that the photoinitiator **P1** leads to a faster polymerization than **P2** because of a higher photochemical cleavage efficiency (k values differs in an order of magnitude). Moreover, k_m apparent rate coefficients are always smaller for **Zr₄**-containing samples. Thermally initiated reactions do not appear to be influenced by the oxocluster presence; they exhibit the highest k_m value, being more

efficient than those photochemically initiated, with the exception of **P1-0**. The photon scattering produced by oxoclusters located on the water/oil interface is the most likely explanation. Indeed, the interaction photoinitiator/MMA is favored (higher k_m values) in the absence of oxoclusters, whereas thermal **T1** initiation seems to proceed homogeneously over the whole volume of the oil phase. The higher scattering is confirmed by the dilution of miniemulsion droplets containing MMA/hexadecane and MMA/**Zr₄**/hexadecane (with the same ratio used for the synthesis of PMMA and poly(MMA-*co*-**Zr₄**) nanoparticles, respectively) in an SDS aqueous solution ($3 \text{ g}\cdot\text{L}^{-1}$). Upon dilution, MMA droplets decrease in size until the monomer becomes nearly soluble in the continuous phase, leading to a transparent solution (Figure 4.38). In contrast, in the case of hybrid droplets, upon dilution, a turbid emulsion is obtained, as a result of a partial solubility of the oxocluster in the MMA/SDS/water system. Indeed, being the cluster not fully soluble in MMA at contents above 3 wt%, it can be present in the form of aggregates that lead to a higher scattering, when compared to pristine PMMA system.

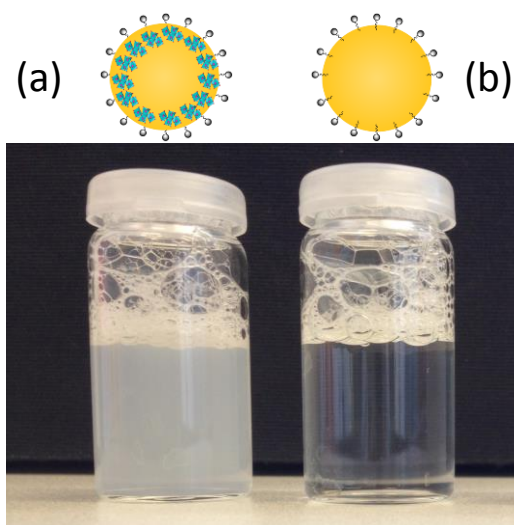


Figure 4.38. Diluted miniemulsion ($100 \mu\text{L} : 4 \text{ mL}$) with SDS water solution ($3 \text{ g}\cdot\text{L}^{-1}$) of (a) MMA/**Zr₄**/Hexadecane and (b) MMA/Hexadecane.

4.3.5. Conclusions

Photoinduced miniemulsion copolymerization has been shown as a suitable technique for the preparation of hybrid poly(MMA-*co*-**Zr₄**) nanoparticles. The formation of a chemical bond between organic and inorganic counterparts is achieved by using photoinitiators, with **Zr₄** acting as an efficient cross-linking unit. The use of the commercial benzoin-

type photoinitiators allowed an efficient incorporation of the inorganic guest into the resulting polymer matrix. Cross-linking efficiency, thermal properties and morphology are comparable to the hybrid nanoparticles synthesized with the typical thermal initiator 2,2'-azobis-(2-methylbutyronitrile). In spite of a less homogeneous initiation (when compared to thermal initiation) and the limitations introduced by scattering, photopolymerization represents a convenient alternative to thermal initiation in cases in which the latter cannot be applied and when the homogeneity of the final sample is less important than energetic factors.

4.4. Hybrid Nanocapsules as a Potential Nano-Thermometer System

In Section 4.1 and 4.3, $Zr_4O_2(\text{methacrylate})_{12}$ has proved to be an efficient cross-linking unit for the resulting PMMA based nanoparticles matrix. Based on the synergic result obtained, in this section $Zr_4O_2(\text{methacrylate})_{12}$ is used in combination with amphiphilic monomers, thus forming a cross-linked thermoresponsive nanocapsules shell. Hybrid/polymer nanocapsules that enclose Nile red are prepared by free radical copolymerization in direct miniemulsion. Because of the different LCST displayed, *N*-Isopropylacrylamide (NIPAM) and *N*-Isopropylmethacrylamide (NIPMM) are investigated as organic comonomers with the ability to endow the resulting nanoparticles with thermoresponsive properties. The encapsulated Nile red displays the possibility to trigger the “on-off” switching of its fluorescence intensity according to the temperature of the media in which the nanocapsules are dispersed. The prepared nanocapsules could be potentially applied as thermometers at the nanometric level.

4.4.1. Introduction

As introduced in Section 4.2, the peculiar thermoresponsive behavior of poly(*N*-isopropylacrylamide) (PNIPAM),^{149, 152} which allows the polymer chain to undergo a volume phase transition (VPT),¹⁴⁹ has been extensively studied both experimentally^{147-148, 154, 191-197} and computationally.^{150-151, 198-203} Its LCST at around 32 °C can be easily tuned by adding suitable of comonomers (i.e., it can be increased and decreased inserting hydrophilic and hydrophobic moieties, respectively),^{151, 204-206} salts^{201, 207-209} and changing the pH value (if a weak acid is used as a comonomer, *e.g.*, acrylic acid).²¹⁰⁻²¹² Moreover, what makes PNIPAM and related copolymers interesting in terms of

applicability is an LCST around human body temperature.²¹³ Hence, PNIPAM materials are potentially applicable for a range of biomedical applications.²¹⁴⁻²¹⁶ The most known polymer among the polyalkylmethacrylamides is PNIPAM, but also other family members displays LCSTs in an “appealing” range of temperature: poly(*N-n*-propylacrylamide) (PNnPA) at around 24 °C,²¹⁷ poly(*N-n*-propylmethacrylamide) (PNnPMA) at around 28 °C,²¹⁸ and poly(*N*-isopropylmethacrylamide) (PNIMAM) between 38 and 44 °C.²¹⁹⁻²²² The presence of one additional methyl group in the PNIMAM chains causes the restraining of the intra-chain collapse and inter-chain association, thus increasing the LSCT of this polymer by about 10 °C with respect to PNIPAM.²²¹

Polyalkylmethacrylamide-based polymers display a volume phase transition as a result of the amphiphilic nature of their monomer: the propyl and the amide moieties are hydrophobic and hydrophilic, respectively. Consequently, cross-linked particles based on these monomers display interesting reversible stimuli-responsive properties in aqueous dispersion. Hydrophilic interactions are dominant at temperatures below the LCST, thus keeping water molecules inside the polymer network; whereas above the LCST, hydrophobic interactions cause the expulsion of water from the network.

In this regard, the addition of inorganic cross-linkers is motivated by the endeavor to provide enhanced structural and functional properties to the resulting thermosensitive organic–inorganic hybrid matrix.^{16, 27, 223} Moreover, the presence of metal atoms offers the possibility to detect hybrid systems in a wide variety of media with a simple elementary analysis.^{114, 224-225} In Section 4.1 we reported the synergic outcome provided by the use of **Zr₄** as cross-linker.⁵¹ Metal oxocluster with 6 to 24 polymerizable bidentate organic ligands (RC(O)O⁻) can trigger a high cross-linking for the resulting polymer matrix.^{15, 51, 63-64, 78, 90, 98-99, 220} Cross-linked polymers, being no longer soluble, typically swells upon immersion in suitable solvents, thus becoming suitable for applications such heterogeneous catalysis,^{51, 93} drug delivery,²²⁶⁻²²⁷ and as magnetic hydrogels.²²⁸

In this section, polyalkylmethacrylamide monomers are copolymerized with **Zr₄** oxocluster at the interface of direct miniemulsion droplets. The resulting morphology is characterized by a hybrid/polymer thermoresponsive hydrophilic shell, which encloses a hydrophobic inner core. Specifically, we report the encapsulation of the hydrophobic fluorescent organic dye 9-diethylamino-5-benzo- α -phenoxazinone (more known as Nile red, in the following labeled as NR) in hybrid nanocapsules based on *N*-isopropylacrylamide or *N*-isopropylmethacrylamide. The use of different contents of **Zr₄**

oxocluster ensures (i) a different cross-linking degree and (ii) a shift of the LCST. NR is well known to drastically decrease its fluorescence in polar solvents and to be non-fluorescent in aqueous solutions; however, it is fluorescent in organic solvents, surfactant micelles,²²⁹ and when adsorbed on polymers, such as PNIPAM.²³⁰⁻²³¹ Moreover, the combination of NR with PNIPAM copolymers has been shown to display an interesting light-triggered “on–off” switching of fluorescence in aqueous solution.²³²⁻²³³ The swollen state below the LCST is characterized by hydrophilic interaction, thus quenching fluorescence, whereas above the LCST, when the polymer matrix is shrunken, fluorescence will be displayed. Based on these considerations, the synthesized cross-linked hybrid nanocapsules could be applied as a nano-thermometer system.²³⁴⁻²³⁸

4.4.2. Nanocapsule Synthesis

The direct miniemulsion technique was implemented for the synthesis of cross-linked hybrid poly(NIPAM-*co*-**Zr₄**) and poly(NIPMM-*co*-**Zr₄**) nanocapsules. A mixture of organic monomer (NIPAM or NIPMM), **Zr₄** oxocluster, the initiator (AMBN), and the hydrophobic osmotic pressure agent (hexadecane) were dissolved in a solution of NR in toluene. The two organic monomers were investigated due to the different LCST of the resulting polymer matrix as reported in literature.^{149, 219} Toluene was chosen because of its ability to dissolve all the above mentioned components, including the monomers, but not the forming polymer matrix, and for its possibility to be removed by freeze-drying. In particular, the insolubility of the growing polymer chain triggers its formation at the oil-water interphase, thus resulting in a capsular morphology. Once the polymerization of the shell is terminated, the inner core is characterized by the presence of the solution of NR in toluene. Furthermore to ensure only the presence of the nanocapsules matrix enclosing the hydrophobic inner core, dialysis was performed to remove unreacted monomer, surfactant in excess, not encapsulated dye, oligomers and/or short polymer chains shorter than 14,000 g·mol⁻¹.

4.4.3. Composition and Morphology

Different amounts of **Zr₄** (1, 5, and 10 wt%) and the anionic surfactant sodium dodecyl sulfate (SDS) were used for the miniemulsion synthesis (Table 4.11). After polymerization, the actual content of **Zr₄** in the resulting nanocapsules was determined by ICP-OES.¹¹⁴ Although in the case of poly(NIPAM-*co*-**Zr₄**) nanocapsules the detected

values are lower with respect to the nominal amount of introduced oxocluster content, the value follows the same incorporation increase up to 10 wt%. In contrast, for poly(NIPMM-*co*-Zr₄) nanocapsules the maximum Zr₄ incorporation was reached for sample **M5** (where the first letter of the sample label represents the monomer used, *i.e.*, **A** and **M** for NIPAM and NIPMM, respectively; and the following number is the nominal amount of Zr₄ in wt%). Sample **M10** showed instead a decrease in the detected Zr₄ amount, evidencing that not all of the oxocluster was incorporated. The further incorporation attempt was not successful because of the relatively high amount of clumps detected during the synthesis (60-70 wt% with respect to the initial synthesis amounts). Amounts higher than 5 wt% of Zr₄ combined with NIPMM as comonomer, resulted in a destabilization of the miniemulsion droplet system.

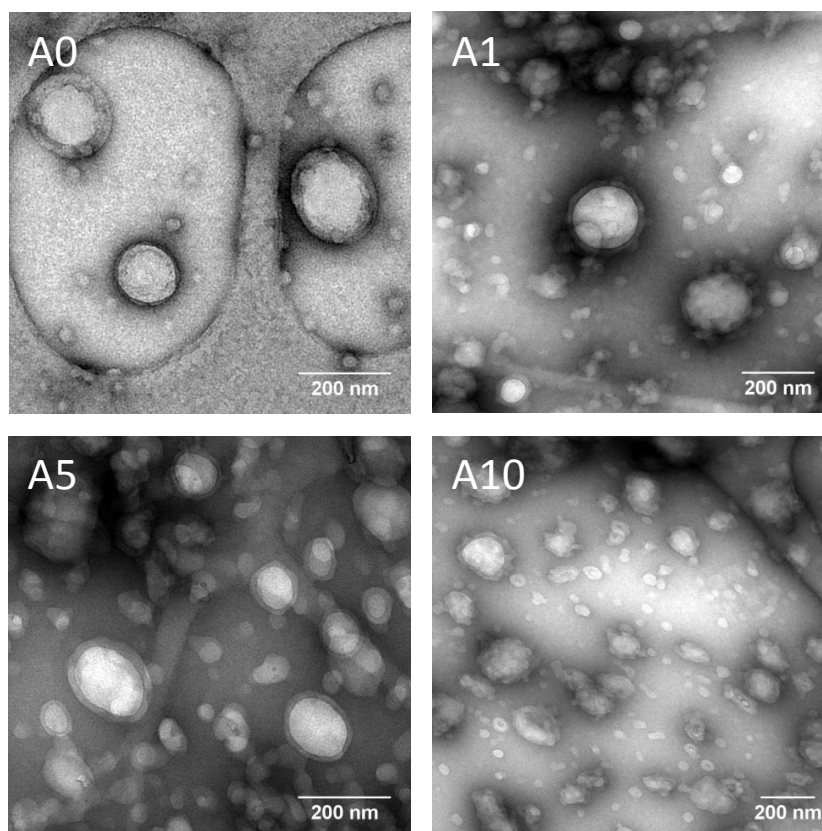
The determination of the cross-linked fraction was performed by GPC. Freeze-dried nanocapsules were redispersed in DMF and then centrifuged. The sedimentation of the insoluble cross-linked nanocapsules allows the evaluation of the soluble fraction in the supernatant, and as a consequence (by subtracting it from the initial amount dispersed in DMF) the cross-linked fraction. For both nanocapsules systems, a general increase in the cross-linked fraction with increasing Zr₄ amounts is observed (Table 4.11). Nevertheless, poly(NIPAM-*co*-Zr₄) nanocapsules present a higher cross-linking efficiency than the poly(NIPMM-*co*-Zr₄) ones. The cross-linking fraction follows an analogous trend to the one observed by copolymerizing the same oxocluster with methylmethacrylate (*i.e.*, a rapid increase at lower cluster content followed by a plateau-like region).⁵¹ However, in case of **M10**, only about 53 wt% of the matrix could be cross-linked. Even lower is the cross-linking efficiency for poly(NIPMM-*co*-Zr₄) nanocapsules: about half of the one observed for the NIPAM-based nanocapsules at the highest Zr₄ content.

The nanocapsule morphology was visualized by TEM. (Figure 4.39 and Figure 4.40 for poly(NIPAM-*co*-Zr₄) and poly(NIPMM-*co*-Zr₄) nanocapsules, respectively). Indeed, using this method it is possible to distinguish the higher density of the nanocapsule shell from the inner core, consisting in the NR solution. Besides the presence of nanocapsules, both systems are characterized by a high polydispersity and the presence of smaller agglomerates. More evident for the NIPAM-based system is the presence of a “rougher” surface of the capsule shell for samples characterized by higher amounts of embedded Zr₄. The presence of aggregates within the nanocapsules shell is attributable to the presence of the oxocluster, and it seems to be in agreement with the findings on cluster distribution within the particles synthesized using Lutensol AT50 in Section 4.1.3.

Table 4.11. Synthetic details and main features of the cross-linked hybrid poly(NIPAM-*co*-Zr₄) and poly(NIPMM-*co*-Zr₄) nanocapsules.

Sample ^[a]	Comonomer	Zr ₄ content as comonomer (wt%)	Actual Zr ₄ content (wt%) ^[b]	Cross-linked fraction (wt%) ^[c]
A0	PNIPAM	0	0	0
A1	PNIPAM	1	0.79 ± 0.01	10.5
A5	PNIPAM	5	3.68 ± 0.01	47.6
A10	PNIPAM	10	6.92 ± 0.01	52.3
M0	PNIPMM	0	0	0
M1	PNIPMM	1	0.91 ± 0.02	0
M5	PNIPMM	5	4.24 ± 0.01	22.4
M10	PNIPMM	10	2.39 ± 0.02	27.4

^[a] The letters in the sample codes refer either to NIPAM (**A**) or to NIPMM (**M**), used as comonomers; the numbers refer to the Zr₄ weight percent (*e.g.*, **M1** represents the sample prepared with NIPMM and 1 wt% of Zr₄); ^[b] determined by ICP-OES; ^[c] determined by GPC on supernatants.

**Figure 4.39.** TEM images of the cross-linked hybrid poly(NIPAM-*co*-Zr₄) nanocapsules. The samples were embedded in trehalose and negatively stained with uranyl acetate.

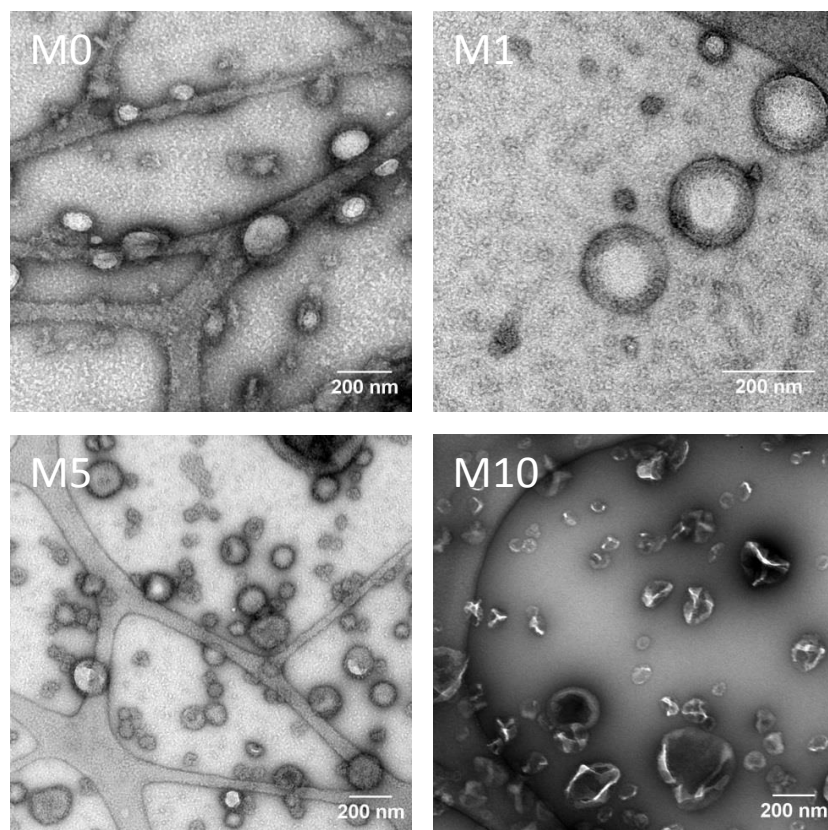


Figure 4.40. TEM images of the cross-linked hybrid poly(NIPMM-*co*-Zr₄) nanocapsules. The samples were embedded in trehalose and negatively stained with uranyl acetate.

Although this case is not related to the interactions between Zr₄ and Lutensol AT50, the presence of the inorganic monomer in specific located areas is rather due to the higher hydrophilicity of the resulting cross-linked PNIPAM polymer matrix. The oxocluster, being more hydrophobic, tends to separate from the forming hydrophilic matrix, thus gathering in aggregates. In contrast, in case of poly(NIPMM-*co*-Zr₄) nanocapsules, the lower presence of oxocluster incorporated results in a less pronounced shell “roughness”.

To confirm the retention of the oxocluster structure after the polymerization, cross-linked hybrid poly(NIPAM-*co*-Zr₄) nanocapsules were analyzed by X-ray absorption (XAS) measurements at Zr K-edge. Fourier transforms of the extended X-ray absorption fine structure (EXAFS) curves of samples A10 and A10 after one week in water dispersion are compared to the pristine Zr₄ oxocluster (Figure 4.41). The difference between the reference Zr₄ and A10 is minimal, which indicates that there is no relevant distortion in the oxocluster structure upon embedding. After keeping sample A10 for a week in nanocapsules water dispersion, a minor distortion in the second shell (at roughly 3.5 Å, corresponding to the Zr-Zr distance) could be observed. Although this minor distortion, the spectrum of A10 after one week in dispersion closely resembles the one of the pure oxocluster, thus suggesting that the oxocluster has retained its structure.

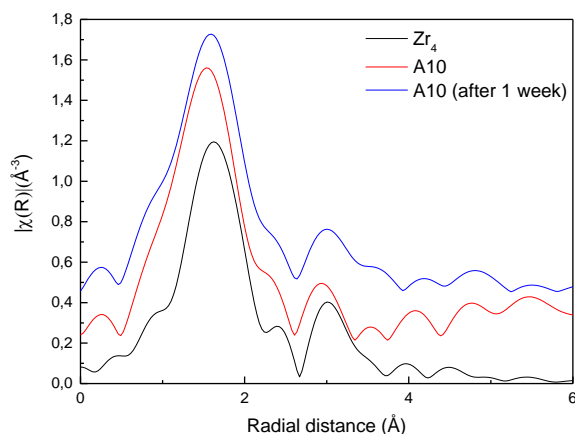


Figure 4.41. Fourier transforms of the EXAFS spectra for poly(NIPAM-*co*-**Zr₄**) nanocapsules containing 10 wt% of **Zr₄** compared to the **Zr₄** as a reference. Data non-corrected for phase shift.

4.4.4. Thermoresponsive Fluorescence Behavior

The thermoresponsive behavior of poly(NIPAM-*co*-**Zr₄**) and poly(NIPMM-*co*-**Zr₄**) nanocapsules was determined by following the evolution of the system as a function of temperature by DLS in a temperature range from 20 to 60 °C. Figure 4.42 shows the hydrodynamic diameter (D_h) as function of temperature. Samples prepared with the lowest cluster incorporation (samples **A1** and **M1**), being less affected by the presence of the inorganic comonomer, showed a difference in the LCST of about 10 °C, as reported in literature.²²¹ For sample **A10**, the higher amount of inorganic cross-linker resulted in an increase of LCST (~7 °C). Whereas, for the analogous sample prepared with NIPMM (**M10**) no considerable shift was observed. The similar LCST for all poly(NIPMM-*co*-**Zr₄**) nanocapsules with different oxocluster amount is likely due to: (i) the lower cluster incorporation, as well as (ii) the lower resulting cross-linking efficacy.

Although temperature-dependent DLS measurements showed that poly(NIPMM-*co*-**Zr₄**) nanocapsules undergo a volume phase transition at about 45 °C, no change in the fluorescence signal was detected upon temperature change. Therefore, this system is not further discussed. In contrast, poly(NIPAM-*co*-**Zr₄**) nanocapsules showed an increase of fluorescence intensity when temperature was higher than their LCST. As discussed in the motivation of this section, NR is known to display fluorescence in hydrophobic environment, whereas it does not fluoresce in aqueous solution.²²⁹ A aqueous solution of NR in the presence of a PNIPAM copolymer has already shown absence of fluorescence at room temperature. On the other hand, an intensity increasing was observed at

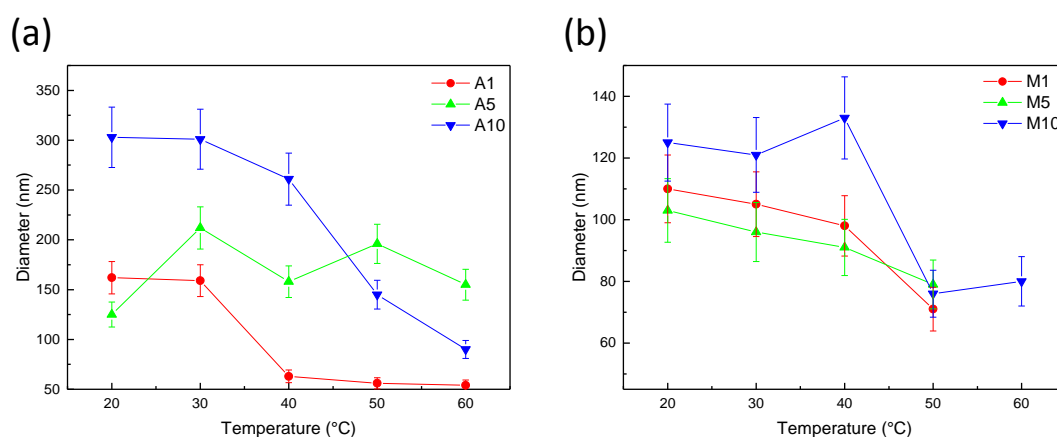


Figure 4.42. Hydrodynamic diameter (D_h) of (a) poly(NIPAM-*co*-Zr₄) and (b) poly(NIPMM-*co*-Zr₄) nanocapsules in water suspension as a function of temperature. The samples were prepared with 1, 5 and 10 wt% of Zr₄.

temperature higher than LSCT. Indeed, when the polymer is soluble (or swollen, in case it is cross-linked), the dye is exposed to water, thus drastically decreasing its fluorescence. Nevertheless, when increasing the temperature, the polymer structure becomes hydrophobic: while water molecules are expelled out, the dye molecules are gathered in the proximity of the shrunken polymer matrix and the fluorescence intensity increases by a factor of 5.²³³ However, in this work, NR is present inside the nanocapsules core. The fluorescence spectra of NR encapsulated in samples **A0** and in the hybrid cross-linked poly(NIPAM-*co*-Zr₄) nanocapsules (samples **A1**, **A5** and **A10**) in the temperature range 27 to 41 °C is reported in Figure 4.43a. The spectra are normalized to the maximum emission intensity at 41 °C. At 27 °C, an anti-Stokes shift (or blue shift) and a higher intensity of the maximum emission are observed with increasing Zr₄ amount in the nanocapsules. For sample **A0** at 41 °C, the intensity of the fluorescence signal is increasing by a factor of 2.48 with respect to the value at 27 °C, for the samples **A1** and **A5** the intensity is about double at 41 °C, while for sample **A10** the intensity is about 2/3 times lower at 27 °C (Table 4.12).

Table 4.12. Fluorescence maximum intensity at 27 °C and 41 °C of the cross-linked hybrid poly(NIPAM-*co*-Zr₄) nanocapsules with different amount of Zr₄.

Samples	Fluorescence Intensity (a.u.) at 27 °C ^[a]	Fluorescence Intensity (a.u.) at 41 °C	Ratio (Intensity at 27 °C / Intensity at 41 °C)
A0	1 ($\lambda_{em} = 635$ nm)	0.403 ($\lambda_{em} = 650$ nm)	2.48
A1	1 ($\lambda_{em} = 635$ nm)	0.544 ($\lambda_{em} = 645$ nm)	1.84
A5	1 ($\lambda_{em} = 635$ nm)	0.561 ($\lambda_{em} = 645$ nm)	1.78
A10	1 ($\lambda_{em} = 635$ nm)	0.687 ($\lambda_{em} = 640$ nm)	1.46

^[a] In order to compare the maximum peak of emission at 27 °C, different λ_{em} were taken due to the anti-Stokes shift observed increasing the amount of Zr₄.

The explanation of the lowering of the fluorescence intensity difference, with increasing cluster content, between 27 and 41 °C is likely due to the increasing cross-linking degree of the nanocapsules shell. For sample **A0**, the dye is not encapsulated anymore when the nanoparticles are transferred in water, because the shell is basically formed by a linear and therefore soluble polymer. At lower temperature, **A0** is composed by a solution of PNIPAM and NR in water. Nevertheless, by increasing the amount of cross-linker in the nanocapsules matrix, cross-linked shell nanocapsules are formed. In the presence of **Zr₄**, the shell does not dissolve but swells upon dilution in water, therefore keeping NR encapsulated. Higher amount of **Zr₄** leads to a more defined core-shell morphology, and therefore to a more solid dye encapsulation after redispersion in water. For this reason, the sealed NR, being in contact with the polymer matrix, increases its fluorescence emission intensity even at temperature below the LCST. In parallel, the better encapsulation of dye is also confirmed by the anti-Stoke shift observed. Indeed, the increasing cross-linking degree of the nanocapsules shell produces a higher non-polar character, thus shifting toward the blue the maximum emission of NR, as already reported in literature.²³⁹ The maximum fluorescence intensities are plotted for different temperature in the range from 27 to 41 °C (Figure 4.43b). Through this type of measurement, it is also possible to observe the thermoresponsive behavior of PNIPAM-based system. The data obtained are in agreement with the DLS measurement, showing a slight increase of LCST at the highest content of **Zr₄**.

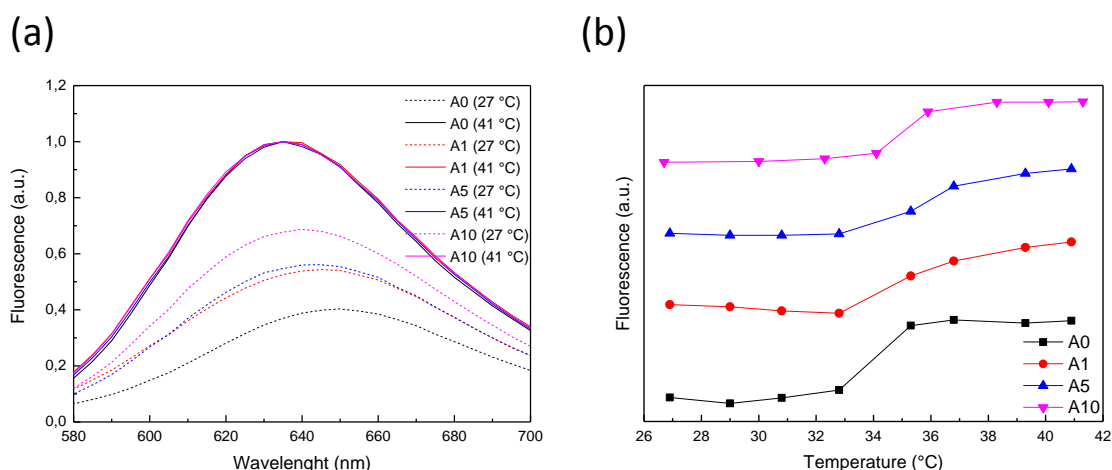


Figure 4.43. (a) Fluorescence emission spectra of PNIPAM nanocapsules and cross-linked hybrid poly(NIPAM-*co*-**Zr₄**) nanocapsules at 27 °C (dashed line) and 41 °C (straight line). (b) Plots of maximum fluorescence intensity versus temperature of PNIPAM nanocapsules and cross-linked hybrid poly(NIPAM-*co*-**Zr₄**) nanocapsules in water suspension. Hybrid nanocapsules were prepared with 1, 5 and 10 wt% of **Zr₄**. Concentration of nanocapsules: 2 mg·mL⁻¹. $\lambda_{\text{ex}} = 549$ nm, band widths: $\Delta\lambda_{\text{em}} = 20$ nm, $\Delta\lambda_{\text{ex}} = 20$ nm, $\lambda_{\text{em}} = 628$ nm [(for panel (b))].

To evaluate possible traces of NR leakage from the nanocapsules core, fluorescence measurements were performed on the particles dispersion supernatant after centrifugation at 40 °C. NR displays enhanced fluorescence only in presence of hydrophobic components, for instance in presence of linear PNIPAM above its LCST. Therefore the fluorescence measurement of the supernatant gives information about the presence of NR, but also about the presence of any polymer moieties remaining in solution after centrifugation. However, information regarding only the leakage of NR is obtained when the fluorescence of the supernatant is recorded in the presence of linear commercial PNIPAM (added after the centrifugation step). The fluorescence intensity of the supernatant decreases with increasing amount of Zr_4 , as observed in Figure 4.44. With increasing amount of cross-linker, lower amount of linear polymer moieties and lower amount of NR are present in solution, thus confirming the incorporation of the dye inside the core-shell morphology of the hybrid cross-linked nanocapsules.

Finally, hybrid cross-linked poly(NIPAM-*co*- Zr_4) nanocapsules containing NR were investigated by cycling the temperature between 32 and 41 °C forward and backward repeatedly (Figure 4.45). The “on-off” switching of fluorescence of encapsulated NR in hybrid cross-linked nanocapsules system can be reversibly tuned: low intensity (off-state) at 32 °C and augmented intensity at 41 °C (on-state).

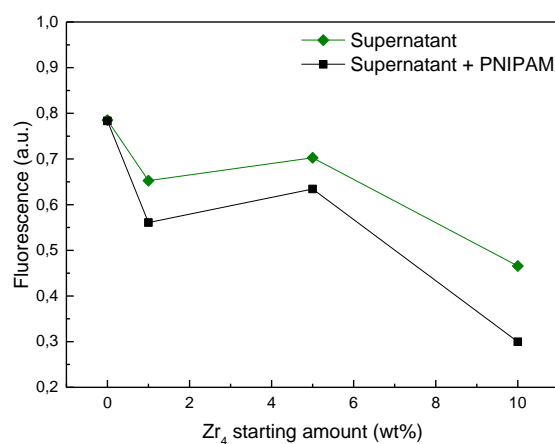


Figure 4.44. Plots of maximum fluorescence intensity versus Zr_4 initial amount as comonomer of nanocapsules dispersion supernatants after centrifugation step at 40 °C. The data are collect at 41 °C. Concentration of nanocapsules before centrifugation: 2 mg·mL⁻¹. $\lambda_{em} = 628$ nm, $\lambda_{ex} = 549$ nm, band widths: $\Delta\lambda_{em} = 20$ nm, $\Delta\lambda_{ex} = 20$ nm.

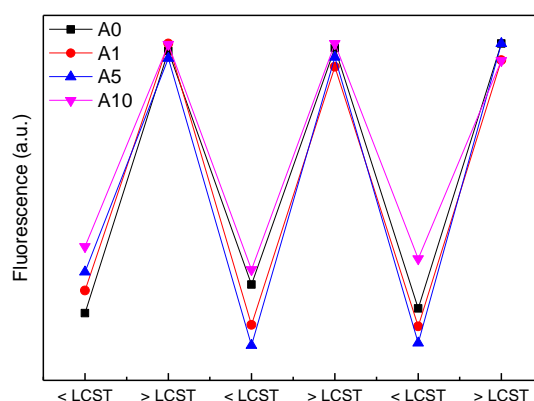


Figure 4.45. Reversibility of fluorescence of PNIPAM nanocapsules and cross-linked hybrid poly(NIPAM-*co*-**Zr₄**) nanocapsules in water suspension alternating temperature between 32 °C and 41 °C. Concentration of nanocapsules: 2 mg·mL⁻¹. $\lambda_{em} = 628$ nm, $\lambda_{ex} = 549$ nm, band widths: $\Delta\lambda_{em} = 20$ nm, $\Delta\lambda_{ex} = 20$ nm.

4.4.5. Conclusions and Outlook

The synthesis of hybrid cross-linked poly(NIPAM-*co*-**Zr₄**) and poly(NIPMM-*co*-**Zr₄**) nanocapsules enclosing Nile red has been reported. **Zr₄** is acting as a cross-linker unit for the resulting NIPAM- and NIPMM-based hybrid thermoresponsive matrix. Both hybrid nanocapsule types undergo a volume phase transition when temperature is increased above their LCST. In particular, the LCST of NIPMM-based nanocapsules seems not to be affected by the presence of **Zr₄**, whereas the LCST of poly(NIPAM-*co*-**Zr₄**) nanocapsules is dependent on the oxocluster content. The encapsulation of the dye fluorophore Nile red in poly(NIPAM-*co*-**Zr₄**) nanocapsules was also investigated by means of fluorescence. While the fluorescence intensity of the enclosed Nile red is weaker below the LCST, it increases when the hybrid capsules are in their shrunken hydrophobic state (above the LCST). Moreover, higher amount of cross-linker in the nanocapsules matrix enhances the permeability of the nanocapsules shell, thus preventing leakage of the dye from the nanocapsules core towards the aqueous media. Finally, the reversibility of the “on-off” switching of fluorescence intensity by alternating the nanocapsules dispersion temperature between 32 and 41 °C could be successfully demonstrated.

Because of their different LCSTs, a system formed by poly(NIPAM-*co*-**Zr₄**) nanocapsules having different cross-linking degree has the potential for being applied as Galileo-like thermometer on nanometric level (Figure 4.46).²⁴⁰ Thus, the intensity of the

fluorescence signal, being proportional to the concentration of the fluorescent nanocapsules, would be able to detect the temperature of the media in which the nanocapsules are present. Further experiments in this direction will be made using confocal laser scanning microscopy. In particular, our goal is to detect temperature as function of fluorescence signals of the different cross-linking degree hybrid nanocapsules.

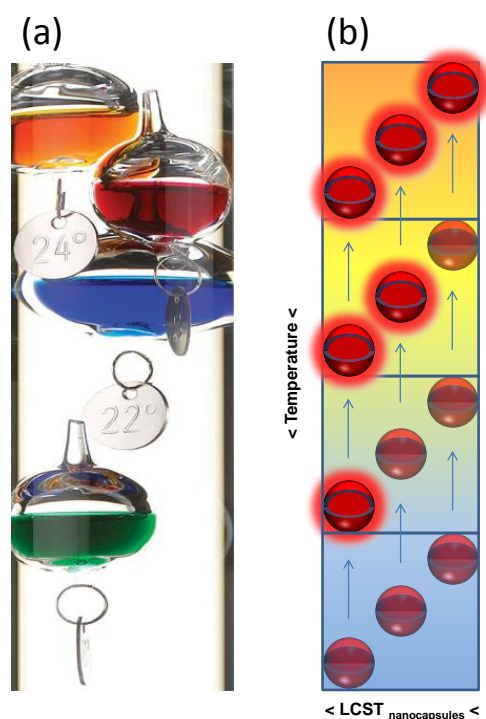


Figure 4.46. Picture of (a) Galileo thermometer^{vi} and (b) Galileo-like thermometer concept using cross-linked hybrid nanocapsules.

^{vi} Courtesy of <http://wordpress.mrreid.org/2013/07/07/galileo-thermometer/> (Feb. 2017)

5. Conclusions

This work has focused on colloidal nanoparticles of class II hybrid materials. In particular, the synthesis and application of metal oxocluster/polymer hybrid nanoparticles have been described. The formation of a covalent bond between the organic monomers and the functionalized metal oxocluster ensure the protection of the inorganic *guest* against hydrolysis phenomena. Miniemulsion polymerization has been proven to be a suitable technique to provide a homogeneous distribution of metal oxocluster molecules within the resulting hybrid/polymer matrix. Moreover, control on size and size distribution of the hybrid nanoparticles has been achieved. The nanometric dimension of the synthesized hybrid systems guarantees a higher surface area, an enhanced dispersibility, and processability with respect to materials synthesized in bulk. The main outcome is the synergic effect due to the incorporation of inorganic comonomer into a polymer matrix. On one hand, group 4 transition metal oxoclusters are endowed with high catalytic activity for the activation of hydrogen peroxide towards the oxidation of sulfur based compounds. On the other hand, because of the presence of several polymerizable moieties, they are outstanding building blocks for the preparation of organic–inorganic hybrid materials. Therefore, in **Section 4.1**, the synergic contribution of the metal oxocluster-based hybrid materials originates from the two-fold role of **Zr₄**: the oxoclusters act both as catalytically active species and as cross-linking units for the particles network. The synthesis and the successful application in heterogeneous catalysis of hybrid poly(MMA-*co*-**Zr₄**) nanoparticles has been reported. The presence of the oxocluster ensures enhanced thermal properties, and triggers a swelling behavior in organic solvents of the resulting cross-linked polymer matrix. It is also shown the significant impact of the use of two different surfactants on morphology, cross-linking efficiency, and catalytic performance. The successful application of hybrid poly(MMA-*co*-**Zr₄**) nanoparticles for the catalytic oxidation of sulfur-based compound by hydrogen peroxide is highlighted, confirming the advantages of a covalent bond with the polymeric matrix on reaction selectivity even after several cycles.

Section 4.2 addresses the absence of a covalent bonding between the two counterparts, which is the main peculiarity of class II hybrid materials, thus not bringing to any synergic outcome. Although $\text{Ti}_9\text{O}_8(\text{OPr})_4(\text{OMc})_{16}$ showed a starting high catalytic activity for the oxidation of benzylic alcohol and the epoxidation of cyclooctene, its

hydrolysis prevented the formation of the products with an effective conversion. The degradation of the cluster was demonstrated both in homogeneous and in heterogeneous conditions. In particular, for the latter case, the degradation of the cluster was due to physical incorporation, and not due to a covalent attachment. Therefore, although **Ti₉** showed interesting catalytic properties, it did not act simultaneously as a cross-linker unit for the hydrophilic polymer matrix of PNAGA, PNMGA and PNIPAM nanoparticles.

Photopolymerization is presented as a convenient alternative to thermal initiation in **Section 4.3**. The synthesis of hybrid poly(MMA-*co*-**Zr₄**) nanoparticles by using photo-induced miniemulsion copolymerization is reported. The use of commercial benzoin-type photoinitiators allowed an efficient incorporation of the inorganic guest into the resulting polymer matrix. Cross-linking efficiency, thermal properties, and morphology are comparable to the hybrid nanoparticles synthesized in **Section 4.1** using thermal-induced copolymerization.

In **Section 4.4** the focus is directed to the encapsulation of an organic dye (Nile red) in thermo-responsive hybrid nanoparticles for the development of a “nano-thermometer” system. Also in this case, **Zr₄** is acting as a cross-linker unit when copolymerized with amphiphilic monomers. The LSCT of poly(NIPAM-*co*-**Zr₄**) nanocapsules is dependent on the oxocluster content, and the fluorescence intensity of enclosed Nile red is dependent on the temperature. The observed “on-off” switching of fluorescence intensity by alternating the nanocapsules dispersion temperature could be successfully applied as Galileo-like “nano-thermometer”. Further experiments in this direction will be made by using confocal laser scanning microscopy.

In summary, this thesis provided insight about the development of class II hybrid materials in a colloidal state. The miniemulsion technique has been demonstrated to be a promising toolbox for the synthesis of metal oxocluster/polymer hybrid materials. We have shown that different applications can be aimed by changing the nature and the composition of the starting building blocks. An extended range of possible applications can be investigated, which will provide further insights about the understanding, development, and optimization of class II hybrid materials.

6. Experimental Part

6.1. Experimental Details for Section 4.1

6.1.1. Materials

Zirconium *n*-butoxide ($\text{Zr}(\text{O}i\text{Bu})_4$, Alfa Aesar, 80% w/w in 1-butanol), methacrylic acid (Sigma-Aldrich, 99% stabilized), 2,2'-azobis(2-methylbutyronitrile) (V59, Wako, $\geq 98.0\%$), hexadecane (Sigma-Aldrich, 99%), sodium *n*-dodecyl sulfate (SDS, Alfa Aesar, 99% powder ultrapure), and Lutensol AT50 (a poly(ethylene oxide)-hexadecyl ether with an EO block length of about 50 units, BASF SE, powder) were used as received without further purification. Methyl methacrylate (Acros Organics, 99% stabilized) was filtered on neutral alumina to remove the inhibitor. Deionized water was used in all experiments.

6.1.2. Synthesis of $\text{Zr}_4\text{O}_2[\text{O}(\text{O})\text{CC}(\text{CH}_3)=\text{CH}_2]_{12}$ (Zr_4)

The zirconium oxocluster was synthesized according to reported procedures^{47, 241} by reaction of zirconium butoxide with methacrylic acid in a 1:7 molar ratio (Figure 4.2a). After mixing the precursors at room temperature without any stirring, the solution was allowed to stand for 2 days under argon atmosphere. The cubic colorless crystals formed were decanted and dried under vacuum for 2 h (80% yield). The crystalline structure of the oxocluster, previously reported in the literature,⁴⁷ was confirmed by measuring the unit cell dimensions on a number of different single crystals by X-ray diffraction technique [monocline, $a = 10.540(2)$ Å, $b = 20.042(2)$ Å, $c = 14.311(2)$ Å, $\beta = 103.27(1)^\circ$]. FTIR (KBr, cm^{-1}): $\tilde{\nu} = 3245$ (weak, broad); 3098 (weak, =C-H); 2978 (weak, asymmetric stretching CH_3), 2958 (weak, CH); 2927 (weak, CH); 1647 (medium, C=C); 1575 (strong, broad, asymmetric stretching COO^-); 1500 (medium, COO^-); 1460 (strong, symmetric, COO^-); 1423 (strong, symmetric, COO^-); 1372 (medium, bending CH_3); 1246 (strong, bending CH_3); 1007 (strong, bending CH_3); 942 (medium, bending out of the plane $\text{CH}(\text{C}=\text{CH}_2)$); 879 (medium); 825 (medium, broad CH_3); 663 (medium broad); 617 (m, b OCO); 554 (medium); 512 (medium).

6.1.3. Preparation of Cross-Linked Hybrid Poly(MMA-co-Zr₄) Nanoparticles

Cross-linked hybrid poly(MMA-co-Zr₄) nanoparticles with different Zr₄ weight percentages were synthesized by thermally activated free radical polymerization in direct miniemulsion. The oil phase, consisting of the combination of MMA and Zr₄ as monomers (6 g in total, weight ratios reported in Table 4.1), hexadecane (250 mg) as a hydrophobic agent, and the initiator 2,2'-azobis(2-methyl-butyronitrile) (V-59, 100 mg), was stirred at 1000 rpm for 30 min to dissolve the oxocluster crystals. Subsequently, the oil phase was mixed with 24 g of an aqueous surfactant solution containing either SDS (3.0 g·L⁻¹) or the nonionic surfactant Lutensol AT50 (20.8 g·L⁻¹). The resulting mixture was pre-emulsified by stirring at 1000 rpm for 20 min and then homogenized by ultrasonication (2 min, 90% intensity, Branson Sonifier W450 Digital, 0.5 in. tip) while cooling at 0 °C with an ice-water bath. The polymerization was carried out for 16–18 h at 72 °C under stirring under inert argon atmosphere (Figure 4.2b). After the polymerization, coagulates were removed by filtration with filter paper. The particles dispersions were finally freeze-dried to remove the unreacted monomer. To remove the surfactant in excess, freeze-dried nanoparticles were redispersed in water using a vortex and centrifuged at 4000 rpm for 20 min at room temperature. After the washing procedure was repeated four times, the particles were freeze-dried again, and characterized by XAS, and solid-state NMR spectroscopy. An additional washing step, followed by centrifugation was performed, either using THF as a solvent for samples characterized by GPC or acetonitrile for particles used in the catalytic experiments. In GPC measurements, after the centrifugation step, the supernatant (soluble fraction) was taken for the measurement, while for the catalytic experiments, the cross-linked fraction was used upon drying. The remaining SDS amount was evaluated following the protocol suggested by Rusconi *et al.*¹⁴⁶. FTIR (KBr, cm⁻¹): $\tilde{\nu}$ = 3449 (broad); 2993 (medium, symmetric CH); 2952 (medium, CH); 2929 (medium, CH); 2853 (weak, CH); 1735 (strong, symmetric COOMe); 1630 (weak, C=C); 1453 (medium, bending CH₃); 1270 (medium); 1244 (medium); 1194 (medium); 1148 (medium, bending CO); 1063 (medium); 990 (medium); 966 (medium); 840 (weak); 809 (medium); 752 (medium).

6.1.4. Catalytic Experiments

In a typical oxidation reaction, poly(MMA-*co*-**Zr₄**) nanoparticles (in the form of dried solid) were added to 2.4 mL of acetonitrile in a small closed vial, in order to provide 1.0 μmol of **Zr₄**. Then methyl *p*-tolyl sulfide, benzyl alcohol or cyclooctene (1.0 mmol) and H₂O₂ (2.46 mmol, from a 30% aqueous solution) were added. The oxidation reaction was run at fixed temperature (50 °C) under stirring. Samples (50 or 10 μL) were withdrawn at fixed time intervals, diluted in 500 μL of a 5 mM solution of *n*-undecane (standard) in acetonitrile and treated with triphenylphosphine (supported on a poly(styrene/divinylbenzene) resin) as oxidant quencher. GC analyses were performed with a SHIMADZU GC2010 equipped with an ionization flame detector and an EQUITY-5 (15 m \times 0.1 mm) capillary column of poly (5% diphenyl/95% dimethylsiloxane) with 0.1 mm film thickness. ($T_{\text{injection}} = 270$ °C; $T_{\text{detection}} = 280$ °C; carrier gas: He; $T_{\text{initial}} = 90$ °C \times 1 min; rate = 90 °C \cdot min⁻¹; $T_{\text{final}} = 260$ °C \times 5 min). Retention times: *n*-undecane: 1.9 min; methyl *p*-tolyl sulfide: 2.3 min; methyl *p*-tolyl sulfoxide: 2.8 min; methyl *p*-tolyl sulfone: 3.0 min; benzyl alcohol: 3.3 min; benzaldehyde: 3.0 min; benzoic acid: 3.8 min; cyclooctene: 2.8 min; cyclooctene oxide: 3.6 min. Concentrations (*M*) of methyl *p*-tolyl sulfide and its oxidation products were calculated by integration of chromatographic peaks (*A*) of the standard (*S*) and of the analytes (*X*), using the following calculated response factors $F = (A_S/M_S)/(A_X/M_X)$: $F(\text{undecane})=1$, $F(\text{methyl } p\text{-tolyl sulfide})=0.58$, $F(\text{methyl } p\text{-tolyl sulfoxide})=0.48$, $F(\text{methyl } p\text{-tolyl sulfone})=0.57$, $F(\text{benzyl alcohol})=5.23$, $F(\text{benzaldehyde})=2.73$, $F(\text{benzoic acid})=17.53$, $F(\text{cyclooctene})=1.73$, $F(\text{cyclooctene oxide})=1.54$.

In case of the oxidation of methyl *p*-tolyl sulfide: second global order kinetic constants k_1 and k_1 were determined performing a fitting on the experimental values with SCIENTIST MICROMATH[®] software, using the kinetic scheme S1.

Hybrid nanoparticles stabilities were assessed by comparison of FTIR spectra before and after the reaction (upon precipitation and washing with isopropanol). Recycling experiments were performed after a first reaction (24 h), upon recovery of the hybrid nanoparticles by high speed centrifugation and washing with acetonitrile. Independent reactions with 2 equivalents of H₂O₂ have shown a H₂O₂ utilization efficiency >75%.

6.2. Experimental Details for Section 4.2

6.2.1. Materials

Titanium propoxide ($\text{Ti}(\text{OPr})_4$, Sigma Aldrich, 98%), methacrylic acid (Sigma-Aldrich, 99% stabilized), 2,2'-azobis(2-methylbutyronitrile) (V59, Wako, $\geq 98.0\%$), methyl glycolate (Sigma-Aldrich, 98%), and N-Isopropylacrylamide (NIPAM, Sigma Aldrich, 97%) were used as received without further purification. Deionized water was used in all experiments.

6.2.2. Synthesis of Amphiphilic Block Copolymer Poly(ethylene/butylene)-*b*-Poly(ethylene oxide) (P(E/B)-*b*-PEO) Copolymer

The synthesis of the P(E/B)-*b*-PEO copolymer followed the recipe described elsewhere.²⁴² The starting P(E/B) block was a commercial copolymer (Kraton Liquid L-1203) of molecular weight $3700 \text{ g}\cdot\text{mol}^{-1}$, to which ethylene oxide was copolymerized by anionic polymerization. The molecular weights of the block copolymer P(E/B)-*b*-PEO used in this work was estimated to be $6700 \text{ g}\cdot\text{mol}^{-1}$ by $^1\text{H-NMR}$, taking into account the known molecular weight of the P(E/B) block.

6.2.3. Synthesis of *N*-Acryloyl Glycinamide (NAGA)

N-Acryloyl glycinamide was synthesized according to reported procedure¹⁶⁴. A solution of glycinamide hydrochloride (15 g in 100 mL of dry diethyl ether) was mixed with a solution of potassium carbonate in water (6.9 M). The solution was cooled to $0 \text{ }^\circ\text{C}$ and acryloyl chloride (stoichiometric ratio 1:1 between glycinamide hydrochloride and acryloyl chloride) was added dropwise under stirring. Stirring was continued for 1 h at $0 \text{ }^\circ\text{C}$, the aqueous phase separated and evaporated to dryness under vacuum at $35 \text{ }^\circ\text{C}$. The solid residue was extracted with acetone and concentrated. The monomer was purified with a chromatography column and crystallized in acetone.

6.2.4. Synthesis of *N*-Methacryloyl Glycinamide (NMGA)

The preparation of *N*-methacryloyl glycinamide is analogous to *N*-acryloyl glycinamide with the only difference that methacryloyl chloride was used instead of acryloyl chloride.

6.2.5. Synthesis of $\text{Ti}_9\text{O}_8(\text{OPr})_4(\text{OMc})_{16}$ (Ti_9)

The titanium oxocluster was synthesized according to reported procedures by reaction of titanium *n*-propoxide with methacrylic acid in a 1:4 molar ratio.⁵⁹ After mixing at room temperature, the solution was allowed to stand for circa 1 month under argon atmosphere at 8 °C. The formed yellow crystals were separated from an amorphous orange powder, decanted and dried under vacuum for 2 h and washed afterwards with acetone. FTIR (KBr, cm^{-1}): $\tilde{\nu}$ = 3449 (broad); 2993 (medium, symmetric CH); 2952 (medium, CH); 2929 (medium, CH); 2853 (weak, CH); 1735 (strong, symmetric COOMe); 1630 (weak, C=C); 1453 (medium, bending CH_3); 1270 (medium); 1244 (medium); 1194 (medium); 1148 (medium, bending CO); 1063 (medium); 990 (medium); 966 (medium); 840 (weak); 809 (medium); 752 (medium).

6.2.6. Preparation of Hybrid Poly(PNIPAM-*co*- Ti_9) Nanoparticles

Cross-linked hybrid poly(PNIPAM-*co*- Ti_9) nanoparticles with 10 wt% of Ti_9 were synthesized by thermally activated free radical polymerization in inverse miniemulsion. The hydrophilic phase, consisting of the combination of NIPAM and Ti_9 as monomers (450 mg in total), methyl glycolate (467 μL), and water (45 μL) as a hydrophilic agent, was stirred at 1000 rpm for 30 min to dissolve the oxocluster crystals. Subsequently, the hydrophilic phase was mixed with 8 mL of the surfactant solution in cyclohexane containing the amphiphilic block copolymer P(E/B)-*b*-PEO (0.6 wt%). The resulting mixture was pre-emulsified by stirring at 1000 rpm for 20 min and then homogenized by ultrasonication (2 min, 90% intensity, Branson Sonifier W450 Digital, 0.5 in. tip) while cooling at 0 °C with an ice-water bath. The initiator 2,2'-azobis(2-methyl-butyronitrile) (V-59, 50 mg) was added to the formed emulsion. The polymerization was carried out for 16–18 h at 72 °C under stirring under inert argon atmosphere. The particles dispersions were finally freeze-dried to remove the unreacted monomer and used in the catalytic experiments. An additional washing step, followed by centrifugation was performed, using THF as a solvent for samples characterized by GPC. For the latter measurements, after the centrifugation step, the supernatant (soluble fraction) was separated and used for the measurement.

6.2.7. Preparation of Hybrid Poly(NAGA-co-Ti₉) and Hybrid Poly(NMGA-co-Ti₉) Nanoparticles

The preparation of hybrid poly(NAGA-co-Ti₉) and hybrid poly(NMGA-co-Ti₉) nanoparticles is analogous to hybrid poly(PNIPAM-co-Ti₉) nanoparticles with the only difference that NAGA and NMGA were used instead of PNIPAM as monomers, respectively.

6.2.8. Catalytic Experiments

In a typical oxidation reaction, poly(NIPAM-co-Ti₉) and poly(NMGA-co-Ti₉) nanoparticles (in the form of dried solid) were added to 2.4 mL of acetonitrile in a small closed vial, in order to provide 1.0 μmol of Ti₉. Then benzyl alcohol or cyclooctene (1.0 mmol) and H₂O₂ (2.46 mmol, from a 30% v/v aqueous solution) were added. The oxidation reaction was run at fixed temperature (50 °C) under stirring. Samples (50 or 10 μL) were withdrawn at fixed time intervals, diluted in 500 μL of a 5 mM solution of *n*-undecane (standard) in acetonitrile and treated with triphenylphosphine (supported on a poly(styrene/divinylbenzene) resin) as oxidant quencher. GC analyses were performed with a gas chromatograph coupled with mass spectrometer (Shimadzu, GCMS-QP2010 Ultra) and Phenomenex, Zebron 5-ms (unpolar) fused silica capillary column of 100% dimethyl polysiloxane. ($T_{\text{injection}} = 310\text{ °C}$; $T_{\text{detection}} = 250\text{ °C}$; carrier gas: He; $T_{\text{initial}} = 50\text{ °C}$; rate = $52\text{ °C}\cdot\text{min}^{-1}$; $T_{\text{final}} = 310\text{ °C}$). Retention times: *n*-undecane: 3.5 min; benzyl alcohol: 3.3 min; benzaldehyde: 3.0 min; benzoic acid: 3.8 min; cyclooctene: 2.8 min; cyclooctene oxide: 3.6 min. Concentrations (M) of the reagents and the oxidation products were calculated by integration of chromatographic peaks (A) of the standard (S) and of the analytes (X), using the following calculated response factors $F = (A_S/M_S)/(A_X/M_X)$: $F(n\text{-undecane}) = 1$, $F(\text{benzyl alcohol}) = 5.23$, $F(\text{benzaldehyde}) = 2.73$, $F(\text{benzoic acid}) = 17.53$, $F(\text{cyclooctene}) = 1.73$, $F(\text{cyclooctene oxide}) = 1.54$.

6.3. Experimental Details for Section 4.3

6.3.1. Materials

Zirconium *n*-butoxide (Alfa Aesar, 80% w/w in 1-butanol), methacrylic acid (Sigma-Aldrich, 99% stabilized), 2-hydroxy-1-[4-(2-hydroxyethoxy)phenyl]-2-methyl-1-

propanone (commercially known as Irgacure 2959, BASF SE), a commercial mixture of oxy-phenyl-acetic acid 2-[2-oxo-2 phenyl-acetoxy-ethoxy]-ethyl ester and oxy-phenyl-acetic 2-[2-hydroxy-ethoxy]-ethyl ester (Irgacure 754, BASF SE), 2-benzyl-2-(dimethylamino)-1-[4-(4-morpholinyl) phenyl]-1-butanone (Irgacure 369, BASF SE), 2,2'-azobis(2-methylbutyronitrile) (AMBN, Wako, $\geq 98.0\%$), hexadecane (Sigma-Aldrich, 99%), sodium *n*-dodecyl sulfate (SDS, Alfa Aesar, 99% powder ultrapure), Lutensol AT50 (a poly(ethylene oxide)-hexadecyl ether with an EO block length of about 50 units, BASF SE, powder), and tetrahydrofuran (THF) were used as received without further purification. Methyl methacrylate (MMA, Acros Organics, 99% stabilized) was passed through a column of neutral alumina to remove the inhibitor. Deionized water was used in all experiments. To shift the bending ν_2 , which was interfering with the FTIR-ATR experiments, deuterated water (Sigma-Aldrich, 99.9 atom % D) was used in the kinetic studies.

6.3.2. Synthesis of $Zr_4O_2[O(O)CC(CH_3)=CH_2]_{12} (Zr_4)^{vii}$

6.3.3. Preparation of Cross-Linked Hybrid Poly(MMA-*co*- Zr_4) Nanoparticles by Thermally Activated Free Radical Polymerization

Cross-linked hybrid poly(MMA-*co*- Zr_4) nanoparticles with different Zr_4 weight percentages were synthesized by direct miniemulsion polymerization. The oil phase, consisting of the mixture of MMA and Zr_4 as monomers (0.55 g in total, weight ratios reported in Table 4.10), hexadecane (22.8 mg) as a hydrophobic agent, and the initiator AMBN (9.2 mg), was stirred at 1000 rpm for 30 min to dissolve the oxocluster crystals. Subsequently, the oil phase was mixed with 2.2 g of an aqueous solution of SDS ($3.0 \text{ g}\cdot\text{L}^{-1}$). The resulting mixture was pre-emulsified by stirring at 1000 rpm for 20 min and then homogenized by ultrasonication (3 min, 70% intensity, Branson Sonifier W450 Digital, 0.125 in tip) while cooling with an ice-water bath. The free radical polymerization was carried out for 18 h at 72 °C under stirring in an inert argon atmosphere. After polymerization, any formed coagulum was removed by filtration with filter paper. To remove the surfactant in excess, the nanoparticles were dialyzed in water (MWCO: 14000).

^{vii} As reported in Section 6.1.2.

6.3.4. Preparation of Cross-Linked Hybrid Poly(MMA-co-Zr₄) Nanoparticles by Photoactivated Free Radical Polymerization

The preparation of the nanoparticles is analogous to the thermally activated hybrid poly(MMA-co-Zr₄),⁵¹ however the Irgacure initiators were added (16.5 mg), instead of an azo-initiator. The polymerization was carried out directly in a quartz cuvette (Hellma Analytics, material code: QS, light path: 10 mm and volume: 3500 μL) for 4 h under irradiation with a UV Mercury HBO100 lamp (100 W), under continuous stirring and an inert argon atmosphere. Furthermore, to cut the unnecessary wavebands during the irradiation, a UG11 UV-band pass filter was adopted because its band pass is in the range 250–400 nm. Particular attention was paid to the UV irradiation setup, and the distance between the lamp and the sample was set as 15 cm, which was found to be optimum in terms of nanoparticles size distribution, polydispersity, and solid content.

6.3.5. Kinetic FTIR Investigation of the Polymerization Process of the Cross-Linked Hybrid Poly(MMA-co-Zr₄) Nanoparticles

To investigate the monomer conversion, aliquots at different polymerization times were analyzed by using an FTIR spectrophotometer (Perkin-Elmer, Paragon 1000) with a horizontal ATR in the spectral range 1800–1600 cm⁻¹. The degree of conversion of carbon C=C double bonds of the methacrylate groups, present both in the monomer and on the oxocluster, to single C–C bonds upon photopolymerization, was calculated based on the ratio between the absorbance of the aliphatic C=C peak at 1638 cm⁻¹ (A_{1638}), consumed upon polymerization and the absorbance of C=O peak at 1720 cm⁻¹ (A_{1720}), which instead remain unaffected. The degree of the monomer conversion (C) was calculated according to the following equation:^{76, 179}

$$C = \left[1 - \frac{\left(\frac{A_{1638}}{A_{1720}}\right)_{\text{polymer}}}{\left(\frac{A_{1638}}{A_{1720}}\right)_{\text{monomer}}} \right] \cdot 100$$

6.4. Experimental Details for Section 4.4

6.4.1. Materials

Zirconium *n*-butoxide ($\text{Zr}(\text{O}i\text{Bu})_4$, Alfa Aesar, 80% w/w in 1-butanol), methacrylic acid (Sigma-Aldrich, 99% stabilized), 2,2'-azobis(2-methylbutyronitrile) (V59, Wako, $\geq 98.0\%$), hexadecane (Sigma-Aldrich, 99%), sodium *n*-dodecyl sulfate (SDS, Alfa Aesar, 99% powder ultrapure), Nile red (9-diethylamino-5-benzo- α -phenoxazinone, Sigma-Aldrich), toluene (Sigma-Aldrich, 99.8%), *N*-isopropylacrylamide (Sigma-Aldrich, 97%), *N*-isopropylmethacrylamide (Sigma-Aldrich, 97%), poly(*N*-isopropylacrylamide) (Sigma-Aldrich, M_n : 20,000-40,000 $\text{g}\cdot\text{mol}^{-1}$), dimethylformamide (DMF, Sigma-Aldrich, anhydrous 99.8%) were used as received without further purification. For the preparation of samples for transmission electron microscopy analysis, the samples were embedded in a D-(+)-trehalose dihydrate matrix (Fisher BioReagents), using uranyl acetate dihydrate (Riedel de Haën) as negative staining. Deionized water was used in all experiments.

6.4.2. Synthesis of $\text{Zr}_4\text{O}_2[\text{O}(\text{O})\text{CC}(\text{CH}_3)=\text{CH}_2]_{12}$ (Zr_4)^{viii}

6.4.3. Preparation of Cross-Linked PNIPAM and PNIPMM Nanocapsules

Cross-linked nanocapsules with different cross-linkers were synthesized by thermally activated free radical polymerization in direct miniemulsion. A mixture consisting either of NIPAM or NIPMM combined with Zr_4 as a cross-linkers (1 g in total, weight ratios reported in Table 4.11), hexadecane (163 μL) as a hydrophobic agent, and the initiator 2,2'-azobis(2-methyl-butyronitrile) (AMBN, 50 mg) were dissolved in a solution of NR in toluene (2.3 mL, 1.3 mM). The formed oil phase was stirred at 1000 rpm for 20 min until a clear solution was obtained; subsequently, it was mixed with 12 g of an aqueous surfactant solution containing SDS (3.0 $\text{g}\cdot\text{L}^{-1}$). The resulting mixture was pre-emulsified by stirring at 1000 rpm for 20 min and then homogenized by ultrasonication (2 min, 90% intensity, Branson Sonifier W450 Digital, 0.5 in. tip) while cooling with an ice-water bath. The polymerization was carried out for 16–18 h at 72 °C under stirring under inert argon atmosphere. After the polymerization, coagulates were removed by filtration with Kimtech Science Kimwipes paper. To remove the non-encapsulated dye, surfactant in

^{viii} As reported in Section 6.1.2.

excess and small oligomers, the remaining nanocapsules suspension (~10 mL) was dialyzed in 2 L of water for 3 days by using cellulose dialysis membranes (Roth, MWCO 14000). To ensure an efficient dialysis, the water was changed every 12 hours. The nanocapsules dispersions were finally freeze-dried to remove the remaining liquid continuous phase (unreacted monomer and toluene) and redispersed in water. Nanocapsules dispersion were characterized by mean of dynamic light scattering (DLS) and transmission electron microscopy (TEM), both after dialysis and after re-dispersion in water. Fluorescence measurements and elemental analysis characterization by inductively coupled plasma optical emission spectrometry (ICP-OES) were performed on redispersed nanocapsules dispersions. For samples characterized by gel permeation chromatography (GPC), dry nanocapsules were first dissolved in DMF and centrifuged. After the centrifugation step, the supernatant (soluble fraction) was taken for the measurement.

6.5. Characterization Techniques

6.5.1. Gel Permeation Chromatography (GPC)

For gel permeation chromatography (GPC) measurements, freeze-dried samples were first dissolved in THF, and then centrifugation was performed to remove the nanoparticles cross-linked fraction. The supernatant (soluble fraction) was taken for the measurement (concentration around $1 \text{ g}\cdot\text{L}^{-1}$).

For hydrophobic latexes, the experiments were performed using an Agilent Technologies 1260 instrument consisting of a pump, an autosampler, and a column oven. The column set consisting of 3 columns (SDV 10^6 \AA , SDV 10^4 \AA , and SDV 500 \AA ; PSS Standards Service GmbH, Mainz, Germany), all of $300 \times 8 \text{ mm}$ and an average particle size of $10 \text{ }\mu\text{m}$, were used at a flow rate of $1.0 \text{ mL}\cdot\text{min}^{-1}$ and a column temperature of $30 \text{ }^\circ\text{C}$. The injection volume was $100 \text{ }\mu\text{L}$. The detection was accomplished with a refractive index detector (Agilent Technologies). The data acquisition and the evaluation was conducted by using PSS WINGPC UniChrom (PSS Polymer Standards Service). The calibration was carried out by using poly(methyl methacrylate) (PSS Polymer Standards Service).

For hydrophilic and amphiphilic latexes, the experiments were performed using a PSS SECcurity instrument consisting of a pump, autosampler and column oven. As eluent

DMF with $1 \text{ g}\cdot\text{L}^{-1}$ LiBr was used. A column set consisting of 3 columns: GRAM 10000 Å, GRAM 1000 Å and GRAM 100Å (PSS Standards Service GmbH, Mainz, Germany), all of 300 x 8 mm and 10µm average particle size was used at a flow rate of $1.0 \text{ mL}\cdot\text{min}^{-1}$ and a column temperature of 60 °C. The injection volume was 100 µL. Detection was accomplished with a RI detector (Agilent Technologies 1260 Infinity). Data acquisition and evaluation was performed using PSS WINGPC UniChrom (PSS Polymer Standards Service GmbH, Mainz, Germany). Calibration was carried out by using polystyrene provided by PSS Polymer Standards Service GmbH (Mainz, Germany).

6.5.2. Inductively Coupled Plasma Optical Emission Spectrometry (ICP-OES)

The contents of the Zr_4 in the hybrid nanoparticles matrix were determined by inductively coupled plasma optical emission spectrometry (ICP-OES) using an ACTIVA M spectrometer (Horiba Jobin Yvon, Bernsheim, Germany) equipped with a Meinhardt-type nebulizer, a cyclone chamber, and controlled by ACTIVAnalyst 5.4 software. The following conditions were applied unless stated otherwise: 1 250 W forward plasma power, $12 \text{ L}\cdot\text{min}^{-1}$ Ar flow and 15 rpm pump flow. The colloidal dispersions were diluted with water to 0.1 wt.% and sonicated for 3 min prior to measuring. The argon emission line at 404.442 nm was used as reference line. Measurements were performed using four different standard concentrations, at least three different elemental emission lines and 5 s integration time. As baseline correction, a dynamic underground correction provided by the software was used. The measurement for each sample was repeated three times.

6.5.3. Scanning Electron Microscopy (SEM)

Scanning electron microscopy (SEM) analysis was carried out by using a Leo Gemini 1530 field-emission microscope operated at a voltage of 0.7 kV. Samples for SEM observation were prepared by drop-casting of diluted dispersions on silicon wafers.

6.5.4. Transmission Electron Microscopy (TEM)

Transmission electron microscopy (TEM) and scanning TEM (STEM) combined with energy-dispersive X-ray spectroscopy (EDX) were carried out in FEI Tecnai F20

microscope operated at 200 kV. The electron micrographs were recorded on a 2k CCD (charge-coupled device) camera (Gatan Ultrascan 1000). The Digital Micrograph software (Gatan) was used to collect the images.

For the measurement, the particles were dispersed in an epoxy resin and 60 nm sheets were cut out for the measurement with a Leica EM UC7 Cryo-Ultramicrotome at room temperature. In contrast for the nanocapsules, 2 μL of dispersions was placed on a lacey grid and let to air dry. Afterwards, the samples were prepared by embedding the material in a matrix of trehalose, containing 4% uranyl acetate as negative staining to increase the contrast.²⁴³

6.5.5. X-ray Absorption Spectroscopy (XAS)

X-Ray absorption spectroscopy (XAS) analysis at the Zr K-edge (17998 eV) spectra were recorded at the bending magnet 08 (GILDA) beamline at European Synchrotron Radiation Facility (ESRF), under 16-bunches operating conditions (6 GeV, 90 mA). The freeze-dried samples were finely ground, homogenized with cellulose as dispersant and pressed into pellets. For energy selection, a Si(311) double-crystal monochromator was used. Spectra were collected in the partially detuned configuration of the monochromator. Data were collected in transmission mode using two ionization chambers placed upstream and downstream of the sample or, for diluted hybrid sample, in fluorescence mode, using a 13-element Ge solid state detector. Internal energy calibration was accomplished by simultaneous measurement of the absorption of an appropriate metallic foil placed between two ionization chambers situated after the sample. Data reduction and analysis was performed using the Demeter packages; in particular, background removal was performed by the Autobk routine of the Athena software, which was also used for data alignment and calibration. The extracted EXAFS functions were fitted exploiting the software Artemis. The values of S_0^2 were evaluated by fitting the corresponding bulk standard (Zr foil). Coordination numbers, distances and Debye-Waller factors were set free to vary.

6.5.6. Dynamic Light Scattering (DLS)

Particles sizes were determined by dynamic light scattering (DLS) using a Nicomp particle sizer (model 380, PSS, Santa Barbara, CA) at a fixed angle of 90°.

Nanoparticles and nanocapsules sizes as a function of temperature were determined by dynamic light scattering (DLS) in water by using an ALV spectrometer consisting of a goniometer and an ALV-5004 multiple-tau full-digital correlator (320 channels), which allows measurements over an angular range from 30 to 150°. A He-Ne Laser (wavelength of 632.8 nm) is used as light source. For temperature-controlled measurements, the light scattering instrument was equipped with a thermostat (Julabo).

6.5.7. Differential Scanning Calorimetry (DSC)

Differential scanning calorimetry (DSC) was carried out by using Mettler Toledo DSC 823 in a temperature range between -50 °C and +350 °C with a heating/cooling rate of 10 °C min⁻¹.

6.5.8. Nuclear Magnetic Resonance (NMR)

Solid state ¹³C CP-MAS NMR measurements were performed on a Bruker Avance II spectrometer operating at 300.13 MHz ¹H Larmor frequency using a commercial 4 mm double resonance MAS NMR probe at ambient conditions and 10 kHz MAS spinning frequency. The rf nutation frequency was on both channels, ¹H and ¹³C, adjusted to 62.5 kHz corresponding to a 90° pulse of 4 μs, in order to fulfill the Hartmann-Hahn matching condition required for CP-MAS experiments. High power composite pulse decoupling (SPINAL64) during signal acquisition. Depending on the sample amount available, 20,000–70,000 transients with a relaxation time of 3s were recorded in order to achieve an appropriate signal to noise ratio in order to analyze the weak ¹³C NMR signals of **Zr₄** ligands.

¹H NMR spectra were recorded using a Bruker Avance III 850. All spectra were referenced internally to residual proton signals of the deuterated solvent.

6.5.9. X-Ray Photoelectron Spectroscopy (XPS)

X-Ray Photoelectron Spectroscopy (XPS) was carried out on a Perkin-Elmer Φ 5600ci spectrometer using standard Al radiation (1486.6 eV) working at 250 W. The working pressure was < 5 · 10⁻⁸ Pa. The spectrometer was calibrated by assuming the binding energy (BE) of the Au4f_{7/2} line at 83.9 eV with respect to the Fermi level. The standard deviation for the BE values was 0.15 eV. The reported BE were corrected for the charging effects, assigning, in the outer layers where contamination carbon is still

present, to the C1s line of carbon the BE value of 284.6 eV.²⁴⁴⁻²⁴⁵ Survey scans (187.85 pass energy, 0.4 eV/step, 25 ms per step) were obtained in the 0–1350 eV range. Detailed scans (29.35 eV pass energy, 0.1 eV/step, 100–150 ms per step) were recorded for the C1s, O1s, Zr3p and Zr3d regions. The atomic composition, after a Shirley type background subtraction²⁴⁶ was evaluated using atomic sensitivity factors supplied by Perkin-Elmer.²⁴⁵ The assignments of the peaks were carried out by using the values reported in the reference handbook,²⁴⁵ in the NIST XPS Database.²⁴⁷ For a detailed XPS data evaluation analysis, the core-level lines obtained by XPS they were fitted by the freeware program XPS Peak 41 by subtracting a Shirley background and by using Gaussian-Lorentzian contributions. During the fitting procedure, all the parameters were left freely process. Elemental analyses were carried out by using the program MultiPak (Ulvac-Phi, Version 9.4), by using the corresponding photoionisation cross-sections.²⁴⁵

6.5.10. Fluorescence Measurements

Fluorescence intensity measurements were performed with the Infinite M1000 plate reader from Tecan, Austria using 96-well plates.

6.5.11. FTIR Measurements

Fourier transform infrared spectroscopy (FTIR) was performed with a Spectrum BX spectrometer (PerkinElmer Inc., USA). The absorption of KBr pellets of the samples was measured between 4000 and 400 cm^{-1} .

7. References

1. Kickelbick, G., Hybrid Materials – Past, Present and Future. *Hybrid Materials* **2014**, *1*, 39-51.
2. Currie, H. A.; Patwardhan, S. V.; Perry, C. C.; Roach, P.; Shirtcliffe, N. J., Natural and artificial hybrid biomaterials. *Hybrid materials—synthesis, characterization and applications*. Wiley, Weinheim **2007**, 138.
3. Ahmad, Z.; Mark, J. E., Biomimetic materials: recent developments in organic-inorganic hybrids. *Mat. Sci. Eng. C* **1998**, *6* (2), 183-196.
4. Young, C. S.; Abukawa, H.; Asrican, R.; Ravens, M.; Troulis, M. J.; Kaban, L. B.; Vacanti, J. P.; Yelick, P. C., Tissue-Engineered Hybrid Tooth and Bone. *Tissue Eng.* **2005**, *11*, 1599-1610.
5. Lewandowska-Lańcucka, J.; Fiejdasz, S.; Rodzik, Ł.; Łatkiewicz, A.; Nowakowska, M., Novel hybrid materials for preparation of bone tissue engineering scaffolds. *J. Mater. Sci. Mater. Med.* **2015**, *26* (9), 231.
6. Kato, T.; Sugawara, A.; Hosoda, N., Calcium Carbonate–Organic Hybrid Materials. *Adv. Mater.* **2002**, *14* (12), 869-877.
7. Gómez-Romero, P.; Sanchez, C., Hybrid Materials, Functional Applications. An Introduction. In *Functional Hybrid Materials*, Wiley-VCH Verlag GmbH & Co. KGaA: **2005**, pp 1-14.
8. Ruiz-Hitzky, E., Organic-Inorganic Materials: From Intercalation Chemistry to Devices. In *Functional Hybrid Materials*, Wiley-VCH Verlag GmbH & Co. KGaA: **2005**, pp 15-49.
9. Kickelbick, G., Introduction to Hybrid Materials. In *Hybrid Materials*, Wiley-VCH: **2007**, pp 1-48.
10. Nicole, L.; Laberty-Robert, C.; Rozes, L.; Sanchez, C., Hybrid materials science: a promised land for the integrative design of multifunctional materials. *Nanoscale* **2014**, *6* (12), 6267-92.
11. Karg, M.; Hellweg, T., Smart inorganic/organic hybrid microgels: Synthesis and characterisation. *J. Mater. Chem.* **2009**, *19* (46), 8714-8727.
12. Sanchez, C.; Lebeau, B.; Chaput, F.; Boilot, J. P., Optical Properties of Functional Hybrid Organic–Inorganic Nanocomposites. *Adv. Mater.* **2003**, *15* (23), 1969-1994.
13. Sanchez, C.; Julian, B.; Belleville, P.; Popall, M., Applications of hybrid organic-inorganic nanocomposites. *J. Mater. Chem.* **2005**, *15* (35-36), 3559-3592.

14. Chiari, G.; Giustetto, R.; Druzik, J.; Doehne, E.; Ricchiardi, G., Pre-columbian nanotechnology: reconciling the mysteries of the maya blue pigment. *Appl. Phys. A* **2008**, *90* (1), 3-7.
15. Kogler, F. R.; Schubert, U., Crosslinking vs. filler effect of carboxylate-substituted zirconium oxo clusters on the thermal stability of polystyrene. *Polymer* **2007**, *48* (17), 4990-4995.
16. Kickelbick, G., Concepts for the incorporation of inorganic building blocks into organic polymers on a nanoscale. *Prog. Polym. Sci.* **2003**, *28* (1), 83-114.
17. Pyun, J.; Matyjaszewski, K., The Synthesis of Hybrid Polymers Using Atom Transfer Radical Polymerization: Homopolymers and Block Copolymers from Polyhedral Oligomeric Silsesquioxane Monomers. *Macromolecules* **2000**, *33* (1), 217-220.
18. Markovic, E.; Constantopolous, K.; Matison, J., Polyhedral Oligomeric Silsesquioxanes: From Early and Strategic Development through to Materials Application. In *Applications of Polyhedral Oligomeric Silsesquioxanes*, Hartmann-Thompson, C., Ed. Springer Netherlands: **2011**; Chapter 1, pp 1-46.
19. Dolbecq, A.; Dumas, E.; Mayer, C. R.; Mialane, P., Hybrid Organic–Inorganic Polyoxometalate Compounds: From Structural Diversity to Applications. *Chem. Rev.* **2010**, *110* (10), 6009-6048.
20. Song, Y.-F.; Long, D.-L.; Ritchie, C.; Cronin, L., Nanoscale polyoxometalate-based inorganic/organic hybrids. *Chem. Rec.* **2011**, *11* (3), 158-171.
21. Sivakumar, R.; Thomas, J.; Yoon, M., Polyoxometalate-based molecular/nano composites: Advances in environmental remediation by photocatalysis and biomimetic approaches to solar energy conversion. *J. Photochem. Photobiol. C* **2012**, *13* (4), 277-298.
22. Berardi, S.; Carraro, M.; Sartorel, A.; Modugno, G.; Bonchio, M., Hybrid Polyoxometalates: Merging Organic and Inorganic Domains for Enhanced Catalysis and Energy Applications. *Isr. J. Chem.* **2011**, *51* (2), 259-274.
23. Proust, A.; Matt, B.; Villanneau, R.; Guillemot, G.; Gouzerh, P.; Izzet, G., Functionalization and post-functionalization: a step towards polyoxometalate-based materials. *Chem. Soc. Rev.* **2012**, *41* (22), 7605-7622.
24. Wu, H.; Yang, H.-K.; Wang, W., Covalently-linked polyoxometalate-polymer hybrids: optimizing synthesis, appealing structures and prospective applications. *New J. Chem.* **2016**, *40* (2), 886-897.
25. Qi, W.; Wu, L., Polyoxometalate/polymer hybrid materials: fabrication and properties. *Polym. Int.* **2009**, *58* (11), 1217-1225.
26. Ren, Y.; Wang, M.; Chen, X.; Yue, B.; He, H., Heterogeneous Catalysis of Polyoxometalate Based Organic–Inorganic Hybrids. *Materials* **2015**, *8* (4), 1545.

27. Schubert, U., Cluster-based inorganic-organic hybrid materials. *Chem. Soc. Rev.* **2011**, *40* (2), 575-582.
28. Gross, S., Oxocluster-reinforced organic-inorganic hybrid materials: effect of transition metal oxoclusters on structural and functional properties. *J. Mater. Chem.* **2011**, *21* (40), 15853-15861.
29. Carraro, M.; Gross, S., Hybrid Materials Based on the Embedding of Organically Modified Transition Metal Oxoclusters or Polyoxometalates into Polymers for Functional Applications: A Review. *Materials* **2014**, *7* (5), 3956-3989.
30. Landfester, K., Miniemulsion Polymerization and the Structure of Polymer and Hybrid Nanoparticles. *Angew. Chem. Int. Ed.* **2009**, *48* (25), 4488-4507.
31. Hu, J.; Chen, M.; Wu, L., Organic-inorganic nanocomposites synthesized via miniemulsion polymerization. *Polym. Chem.* **2011**, *2* (4), 760-772.
32. Hood, M.; Mari, M.; Muñoz-Espí, R., Synthetic Strategies in the Preparation of Polymer/Inorganic Hybrid Nanoparticles. *Materials* **2014**, *7* (5), 4057-4087.
33. Pablico, M. H.; Mertzman, J. E.; Japp, E. A.; Boncher, W. L.; Nishida, M.; Van Keuren, E.; Lofland, S. E.; Dollahon, N.; Rubinson, J. F.; Holman, K. T.; Stoll, S. L., Miniemulsion Synthesis of Metal-Oxo Cluster Containing Copolymer Nanobeads. *Langmuir* **2011**, *27* (20), 12575-12584.
34. Fischer, V.; Lieberwirth, I.; Jakob, G.; Landfester, K.; Muñoz-Espí, R., Metal Oxide/Polymer Hybrid Nanoparticles with Versatile Functionality Prepared by Controlled Surface Crystallization. *Adv. Funct. Mater.* **2013**, *23* (4), 451-466.
35. Li, H.; Li, P.; Yang, Y.; Qi, W.; Sun, H.; Wu, L., Incorporation of Polyoxometalates Into Polystyrene Latex by Supramolecular Encapsulation and Miniemulsion Polymerization. *Macromol. Rapid Commun.* **2008**, *29* (5), 431-436.
36. Mari, M.; Müller, B.; Landfester, K.; Muñoz-Espí, R., Ceria/Polymer Hybrid Nanoparticles as Efficient Catalysts for the Hydration of Nitriles to Amides. *ACS Appl. Mater. Interf.* **2015**, *7* (20), 10727-10733.
37. Schoth, A.; Adurahim, E. S.; Bahattab, M. A.; Landfester, K.; Muñoz-Espí, R., Waterborne Polymer/Silica Hybrid Nanoparticles and Their Structure in Coatings. *Macromol. React. Eng.* **2016**, *10* (1), 47-54.
38. Livage, J.; Sanchez, C., Sol-gel chemistry. *J. Non-Cryst. Solids* **1992**, *145*, 11-19.
39. Schubert, U.; Huesing, N.; Lorenz, A., Hybrid Inorganic-Organic Materials by Sol-Gel Processing of Organofunctional Metal Alkoxides. *Chem. Mater.* **1995**, *7* (11), 2010-2027.
40. Schubert, U., Polymers Reinforced by Covalently Bonded Inorganic Clusters. *Chem. Mater.* **2001**, *13* (10), 3487-3494.

41. Kickelbick, G., Hybrid Materials: Synthesis, Characterization and Application. Wiley-VCH Verlag GmbH & Co. KGaA: Weinheim, Germany **2007**, (), .
42. Kickelbick, G.; Feth, M. P.; Bertagnolli, H.; Puchberger, M.; Holzinger, D.; Gross, S., Formation of organically surface-modified metal oxo clusters from carboxylic acids and metal alkoxides: a mechanistic study. *J. Chem. Soc. Dalton* **2002**, (20), 3892-3898.
43. Palacio, F.; Oliete, P.; Schubert, U.; Mijatovic, I.; Husing, N.; Peterlik, H., Magnetic behaviour of a hybrid polymer obtained from ethyl acrylate and the magnetic cluster $Mn_{12}O_{12}(acrylate)_{16}$. *J. Mater. Chem.* **2004**, *14* (12), 1873-1878.
44. Mayer, C. R.; Cabuil, V.; Lalot, T.; Thouvenot, R., Incorporation of Magnetic Nanoparticles in New Hybrid Networks Based on Heteropolyanions and Polyacrylamide. *Angew. Chem. Int. Ed.* **1999**, *38* (24), 3672-3675.
45. Moraru, B.; Hüsing, N.; Kickelbick, G.; Schubert, U.; Fratzl, P.; Peterlik, H., Inorganic–Organic Hybrid Polymers by Polymerization of Methacrylate- or Acrylate-Substituted Oxotitanium Clusters with Methyl Methacrylate or Methacrylic Acid. *Chem. Mater.* **2002**, *14* (6), 2732-2740.
46. Albinati, A.; Faccini, F.; Gross, S.; Kickelbick, G.; Rizzato, S.; Venzo, A., New methacrylate-functionalized ba and ba-ti oxoclusters as potential nanosized building blocks for inorganic-organic hybrid materials: synthesis and characterization. *Inorg. Chem.* **2007**, *46* (9), 3459-66.
47. Trimmel, G.; Gross, S.; Kickelbick, G.; Schubert, U., Swelling behavior and thermal stability of poly(methylmethacrylate) crosslinked by the oxozirconium cluster $Zr_4O_2(methacrylate)_{12}$. *Appl. Organomet. Chem.* **2001**, *15* (5), 401-406.
48. Kickelbick, G.; Schubert, U., Oxozirconium Methacrylate Clusters: $Zr_6(OH)_4O_4(OMc)_{12}$ and $Zr_4O_2(OMc)_{12}$ (OMc = Methacrylate). *Chem. Ber.* **1997**, *130* (4), 473-478.
49. Gross, S.; Di Noto, V.; Schubert, U., Dielectric investigation of inorganic–organic hybrid film based on zirconium oxocluster-crosslinked PMMA. *J. Non-Cryst. Solids* **2003**, *322* (1–3), 154-159.
50. Girardi, F.; Cappelletto, E.; Sandak, J.; Bochicchio, G.; Tessadri, B.; Palanti, S.; Feci, E.; Di Maggio, R., Hybrid organic–inorganic materials as coatings for protecting wood. *Prog. Org. Coat.* **2014**, *77* (2), 449-457.
51. Benedetti, C.; Cazzolaro, A.; Carraro, M.; Graf, R.; Landfester, K.; Gross, S.; Muñoz-Espí, R., Dual Role of Zirconium Oxoclusters in Hybrid Nanoparticles: Cross-Linkers and Catalytic Sites. *ACS Appl. Mater. Interf.* **2016**, *8* (39), 26275-26284.
52. Faccioli, F.; Bauer, M.; Pedron, D.; Sorarù, A.; Carraro, M.; Gross, S., Hydrolytic Stability and Hydrogen Peroxide Activation of Zirconium-Based Oxoclusters. *Eur. J. Inorg. Chem.* **2015**, *2015* (2), 210-225.

53. Doeuff, S.; Dromzee, Y.; Taulelle, F.; Sanchez, C., Synthesis and solid- and liquid-state characterization of a hexameric cluster of titanium(IV): $\text{Ti}_6(\mu_2\text{-O})_2(\mu_3\text{-O})_2(\mu_2\text{-OC}_4\text{H}_9)_2(\text{OC}_4\text{H}_9)_6(\text{OCOCH}_3)_8$. *Inorg. Chem.* **1989**, 28 (25), 4439-4445.
54. Rozes, L.; Steunou, N.; Fornasieri, G.; Sanchez, C., Titanium-Oxo Clusters, Versatile Nanobuilding Blocks for the Design of Advanced Hybrid Materials. *Monatsh. Chem.* **2006**, 137 (5), 501-528.
55. Rozes, L.; Cochet, S.; Frot, T.; Fornasieri, G.; Sassoie, C.; Popall, M.; Sanchez, C., Titanium Oxo-Clusters: Versatile Nano-Objects for the Design of Hybrid Compounds. *MRS Symp. Proc.* **2007**, 1007.
56. Rozes, L.; Sanchez, C., Titanium oxo-clusters: precursors for a Lego-like construction of nanostructured hybrid materials. *Chem. Soc. Rev.* **2011**, 40 (2), 1006-1030.
57. Schubert, U., Chemical modification of titanium alkoxides for sol-gel processing. *J. Mater. Chem.* **2005**, 15 (35-36), 3701-3715.
58. Trabelsi, S.; Janke, A.; Hässler, R.; Zafeiropoulos, N. E.; Fornasieri, G.; Bocchini, S.; Rozes, L.; Stamm, M.; Gérard, J.-F.; Sanchez, C., Novel Organo-Functional Titanium-oxo-cluster-Based Hybrid Materials with Enhanced Thermomechanical and Thermal Properties. *Macromolecules* **2005**, 38 (14), 6068-6078.
59. Kickelbick, G.; Schubert, U., An Unusual Ring Structure of an Oligomeric Oxotitanium Alkoxide Carboxylate. *Eur. J. Inorg. Chem.* **1998**, 1998 (2), 159-161.
60. Di Maggio, R.; Dire, S.; Callone, E.; Girardi, F.; Kickelbick, G., Hybrid organic-inorganic materials using zirconium based NBBs and vinyl trimethoxysilane: Effect of pre-hydrolysis of silane. *Polymer* **2010**, 51, 832-841.
61. Cochet, S.; Rozes, L.; Popall, M.; Sanchez, C., Titanium oxo-clusters as nanobuilding blocks for microsystems technology. *Mater. Sci. Eng., C* **2007**, 27 (5-8), 1401-1405.
62. Faccini, F.; Fric, H.; Schubert, U.; Wendel, E.; Tsetsgee, O.; Müller, K.; Bertagnolli, H.; Venzo, A.; Gross, S., ω -Mercapto-functionalized hafnium- and zirconium-oxoclusters as nanosized building blocks for inorganic-organic hybrid materials: synthesis, characterization and photothiol-ene polymerization. *J. Mater. Chem.* **2007**, 17 (31), 3297-3307.
63. Trimmel, G.; Moraru, B.; Gross, S.; Di Noto, V.; Schubert, U., Cross-linking of poly(methyl methacrylate) by oxozirconate and oxotitanate clusters. *Macromol. Symp.* **2001**, 175 (1), 357-366.
64. Gross, S.; Trimmel, G.; Schubert, U.; Noto, V. D., Inorganic-organic hybrid materials-from poly(methylmethacrylate) -crosslinked by an organically modified -oxozirconium cluster. Synthesis and -characterization. *Polym. Adv. Technol.* **2002**, 13 (3-4), 254-259.
65. Koch, T.; Kogler, F. R.; Schubert, U.; Seidler, S., Mechanical Properties of Organic-Inorganic Hybrid Materials Determined by Indentation Techniques. *Monatsh. Chem.* **2007**, 138 (4), 293-299.

66. Puchegger, S.; Renhoffer, H.; Kogler, F. R.; Loidl, D.; Bernstorff, S.; Schubert, U.; Peterlik, H., Suppression of Crazeing in Polystyrene Crosslinked with a Multifunctional Zirconium Oxo Cluster Observed In Situ during Tensile Tests. *Macromol. Rapid Commun.* **2007**, *28* (22), 2145-2150.
67. Gao, Y.; Choudhury, N. R.; Matisons, J.; Schubert, U.; Moraru, B., Part 2: Inorganic–Organic Hybrid Polymers by Polymerization of Methacrylate-Substituted Oxotitanium Clusters with Methyl Methacrylate: Thermomechanical and Morphological Properties. *Chem. Mater.* **2002**, *14* (11), 4522-4529.
68. Kogler, F. R.; Koch, T.; Peterlik, H.; Seidler, S.; Schubert, U., Mechanical, thermomechanical, and thermal properties of polystyrene crosslinked with a multifunctional zirconium oxo cluster. *J. Polym. Sci. Pol. Phys.* **2007**, *45* (16), 2215-2231.
69. Sangermano, M.; Gross, S.; Pracella, L.; Priola, A.; Rizza, G., Hybrid Organic-Inorganic Nanostructured Acrylic Films Based on Methacrylate Modified Zirconium Oxocluster. *Macromol. Chem. Physic.* **2007**, *208* (16), 1730-1736.
70. Gao, Y.; Kogler, F. R.; Schubert, U., Improvement of the thermal stability of cluster-crosslinked polystyrene and poly(methyl methacrylate) by optimization of the polymerization conditions. *J. Polym. Sci., Part A: Polym. Chem.* **2005**, *43* (24), 6586-6591.
71. Schubert, U.; Gao, Y.; Kogler, F. R., Tuning the properties of nanostructured inorganic–organic hybrid polymers obtained from metal oxide clusters as building blocks. *Prog. Solid State Ch.* **2007**, *35* (1), 161-170.
72. Soler-Illia, G. J. d. A. A.; Scolas, E.; Louis, A.; Albouy, P.-A.; Sanchez, C., Design of meso-structured titanium oxo based hybrid organic-inorganic networks. *New J. Chem.* **2001**, *25* (1), 156-165.
73. Di Maggio, R.; Fambri, L.; Cesconi, M.; Vaona, W., Inorganic–Organic Clusters of Zirconium as Initiators of Hydroxyethyl Methacrylate Polymerization. *Macromolecules* **2002**, *35* (14), 5342-5344.
74. Girardi, F.; Maggini, S.; Della Volpe, C.; Cappelletto, E.; Mueller, K.; Siboni, S.; Di Maggio, R., Hybrid organic–inorganic materials on paper: surface and thermo-mechanical properties. *J. Sol-Gel Sci. Technol.* **2011**, *60* (3), 315-323.
75. Maggini, S.; Feci, E.; Cappelletto, E.; Girardi, F.; Palanti, S.; Di Maggio, R., (I/O) Hybrid Alkoxysilane/Zirconium-Oxocluster Copolymers as Coatings for Wood Protection. *ACS Appl. Mater. Interf.* **2012**, *4* (9), 4871-4881.
76. Graziola, F.; Girardi, F.; Bauer, M.; Di Maggio, R.; Rovezzi, M.; Bertagnolli, H.; Sada, C.; Rossetto, G.; Gross, S., UV-photopolymerisation of poly(methyl methacrylate)-based inorganic-organic hybrid coatings and bulk samples reinforced with methacrylate-modified zirconium oxocluster. *Polymer* **2008**, *49*, 4332-4343.
77. Girardi, F.; Graziola, F.; Aldighieri, P.; Fedrizzi, L.; Gross, S.; Di Maggio, R., Inorganic–organic hybrid materials with zirconium oxoclusters as protective coatings on aluminium alloys. *Prog. Org. Coat.* **2008**, *62* (4), 376-381.

78. Gibin, G.; Lorenzetti, A.; Callone, E.; Dirè, S.; Dolcet, P.; Venzo, A.; Causin, V.; Marigo, A.; Modesti, M.; Gross, S., Smart and Covalently Cross-Linked: Hybrid Shape Memory Materials Reinforced through Covalent Bonds by Zirconium Oxoclusters. *ChemPlusChem* **2016**, *81* (3), 338-350.
79. Willemin, S.; Donnadiou, B.; Lecren, L.; Henner, B.; Clerac, R.; Guerin, C.; Meyer, A.; Pokrovskii, A. V.; Larionova, J., Synthesis and characterization of magnetic organic-inorganic nanocomposites based on the $[\text{Mn}_2\text{O}_{12}\{\text{CH}_2\text{C}(\text{CH}_3)\text{COO}\}_{16}(\text{H}_2\text{O})_4]$ building block. *New J. Chem.* **2004**, *28* (8), 919-928.
80. Sessoli, R.; Gatteschi, D.; Caneschi, A.; Novak, M. A., Magnetic bistability in a metal-ion cluster. *Nature* **1993**, *365* (6442), 141-143.
81. Caneschi, A.; Gatteschi, D.; Sangregorio, C.; Sessoli, R.; Sorace, L.; Cornia, A.; Novak, M. A.; Paulsen, C.; Wernsdorfer, W., The molecular approach to nanoscale magnetism. *J. Magn. Mater.* **1999**, *200* (1-3), 182-201.
82. Mukhin, A. A.; Travkin, V. D.; Zvezdin, A. K.; Caneschi, A.; Gatteschi, D.; Sessoli, R., Electron transitions in magnetic clusters $\text{Mn}_{12}\text{-Ac}$ at submillimeter wavelengths. *Physica B: Condensed Matter* **2000**, *284-288*, Part 2, 1221-1222.
83. Cornia, A.; Affronte, M.; Gatteschi, D.; Jansen, A. G. M.; Caneschi, A.; Sessoli, R., High-field torque magnetometry for investigating magnetic anisotropy in Mn_{12} -acetate nanomagnets. *J. Magn. Mater.* **2001**, *226-230*, Part 2, 2012-2014.
84. Pablico-Lansigan, M. H.; Hickling, W. J.; Japp, E. A.; Rodriguez, O. C.; Ghosh, A.; Albanese, C.; Nishida, M.; Van Keuren, E.; Fricke, S.; Dollahon, N.; Stoll, S. L., Magnetic nanobeads as potential contrast agents for magnetic resonance imaging. *ACS nano* **2013**, *7* (10), 9040-8.
85. Ferreira, R. A. S.; Oliveira, D. C.; Maia, L. Q.; Vicente, C. M. S.; André, P. S.; Bermudez, V. Z.; Ribeiro, S. J. L.; Carlos, L. D., Enhanced photoluminescence features of Eu^{3+} -modified di-ureasil-zirconium oxocluster organic-inorganic hybrids. *Opt. Mater.* **2010**, *32* (12), 1587-1591.
86. Sanchez, C.; Lebeau, B., Design and Properties of Hybrid Organic-Inorganic Nanocomposites for Photonics. *MRS Bull.* **2001**, *26* (5), 377-387.
87. Oliveira, D. C.; Macedo, A. G.; Silva, N. J. O.; Molina, C.; Ferreira, R. A. S.; André, P. S.; Dahmouche, K.; Bermudez, V. D. Z.; Messaddeq, Y.; Ribeiro, S. J. L.; Carlos, L. D., Photopatternable Di-ureasil-Zirconium Oxocluster Organic-Inorganic Hybrids As Cost Effective Integrated Optical Substrates. *Chem. Mater.* **2008**, *20* (11), 3696-3705.
88. Haas, K.-H.; Wolter, H., Synthesis, properties and applications of inorganic-organic copolymers (ORMOCER®s). *Curr. Opin. Solid State Mater. Sci.* **1999**, *4* (6), 571-580.
89. Dan-Hardi, M.; Serre, C.; Frot, T.; Rozes, L.; Maurin, G.; Sanchez, C.; Férey, G., A New Photoactive Crystalline Highly Porous Titanium(IV) Dicarboxylate. *J. Am. Chem. Soc.* **2009**, *131* (31), 10857-10859.

90. Gross, S.; Noto, V. D.; Kickelbick, G.; Schubert, U., Cluster-Crosslinked Inorganic–Organic Hybrid Polymers: Influence of the Cluster Type on the Materials Properties. *MRS Symp. Proc.* **2002**, 726.
91. Gross, S.; Zattin, A.; Di Noto, V.; Lavina, S., Metal Oxoclusters as Molecular Building Blocks for the Development of Nanostructured Inorganic–Organic Hybrid Thin Films. *Monatsh. Chem.* **2006**, 137 (5), 583-593.
92. Gross, S.; Camozzo, D.; Di Noto, V.; Armelao, L.; Tondello, E., PMMA: A key macromolecular component for dielectric low- κ hybrid inorganic–organic polymer films. *Eur. Polym. J.* **2007**, 43 (3), 673-696.
93. Vigolo, M.; Borsacchi, S.; Sorarù, A.; Geppi, M.; Smarsly, B. M.; Dolcet, P.; Rizzato, S.; Carraro, M.; Gross, S., Engineering of oxoclusters-reinforced polymeric materials with application as heterogeneous oxydesulfurization catalysts. *Appl. Catal., B* **2016**, 182, 636-644.
94. Sanchez, C.; In, M., Molecular design of alkoxide precursors for the synthesis of hybrid organic-inorganic gels. *J. Non-Cryst. Solids* **1992**, 147, 1-12.
95. Kickelbick, G.; Holzinger, D.; Brick, C.; Trimmel, G.; Moons, E., Hybrid Inorganic–Organic Core–Shell Nanoparticles from Surface-Functionalized Titanium, Zirconium, and Vanadium Oxo Clusters. *Chem. Mater.* **2002**, 14 (10), 4382-4389.
96. Gao, Y.; Kogler, F. R.; Peterlik, H.; Schubert, U., Ring-opening metathesis polymerizations with norbornene carboxylate-substituted metal oxo clusters. *J. Mater. Chem.* **2006**, 16 (32), 3268-3276.
97. Sangermano, M.; Gross, S.; Priola, A.; Rizza, G.; Sada, C., Thiol-ene Hybrid Organic/Inorganic Nanostructured Coatings Based on Thiol-Functionalized Zirconium Oxoclusters. *Macromol. Chem. Physic.* **2007**, 208 (23), 2560-2568.
98. Trimmel, G.; Fratzl, P.; Schubert, U., Cross-Linking of Poly(methyl methacrylate) by the Methacrylate-Substituted Oxozirconium Cluster $Zr_6(OH)_4O_4(\text{Methacrylate})_{12}$. *Chem. Mater.* **2000**, 12 (3), 602-604.
99. Kreutzer, J.; Qin, X.-H.; Gorsche, C.; Peterlik, H.; Liska, R.; Schubert, U., Variation of the crosslinking density in cluster-reinforced polymers. *Mater. Today Comm.* **2015**, 5, 10-17.
100. Lovell, P. A.; El-Aasser, M. S., *Emulsion Polymerization and Emulsion Polymers*. John Wiley and Sons: **1997**.
101. Sakai, T., Surfactant-free emulsions. *Curr. Opin. Colloid. In.* **2008**, 13 (4), 228-235.
102. Schoth, A.; Landfester, K.; Muñoz-Espí, R., Surfactant-Free Polyurethane Nanocapsules via Inverse Pickering Miniemulsion. *Langmuir* **2015**, 31 (13), 3784-3788.
103. Landfester, K., The Generation of Nanoparticles in Miniemulsions. *Adv. Mater.* **2001**, 13 (10), 765-768.

104. Landfester, K., Miniemulsions for Nanoparticle Synthesis. In *Colloid Chemistry II*, Antonietti, M., Ed. Springer Berlin Heidelberg: **2003**; Chapter 4, pp 75-123.
105. Landfester, K., Miniemulsion polymerization and the structure of polymer and hybrid nanoparticles. *Angew. Chem. Int. Ed. Engl.* **2009**, *48* (25), 4488-507.
106. Asua, J. M., Miniemulsion polymerization. *Prog. Polym. Sci.* **2002**, *27* (7), 1283-1346.
107. Rosen, M. J.; Kunjappu, J., Surfactants and interfacial phenomena. Hoboken, NJ, USA: Wiley. DOI **2004**, *10* (0471670), 561.
108. Cosgrove, T., *Colloid science: principles, methods and applications*. John Wiley & Sons: **2010**.
109. Tadros, T. F., Physical Chemistry of Surfactant Solutions. In *Applied Surfactants*, Wiley-VCH Verlag GmbH & Co. KGaA: **2005**, pp 19-51.
110. Voorhees, P. W., The theory of Ostwald ripening. *J. Stat. Phys.* **1985**, *38* (1), 231-252.
111. Davis, S. S.; Round, H. P.; Purewal, T. S., Ostwald ripening and the stability of emulsion systems: an explanation for the effect of an added third component. *J. Colloid Interface Sci.* **1981**, *80* (2), 508-511.
112. Moore, J. C., Gel permeation chromatography. I. A new method for molecular weight distribution of high polymers. *J. Polym. Sci. A Polym. Chem.* **1964**, *2* (2), 835-843.
113. Hou, X.; Amais, R. S.; Jones, B. T.; Donati, G. L., *Encyclopedia of Analytical Chemistry*. **2016**; Vol. Inductively Coupled Plasma Optical Emission Spectrometry.
114. Vogel, N.; Hauser, C. P.; Schuller, K.; Landfester, K.; Weiss, C. K., Accurate Elemental Analysis of Metal-Containing Polymer Latexes Using ICP-Optical Emission Spectrometry. *Macromol. Chem. Physic.* **2010**, *211* (12), 1355-1368.
115. Gross, S.; Bauer, M., EXAFS as Powerful Analytical Tool for the Investigation of Organic-Inorganic Hybrid Materials. *Adv. Funct. Mater.* **2010**, *20* (23), 4026-4047.
116. Goldberg, W. I., Dynamic light scattering. *Am. J. Phys.* **1999**, *67* (12), 1152-1160.
117. Ma, X.; Sun, L.; Song, C., A new approach to deep desulfurization of gasoline, diesel fuel and jet fuel by selective adsorption for ultra-clean fuels and for fuel cell applications. *Catal. Today* **2002**, *77* (1-2), 107-116.
118. Sampanthar, J. T.; Xiao, H.; Dou, J.; Nah, T. Y.; Rong, X.; Kwan, W. P., A novel oxidative desulfurization process to remove refractory sulfur compounds from diesel fuel. *Appl. Catal. B* **2006**, *63* (1-2), 85-93.
119. Zhu, W.; Li, H.; Jiang, X.; Yan, Y.; Lu, J.; He, L.; Xia, J., Commercially available molybdenic compound-catalyzed ultra-deep desulfurization of fuels in ionic liquids. *Green Chem.* **2008**, *10* (6), 641-646.

120. Jiang, Y.; Zhu, W.; Li, H.; Yin, S.; Liu, H.; Xie, Q., Oxidative Desulfurization of Fuels Catalyzed by Fenton-Like Ionic Liquids at Room Temperature. *ChemSusChem* **2011**, *4* (3), 399-403.
121. Haw, K.-G.; Bakar, W. A. W. A.; Ali, R.; Chong, J.-F.; Kadir, A. A. A., Catalytic oxidative desulfurization of diesel utilizing hydrogen peroxide and functionalized-activated carbon in a biphasic diesel–acetonitrile system. *Fuel Process. Technol.* **2010**, *91* (9), 1105-1112.
122. Carraro, M.; Fiorani, G.; Mognon, L.; Caneva, F.; Gardan, M.; Maccato, C.; Bonchio, M., Hybrid Polyoxotungstates as Functional Comonomers in New Cross-Linked Catalytic Polymers for Sustainable Oxidation with Hydrogen Peroxide. *Chem. Eur. J.* **2012**, *18* (41), 13195-13202.
123. Carraro, M.; Nsouli, N.; Oelrich, H.; Sartorel, A.; Sorarù, A.; Mal, S. S.; Scorrano, G.; Walder, L.; Körtz, U.; Bonchio, M., Reactive Zr^{IV} and Hf^{IV} Butterfly Peroxides on Polyoxometalate Surfaces: Bridging the Gap between Homogeneous and Heterogeneous Catalysis. *Chem. Eur. J.* **2011**, *17* (30), 8371-8378.
124. Holm, R. H., Metal-centered oxygen atom transfer reactions. *Chem. Rev.* **1987**, *87* (6), 1401-1449.
125. Dickman, M. H.; Pope, M. T., Peroxo and Superoxo Complexes of Chromium, Molybdenum, and Tungsten. *Chem. Rev.* **1994**, *94* (3), 569-584.
126. Kaczorowska, K.; Kolarska, Z.; Mitka, K.; Kowalski, P., Oxidation of sulfides to sulfoxides. Part 2: Oxidation by hydrogen peroxide. *Tetrahedron* **2005**, *61* (35), 8315-8327.
127. Conte, V.; Di Furia, F.; Licini, G., Liquid phase oxidation reactions by peroxides in the presence of vanadium complexes. *Appl. Catal. A-Gen.* **1997**, *157* (1-2), 335-361.
128. Noyori, R.; Aoki, M.; Sato, K., Green oxidation with aqueous hydrogen peroxide. *Chem. Commun.* **2003**, (16), 1977-1986.
129. Lane, B. S.; Burgess, K., Metal-Catalyzed Epoxidations of Alkenes with Hydrogen Peroxide. *Chem. Rev.* **2003**, *103* (7), 2457-2474.
130. Jahier, C.; Mal, S. S.; Körtz, U.; Nlate, S., Dendritic Zirconium-Peroxotungstosilicate Hybrids: Synthesis, Characterization, and Use as Recoverable and Reusable Sulfide Oxidation Catalysts. *Eur. J. Inorg. Chem.* **2010**, *2010* (10), 1559-1566.
131. Antonova, N. S.; Carbó, J. J.; Körtz, U.; Kholdeeva, O. A.; Poblet, J. M., Mechanistic Insights into Alkene Epoxidation with H₂O₂ by Ti- and other TM-Containing Polyoxometalates: Role of the Metal Nature and Coordination Environment. *J. Am. Chem. Soc.* **2010**, *132* (21), 7488-7497.
132. Hecht, L. L.; Schoth, A.; Muñoz-Espí, R.; Javadi, A.; Köhler, K.; Miller, R.; Landfester, K.; Schuchmann, H. P., Determination of the Ideal Surfactant Concentration in Miniemulsion Polymerization. *Macromol. Chem. Physic.* **2013**, *214* (7), 812-823.

133. Gross, S.; Bauer, M., EXAFS as Powerful Analytical Tool for the Investigation of Organic–Inorganic Hybrid Materials. *Adv. Funct. Mater.* **2010**, *20* (23), 4026-4047.
134. Kang, Y.; Seo, Y.-H.; Kim, D. W.; Lee, C., Effect of poly(ethylene glycol) dimethyl ether plasticizer on ionic conductivity of cross-linked poly[siloxane-g-oligo(ethylene oxide)] solid polymer electrolytes. *Macromol. Res.* **2004**, *12* (5), 431-436.
135. Sato, K.; Hyodo, M.; Aoki, M.; Zheng, X.-Q.; Noyori, R., Oxidation of sulfides to sulfoxides and sulfones with 30% hydrogen peroxide under organic solvent- and halogen-free conditions. *Tetrahedron* **2001**, *57* (13), 2469-2476.
136. Jeyakumar, K.; Chand, D. K., Selective oxidation of sulfides to sulfoxides and sulfones at room temperature using H₂O₂ and a Mo(VI) salt as catalyst. *Tetrahedron Lett.* **2006**, *47* (27), 4573-4576.
137. Gamelas, C. A.; Lourenço, T.; da Costa, A. P.; Simplício, A. L.; Royo, B.; Romão, C. C., Selective and mild oxidation of sulfides to sulfoxides or sulfones using H₂O₂ and Cp*Mo(CO)₃Cl as catalysts. *Tetrahedron Lett.* **2008**, *49* (32), 4708-4712.
138. Al-Maksoud, W.; Daniele, S.; Sorokin, A. B., Practical oxidation of sulfides to sulfones by H₂O₂ catalysed by titanium catalyst. *Green Chem.* **2008**, *10* (4), 447-451.
139. Licini, G.; Mba, M.; Zonta, C., Amine triphenolate complexes: synthesis, structure and catalytic activity. *Dalton Trans.* **2009**, (27), 5265-5277.
140. Bahrami, K., Selective oxidation of sulfides to sulfoxides and sulfones using hydrogen peroxide (H₂O₂) in the presence of zirconium tetrachloride. *Tetrahedron Lett.* **2006**, *47* (12), 2009-2012.
141. Sheldon, R. A.; Arends, I. W. C. E.; ten Brink, G.-J.; Dijkman, A., Green, Catalytic Oxidations of Alcohols. *Acc. Chem. Res.* **2002**, *35* (9), 774-781.
142. Romano, D.; Villa, R.; Molinari, F., Preparative Biotransformations: Oxidation of Alcohols. *ChemCatChem* **2012**, *4* (6), 739-749.
143. Davis, S. E.; Ide, M. S.; Davis, R. J., Selective oxidation of alcohols and aldehydes over supported metal nanoparticles. *Green Chem.* **2013**, *15* (1), 17-45.
144. Venturello, C.; Alneri, E.; Ricci, M., A new, effective catalytic system for epoxidation of olefins by hydrogen peroxide under phase-transfer conditions. *J. Org. Chem.* **1983**, *48* (21), 3831-3833.
145. Ciriminna, R.; Pandarus, V.; Béland, F.; Xu, Y.-J.; Pagliaro, M., Heterogeneously Catalyzed Alcohol Oxidation for the Fine Chemical Industry. *Org. Process Res. Dev.* **2015**, *19* (11), 1554-1558.
146. Rusconi, F.; Valton, É.; Nguyen, R.; Dufourc, E., Quantification of Sodium Dodecyl Sulfate in Microliter-Volume Biochemical Samples by Visible Light Spectroscopy. *Anal. Biochem.* **2001**, *295* (1), 31-37.

147. Pelton, R. H.; Chibante, P., Preparation of aqueous latices with N-isopropylacrylamide. *Colloids Surf.* **1986**, *20* (3), 247-256.
148. Pelton, R., Temperature-sensitive aqueous microgels. *Adv. Colloid Interface Sci.* **2000**, *85* (1), 1-33.
149. Schild, H. G., Poly(N-isopropylacrylamide): experiment, theory and application. *Prog. Polym. Sci.* **1992**, *17* (2), 163-249.
150. Deshmukh, S. A.; Sankaranarayanan, S. K. R. S.; Suthar, K.; Mancini, D. C., Role of Solvation Dynamics and Local Ordering of Water in Inducing Conformational Transitions in Poly(N-isopropylacrylamide) Oligomers through the LCST. *J. Phys. Chem. B* **2012**, *116* (9), 2651-2663.
151. Singh, R.; Deshmukh, S. A.; Kamath, G.; Sankaranarayanan, S. K. R. S.; Balasubramanian, G., Controlling the aqueous solubility of PNIPAM with hydrophobic molecular units. *Comput. Mater. Sci.* **2017**, *126*, 191-203.
152. Aseyev, V. O.; Tenhu, H.; Winnik, F. M., Temperature Dependence of the Colloidal Stability of Neutral Amphiphilic Polymers in Water. In *Conformation-Dependent Design of Sequences in Copolymers II*, Khokhlov, A. R., Ed. Springer Berlin Heidelberg: Berlin, Heidelberg, **2006**, pp 1-85.
153. Zhang, J.; Zhang, M.; Tang, K.; Verpoort, F.; Sun, T., Polymer-Based Stimuli-Responsive Recyclable Catalytic Systems for Organic Synthesis. *Small* **2014**, *10* (1), 32-46.
154. Bergbreiter, D. E.; Case, B. L.; Liu, Y.-S.; Caraway, J. W., Poly(N-isopropylacrylamide) Soluble Polymer Supports in Catalysis and Synthesis. *Macromolecules* **1998**, *31* (18), 6053-6062.
155. Jiang, X.; Xiong, D. A.; An, Y.; Zheng, P.; Zhang, W.; Shi, L., Thermoresponsive hydrogel of poly(glycidyl methacrylate-co-N-isopropylacrylamide) as a nanoreactor of gold nanoparticles. *J. Polym. Sci., Part A: Polym. Chem.* **2007**, *45* (13), 2812-2819.
156. Li, D.; Cui, Y.; Wang, K.; He, Q.; Yan, X.; Li, J., Thermosensitive Nanostructures Comprising Gold Nanoparticles Grafted with Block Copolymers. *Adv. Funct. Mater.* **2007**, *17* (16), 3134-3140.
157. Kimura, M.; Kato, M.; Muto, T.; Hanabusa, K.; Shirai, H., Temperature-Sensitive Dendritic Hosts: Synthesis, Characterization, and Control of Catalytic Activity. *Macromolecules* **2000**, *33* (4), 1117-1119.
158. Grewer, T.; Rogers, R., *Thermal hazards of chemical reactions, volume 4, (industrial safety series)*. Elsevier: **2015**.
159. Ball, R., Oscillatory thermal instability and the Bhopal disaster. *Process Saf. Environ. Prot.* **2011**, *89* (5), 317-322.
160. Copelli, S.; Derudi, M.; Cattaneo, C. S.; Nano, G.; Raboni, M.; Torretta, V.; Rota, R., Synthesis of 4-Chloro-3-nitrobenzotrifluoride: Industrial thermal runaway simulation due to cooling system failure. *Process Saf. Environ. Prot.* **2014**, *92* (6), 659-668.

161. Eissen, M.; Zogg, A.; Hungerbühler, K., The runaway scenario in the assessment of thermal safety: simple experimental access by means of the catalytic decomposition of H₂O₂. *J. Loss. Prevent. Proc.* **2003**, *16* (4), 289-296.
162. Kanaoka, S.; Yagi, N.; Fukuyama, Y.; Aoshima, S.; Tsunoyama, H.; Tsukuda, T.; Sakurai, H., Thermosensitive Gold Nanoclusters Stabilized by Well-Defined Vinyl Ether Star Polymers: Reusable and Durable Catalysts for Aerobic Alcohol Oxidation. *J. Am. Chem. Soc.* **2007**, *129* (40), 12060-12061.
163. Hamamoto, H.; Suzuki, Y.; Yamada, Y. M. A.; Tabata, H.; Takahashi, H.; Ikegami, S., A Recyclable Catalytic System Based on a Temperature-Responsive Catalyst. *Angew. Chem. Int. Ed.* **2005**, *44* (29), 4536-4538.
164. Seuring, J.; Bayer, F. M.; Huber, K.; Agarwal, S., Upper Critical Solution Temperature of Poly(N-acryloyl glycinamide) in Water: A Concealed Property. *Macromolecules* **2012**, *45* (1), 374-384.
165. Seuring, J.; Agarwal, S., Polymers with Upper Critical Solution Temperature in Aqueous Solution. *Macromol. Rapid Commun.* **2012**, *33* (22), 1898-1920.
166. Seuring, J.; Agarwal, S., Polymers with Upper Critical Solution Temperature in Aqueous Solution: Unexpected Properties from Known Building Blocks. *ACS Macro Lett.* **2013**, *2* (7), 597-600.
167. Haas, H. C.; MacDonald, R. L.; Schuler, A. N., Synthetic thermally reversible gel systems. VI. *J. Polym. Sci. A Polym. Chem.* **1970**, *8* (12), 3405-3415.
168. Haas, H. C.; Schuler, N. W., Thermally reversible homopolymer gel systems. *J. Polym. Sci. B Polym. Lett.* **1964**, *2* (12), 1095-1096.
169. Nagaoka, H.; Ohnishi, N.; Corporation), M. E. C., *US patent 2007/0203313 A1* **2007**.
170. Ohnishi, N.; Furukawa, H.; Kataoka, K.; Corporation), K. U. N. I. o. A. I. S. a. T. C., *US patent 7,195,925 B2* **2007**.
171. Kholdeeva, O. A.; Trubitsina, T. A.; Maksimov, G. M.; Golovin, A. V.; Maksimovskaya, R. I., Synthesis, Characterization, and Reactivity of Ti(IV)-Monosubstituted Keggin Polyoxometalates. *Inorg. Chem.* **2005**, *44* (5), 1635-1642.
172. Kholdeeva, O. A., Titanium-monosubstituted polyoxometalates: relation between homogeneous and heterogeneous Ti-single-site-based catalysis. *Top. Catal.* **2006**, *40* (1), 229-243.
173. Rim, Y. S.; Bae, S.-H.; Chen, H.; De Marco, N.; Yang, Y., Recent Progress in Materials and Devices toward Printable and Flexible Sensors. *Adv. Mater.* **2016**, *28* (22), 4415-4440.
174. Alberto, P.; Raymond, C. Y. A.; Heungsoo, K.; Nicholas, A. C.; Scott, A. M., Laser 3D micro-manufacturing. *J. Phys. D: Appl. Phys.* **2016**, *49* (22), 223001.

175. de Leon, A. C.; Chen, Q.; Palaganas, N. B.; Palaganas, J. O.; Manapat, J.; Advincula, R. C., High performance polymer nanocomposites for additive manufacturing applications. *React. Funct. Polym.* **2016**, *103*, 141-155.
176. Fouassier, J.-P., Photochemistry and UV curing: a brief survey of the latest trends. In *Photochemistry & UV Curing: New Trends*, J.P. F., Ed. Research Signpost Trivandrum: **2006**, pp 1-8.
177. Ligon-Auer, S. C.; Schwentenwein, M.; Gorsche, C.; Stampfl, J.; Liska, R., Toughening of photo-curable polymer networks: a review. *Polym. Chem.* **2016**, *7* (2), 257-286.
178. Decker, C., Chapter 5 - UV-Radiation Curing of Adhesives. In *Handbook of Adhesives and Sealants*, Philippe, C., Ed. Elsevier Science Ltd: **2006**, pp 303-353.
179. Oréface, R. L.; Discacciati, J. A. C.; Neves, A. D.; Mansur, H. S.; Jansen, W. C., In situ evaluation of the polymerization kinetics and corresponding evolution of the mechanical properties of dental composites. *Polym. Test.* **2003**, *22* (1), 77-81.
180. Ikemura, K.; Endo, T., A review of the development of radical photopolymerization initiators used for designing light-curing dental adhesives and resin composites. *Dent. Mater. J.* **2010**, *29* (5), 481-501.
181. Leprince, J. G.; Palin, W. M.; Hadis, M. A.; Devaux, J.; Leloup, G., Progress in dimethacrylate-based dental composite technology and curing efficiency. *Dent. Mater.* **2013**, *29* (2), 139-156.
182. Cramer, N.; Stansbury, J.; Bowman, C., Recent advances and developments in composite dental restorative materials. *J. Dent. Res.* **2011**, *90* (4), 402-416.
183. Hageman, H. J., Photoinitiators for free radical polymerization. *Prog. Org. Coat.* **1985**, *13* (2), 123-150.
184. Denisov, E. T.; Denisova, T. G.; Pokidova, T. S., Mechanisms of Decomposition of Initiators. In *Handbook of Free Radical Initiators*, John Wiley & Sons, Inc.: **2005**, pp 1-15.
185. Chemtob, A.; Kunstler, B.; Croutxé-Barghorn, C.; Fouchard, S., Photoinduced miniemulsion polymerization. *Colloid. Polym. Sci.* **2010**, *288* (5), 579-587.
186. Tonnar, J.; Pouget, E.; Lacroix-Desmazes, P.; Boutevin, B., Synthesis of Poly(vinyl acetate)-block-poly(dimethylsiloxane)-block-poly(vinyl acetate) Copolymers by Iodine Transfer Photopolymerization in Miniemulsion. *Macromol. Symp.* **2009**, *281* (1), 20-30.
187. Fouassier, J.-P.; Merlin, A., Laser investigation of norrish type I photoscission in the photoinitiator irgacure (2,2-dimethoxy 2-phenyl-acetophenone). *J. Photochem.* **1980**, *12* (1), 17-23.
188. Lewis, F. D.; Lauterbach, R. T.; Heine, H. G.; Hartmann, W.; Rudolph, H., Photochemical .alpha. cleavage of benzoin derivatives. Polar transition states for free-radical formation. *J. Am. Chem. Soc.* **1975**, *97* (6), 1519-1525.

189. Sandner, M. R.; Osborn, C. L., Photochemistry of 2,2-dimethoxy-2-phenylacetophenone-triplet detection via "spin memory". *Tetrahedron Lett.* **1974**, *15* (5), 415-418.
190. Fouassier, J.-P.; Merlin, A., Photochemical α -cleavage and hydrogen abstraction in deoxybenzoin: a laser spectroscopy investigation. *Can. J. Chem.* **1979**, *57* (21), 2812-2817.
191. Bivigou-Koumba, A. M.; Kristen, J.; Laschewsky, A.; Müller-Buschbaum, P.; Papadakis, C. M., Synthesis of Symmetrical Triblock Copolymers of Styrene and N-isopropylacrylamide Using Bifunctional Bis(trithiocarbonate)s as RAFT Agents. *Macromol. Chem. Phys.* **2009**, *210* (7), 565-578.
192. Ilmain, F.; Tanaka, T.; Kokufuta, E., Volume transition in a gel driven by hydrogen bonding. *Nature* **1991**, *349* (6308), 400-401.
193. Liu, H.; Avoce, D.; Song, Z.; Zhu, X. X., N-Isopropylacrylamide Copolymers with Acrylamide and Methacrylamide Derivatives of Cholic Acid: Synthesis and Characterization. *Macromol. Rapid Commun.* **2001**, *22* (9), 675-680.
194. Eliassaf, J., Aqueous solutions of poly(N-isopropylacrylamide). *J. Appl. Polym. Sci.* **1978**, *22* (3), 873-874.
195. Chiantore, O.; Guaita, M.; Trossarelli, L., Solution properties of poly(N-isopropylacrylamide). *Macromol. Chem. Phys.* **1979**, *180* (4), 969-973.
196. Wu, X. S.; Hoffman, A. S.; Yager, P., Synthesis and characterization of thermally reversible macroporous poly(N-isopropylacrylamide) hydrogels. *J. Polym. Sci., Part A: Polym. Chem.* **1992**, *30* (10), 2121-2129.
197. Xia, Y.; Yin, X.; Burke, N. A. D.; Stöver, H. D. H., Thermal Response of Narrow-Disperse Poly(N-isopropylacrylamide) Prepared by Atom Transfer Radical Polymerization. *Macromolecules* **2005**, *38* (14), 5937-5943.
198. Mukherji, D.; Marques, C. M.; Kremer, K., Polymer collapse in miscible good solvents is a generic phenomenon driven by preferential adsorption. *Nature Comm.* **2014**, *5*, 4882.
199. Oliveira, T. E. d.; Mukherji, D.; Kremer, K.; Netz, P. A., Effects of stereochemistry and copolymerization on the LCST of PNIPAm. *J. Chem. Phys.* **2017**, *146* (3), 034904.
200. Abbott, L. J.; Tucker, A. K.; Stevens, M. J., Single Chain Structure of a Poly(N-isopropylacrylamide) Surfactant in Water. *J. Phys. Chem. B* **2015**, *119* (9), 3837-3845.
201. Du, H.; Wickramasinghe, R.; Qian, X., Effects of Salt on the Lower Critical Solution Temperature of Poly (N-Isopropylacrylamide). *J. Phys. Chem. B* **2010**, *114* (49), 16594-16604.
202. Hugouvieux, V.; Axelos, M. A. V.; Kolb, M., Amphiphilic Multiblock Copolymers: From Intramolecular Pearl Necklace to Layered Structures. *Macromolecules* **2009**, *42* (1), 392-400.

203. Deshmukh, S.; Mooney, D. A.; MacElroy, J. M. D., Molecular simulation study of the effect of cross-linker on the properties of poly(N-isopropyl acrylamide) hydrogel. *Mol. Simul.* **2011**, *37* (10), 846-854.
204. Schilli, C. M.; Zhang, M.; Rizzardo, E.; Thang, S. H.; Chong, Y. K.; Edwards, K.; Karlsson, G.; Müller, A. H. E., A New Double-Responsive Block Copolymer Synthesized via RAFT Polymerization: Poly(N-isopropylacrylamide)-block-poly(acrylic acid). *Macromolecules* **2004**, *37* (21), 7861-7866.
205. Shibayama, M.; Mizutani, S.-y.; Nomura, S., Thermal Properties of Copolymer Gels Containing N-Isopropylacrylamide. *Macromolecules* **1996**, *29* (6), 2019-2024.
206. Feil, H.; Bae, Y. H.; Feijen, J.; Kim, S. W., Effect of comonomer hydrophilicity and ionization on the lower critical solution temperature of N-isopropylacrylamide copolymers. *Macromolecules* **1993**, *26* (10), 2496-2500.
207. Schild, H. G.; Tirrell, D. A., Interaction of poly (N-isopropylacrylamide) with sodium n-alkyl sulfates in aqueous solution. *Langmuir* **1991**, *7* (4), 665-671.
208. Zhang, Y.; Furyk, S.; Sagle, L. B.; Cho, Y.; Bergbreiter, D. E.; Cremer, P. S., Effects of Hofmeister Anions on the LCST of PNIPAM as a Function of Molecular Weight. *J. Phys. Chem. C* **2007**, *111* (25), 8916-8924.
209. Virtanen, J.; Arotçaréna, M.; Heise, B.; Ishaya, S.; Laschewsky, A.; Tenhu, H., Dissolution and Aggregation of a Poly(NIPA-block-sulfobetaine) Copolymer in Water and Saline Aqueous Solutions. *Langmuir* **2002**, *18* (14), 5360-5365.
210. Yin, X.; Hoffman, A. S.; Stayton, P. S., Poly(N-isopropylacrylamide-co-propylacrylic acid) Copolymers That Respond Sharply to Temperature and pH. *Biomacromolecules* **2006**, *7* (5), 1381-1385.
211. Soppimath, K. S.; Tan, D. C. W.; Yang, Y. Y., pH-Triggered Thermally Responsive Polymer Core-Shell Nanoparticles for Drug Delivery. *Adv. Mater.* **2005**, *17* (3), 318-323.
212. Xu, F.-J.; Kang, E.-T.; Neoh, K.-G., pH- and temperature-responsive hydrogels from crosslinked triblock copolymers prepared via consecutive atom transfer radical polymerizations. *Biomaterials* **2006**, *27* (14), 2787-2797.
213. Crespy, D.; Rossi, R. M., Temperature-responsive polymers with LCST in the physiological range and their applications in textiles. *Polym. Int.* **2007**, *56* (12), 1461-1468.
214. Zhang, J. L.; Srivastava, R. S.; Misra, R. D. K., Core-Shell Magnetite Nanoparticles Surface Encapsulated with Smart Stimuli-Responsive Polymer: Synthesis, Characterization, and LCST of Viable Drug-Targeting Delivery System. *Langmuir* **2007**, *23* (11), 6342-6351.
215. Zhang, J.; Misra, R. D. K., Magnetic drug-targeting carrier encapsulated with thermosensitive smart polymer: Core-shell nanoparticle carrier and drug release response. *Acta Biomat.* **2007**, *3* (6), 838-850.

216. Schmaljohann, D., Thermo- and pH-responsive polymers in drug delivery. *Adv. Drug Deliv. Rev.* **2006**, *58* (15), 1655-1670.
217. Inomata, H.; Goto, S.; Saito, S., Phase transition of N-substituted acrylamide gels. *Macromolecules* **1990**, *23* (22), 4887-4888.
218. Ito, S., Phase Transition of Aqueous Solution of Poly (<I>N</I>-alkylacrylamide) Derivatives Effects of Side Chain Structure. *KOBUNSHI RONBUNSHU* **1989**, *46* (7), 437-443.
219. Kubota, K.; Hamano, K.; Kuwahara, N.; Fujishige, S.; Ando, I., Characterization of Poly(N-isopropylmethacrylamide) in Water. *Polym. J.* **1990**, *22* (12), 1051-1057.
220. Duracher, D.; Elaïssari, A.; Pichot, C., Characterization of cross-linked poly(N-isopropylmethacrylamide) microgel latexes. *Colloid. Polym. Sci.* **1999**, *277* (10), 905-913.
221. Tang, Y.; Ding, Y.; Zhang, G., Role of Methyl in the Phase Transition of Poly(N-isopropylmethacrylamide). *J. Phys. Chem. B* **2008**, *112* (29), 8447-8451.
222. Salmerón Sánchez, M.; Hanyková, L.; Ilavský, M.; Monleón Pradas, M., Thermal transitions of poly(N-isopropylmethacrylamide) in aqueous solutions. *Polymer* **2004**, *45* (12), 4087-4094.
223. Gross, M. C. a. S., Hybrid Materials Based on the Embedding of Organically Modified Transition Metal Oxoclusters or Polyoxometalates into Polymers for Functional Applications: A Review. *Materials* **2014**, *7* (5), 3956-3989.
224. Sabo Suleiman, J.; Hu, B.; Pu, X.; Huang, C.; Jiang, Z., Nanometer-sized zirconium dioxide microcolumn separation/preconcentration of trace metals and their determination by ICP-OES in environmental and biological samples. *Microchim. Acta* **2007**, *159* (3), 379-385.
225. Shariati, S.; Yamini, Y., Cloud point extraction and simultaneous determination of zirconium and hafnium using ICP-OES. *J. Colloid Interface Sci.* **2006**, *298* (1), 419-425.
226. Agnihotri, S. A.; Mallikarjuna, N. N.; Aminabhavi, T. M., Recent advances on chitosan-based micro- and nanoparticles in drug delivery. *J. Controlled Release* **2004**, *100* (1), 5-28.
227. Shi, A.-m.; Li, D.; Wang, L.-j.; Li, B.-z.; Adhikari, B., Preparation of starch-based nanoparticles through high-pressure homogenization and miniemulsion cross-linking: Influence of various process parameters on particle size and stability. *Carbohydr. Polym.* **2011**, *83* (4), 1604-1610.
228. van Berkum, S.; Biewenga, P. D.; Verkleij, S. P.; van Zon, J. B. A.; Boere, K. W. M.; Pal, A.; Philipse, A. P.; Ern , B. H., Swelling Enhanced Remanent Magnetization of Hydrogels Cross-Linked with Magnetic Nanoparticles. *Langmuir* **2015**, *31* (1), 442-450.
229. Kurniasih, I. N.; Liang, H.; Mohr, P. C.; Khot, G.; Rabe, J. P.; Mohr, A., Nile Red Dye in Aqueous Surfactant and Micellar Solution. *Langmuir* **2015**, *31* (9), 2639-2648.

230. Plenderleith, R.; Swift, T.; Rimmer, S., Highly-branched poly(N-isopropyl acrylamide)s with core-shell morphology below the lower critical solution temperature. *RSC Advances* **2014**, *4* (92), 50932-50937.
231. Thivaivos, I.; Bokias, G., Adsorption of Nile red by poly(N-isopropylacrylamide) gels in binary water/tetrahydrofuran mixtures. *J. Appl. Polym. Sci.* **2010**, *116* (3), 1509-1514.
232. Li, D.; Jiang, J.; Huang, Q.; Wang, G.; Zhang, M.; Du, J., Light-triggered "on-off" switching of fluorescence based on a naphthopyran-containing compound polymer micelle. *Polym. Chem.* **2016**, *7* (20), 3444-3450.
233. Yee, M. M.; Tsubone, M.; Morita, T.; Yusa, S.-i.; Nakashima, K., Fluorescence ON-OFF switching using micelle of stimuli-responsive double hydrophilic block copolymers: Nile Red fluorescence in micelles of poly(acrylic acid-b-N-isopropylacrylamide). *J. Lumin.* **2016**, *176*, 318-323.
234. Chen, C.-Y.; Chen, C.-T., A PNIPAM-based fluorescent nanothermometer with ratiometric readout. *Chem. Commun.* **2011**, *47* (3), 994-996.
235. Santoro, S.; Sebastian, V.; Moro, A. J.; Portugal, C. A. M.; Lima, J. C.; Coelho, I. M.; Crespo, J. G.; Mallada, R., Development of fluorescent thermoresponsive nanoparticles for temperature monitoring on membrane surfaces. *J. Colloid Interface Sci.* **2017**, *486*, 144-152.
236. Wu, Y.; Liu, J.; Ma, J.; Liu, Y.; Wang, Y.; Wu, D., Ratiometric Nanothermometer Based on Rhodamine Dye-Incorporated F127-Melamine-Formaldehyde Polymer Nanoparticle: Preparation, Characterization, Wide-Range Temperature Sensing, and Precise Intracellular Thermometry. *ACS Appl. Mater. Interf.* **2016**, *8* (23), 14396-14405.
237. Liu, X.; Tang, X.; Hou, Y.; Wu, Q.; Zhang, G., Fluorescent nanothermometers based on mixed shell carbon nanodots. *RSC Advances* **2015**, *5* (99), 81713-81722.
238. Hemmer, E.; Quintanilla, M.; Légaré, F.; Vetrone, F., Temperature-Induced Energy Transfer in Dye-Conjugated Upconverting Nanoparticles: A New Candidate for Nanothermometry. *Chem. Mater.* **2015**, *27* (1), 235-244.
239. Sackett, D. L.; Wolff, J., Nile red as a polarity-sensitive fluorescent probe of hydrophobic protein surfaces. *Anal. Biochem.* **1987**, *167* (2), 228-234.
240. Loyson, P., Galilean Thermometer Not So Galilean. *J. Chem. Educ.* **2012**, *89* (9), 1095-1096.
241. Gross, S.; Trimmel, G.; Schubert, U.; Noto, V. D., Inorganic-organic hybrid materials from poly(methylmethacrylate) crosslinked by an organically modified oxozirconium cluster. Synthesis and characterization. *Polym. Adv. Technol.* **2002**, *13* (3-4), 254-259.
242. Thomas, A.; Schlaad, H.; Smarsly, B.; Antonietti, M., Replication of Lyotropic Block Copolymer Mesophases into Porous Silica by Nanocasting: Learning about Finer Details of Polymer Self-Assembly. *Langmuir* **2003**, *19* (10), 4455-4459.

-
243. Renz, P.; Kokkinopoulou, M.; Landfester, K.; Lieberwirth, I., Imaging of Polymeric Nanoparticles: Hard Challenge for Soft Objects. *Macromol. Chem. Physic.* **2016**, *217* (17), 1879-1885.
244. Seah, M. P.; Briggs, D., *Practical Surface Analysis, Auger and X-ray Photoelectron Spectroscopy*. J. Wiley & Sons: **1990**; Vol. 1, p 543.
245. Moulder, J. F., *Handbook of X-ray Photoelectron Spectroscopy: A Reference Book of Standard Spectra for Identification and Interpretation of XPS Data*. Physical Electronics Division, Perkin-Elmer Corporation: **1992**.
246. Shirley, D. A., High-Resolution X-Ray Photoemission Spectrum of the Valence Bands of Gold. *Phys. Rev. B.* **1972**, *5* (12), 4709-4714.
247. X-ray Photoelectron Spectroscopy Database 20, V., National Institute of Standards and Technology, Gaithersburg, MD; <http://srdata.nist.gov/XPS>.

A. Acronyms List and Symbols

^1H NMR	Proton nuclear magnetic resonance
AIBN	Azobisisobutyronitrile
AMBN	2,2'-azobis-(2-methylbutyronitrile)
ATR	Attenuated total reflectance
ATRP	Atom transfer radical polymerizations
BB	Building blocks
CCD	Charge-coupled device
CMC	Critical micellar concentration
CP-MAS NMR	Solid-state nuclear magnetic resonance
DLS	Dynamic light scattering
DMF	Dimethylformamide
DMSO	Dimethyl sulfoxide
DSC	Differential scanning calorimetry
EXAFS	Extended X-ray absorption fine structure spectroscopy
FET	Field effect transistor
FTIR	Fourier transform infrared spectroscopy
GC	Gas chromatography
GPC	Gel permeation chromatography
HDS	Hydrodesulfurization
HLB	Hydrophilic-lipophilic balance
ICP-OES	Inductively coupled plasma optical emission spectrometry
LCST	Lower critical solution temperature
MMA	Methyl methacrylate
MRI	Magnetic resonance imaging
NAGA	<i>N</i> -acryloyl glycinamide
NIPAM	<i>N</i> -isopropylacrylamide
NIPMM	<i>N</i> -isopropylmethacrylamide
NMGA	<i>N</i> -methacryloyl glycinamide
NMR	Nuclear magnetic resonance
NR	Nile red
P(E/B)- <i>b</i> -PEO	Poly(ethylene/butylene)- <i>block</i> -poly(ethylene oxide)
PGMA	Poly(glycidyl methacrylate)
PMMA	Poly(methyl methacrylate)
PNAGA	Poly(<i>N</i> -acryloyl glycinamide)

PNIPAM	Poly(<i>n</i> -isopropylacrylamide)
PNMGA	Poly(<i>N</i> - methacryloyl glycinamide)
PNnPA	<i>N-n</i> -propylacrylamide
PNnPMA	<i>N-n</i> -propylmethacrylamide
POM	Polyoxometalates
POSS	Polyhedral silsesquioxanes
RF	Radiofrequency
ROMP	Ring-opening metathesis polymerization
SDS	Sodium dodecyl sulfate
SEC	Size-exclusion chromatography
SEM	Scanning electron microscopy
STEM	Scanning transmission electron microscopy
TEM	Transmission electron microscopy
THF	Tetrahydrofuran
Ti ₉	Ti ₉ O ₈ (OPr) ₄ (OMc) ₁₆
TOF	Turnover frequency
TON	Turnover number
UCST	Upper critical solution temperature
UV	Ultraviolet
VPT	Volume phase transition
XAFS	X-ray absorption fine structure
XANES	X-ray absorption near edge structure
XAS	X-ray absorption spectroscopy
XPS	X-ray photoelectron spectroscopy
XRD	X-ray diffraction
Zr ₄	Zr ₄ O ₂ (OMc) ₁₂
<i>c</i>	Concentration
<i>d</i>	Thickness of the sample
<i>I</i>	Intensity
<i>K</i>	Scattering vector
<i>k</i> ; <i>k_m</i> ; <i>k_p</i> ; <i>k₁</i> ; <i>k₂</i>	Kinetic constants
<i>P</i>	Pressure
<i>r</i>	Radius
<i>R</i>	Universal gas constant
<i>t</i>	Starting time
<i>γ</i>	Interfacial tension

Δp_L	Laplace pressure
λ	Wavelength
τ	Evolution time
Γ	Relaxation rate
Π_{osm}	Osmotic pressure
T	Temperature
k	Boltzmann constant
η	Dynamic viscosity

B. List of Figures

- Figure 1.1.** Hybrid examples: (a) a liger is a hybrid cross between a male lion (*Panthera leo*) and a female tiger (*Panthera tigris*); (b) hybrid maps (of the city of Urbino) are the combination of satellite maps and street maps; (c) grapefruit (*Citrus × paradisi*) is a hybrid originating between sweet orange (*C. sinensis*) and pomelo or shaddock (*C. maxima*); (d) Hybrid Toyota vehicles.1
- Figure 1.2.** Maya blue: (a) on the background of an ancient Mayan paint and (b) chemical structure by Chiari *et al.*¹⁴3
- Figure 2.1.** Possible ways to functionalize inorganic BB: (a) post-synthesis surface functionalization and (b) direct *in situ* functionalization. The formed functionalized cluster is either way used as inorganic BB in the next polymerization step.¹⁶7
- Figure 2.2.** Structure of (a) $Zr_4O_2(OMc)_{12}$ ⁴⁷ and (b) $Zr_6(OH)_4O_4(OMc)_{12}$.⁴⁸8
- Figure 2.3.** Structure of $Ti_9O_8(OPr)_4(OMc)_{16}$ by Kickelbick *et al.*⁵⁹10
- Figure 2.4.** Schematic illustration of (a) coalescence and (b) Ostwald ripening in miniemulsion system.16
- Figure 2.5.** Schematic representation for the preparation of metal oxocluster/polymer hybrid nanoparticles by using miniemulsion polymerization technique.20
- Figure 3.1.** Evaluation of the soluble part content in hybrid particles cross-linked with metal oxocluster: after centrifugation the supernatant solution is analyzed by GPC.21
- Figure 4.1.** Schematic illustration of the dual role of $Zr_4O_2(\text{methacrylate})_{12}$ in hybrid nanoparticles: cross-linker and catalytic site.28
- Figure 4.2.** Preparation of the cross-linked hybrid poly(MMA-*co*-**Zr₄**) nanoparticles: (a) synthesis of zirconium oxocluster $Zr_4O_2(\text{methacrylate})_{12}$, (b) copolymerization with MMA in miniemulsion droplets.30
- Figure 4.3.** FTIR spectra of (a) **Zr₄**, **S0**, **S5** and (b) **Zr₄**, **L0**, **L5**.30
- Figure 4.4.** **Zr₄** content detected by elemental analysis (ICP-OES) of hybrid poly(MMA-*co*-**Zr₄**) nanoparticles prepared using either SDS or Lutensol AT50 as surfactants.32
- Figure 4.5.** DLS measurement of the water suspension as a function of the hydrodynamic diameter of hybrid poly(MMA-*co*-**Zr₄**) nanoparticles prepared using either SDS or Lutensol AT50 as surfactants.32
- Figure 4.6.** SEM images of hybrid poly(MMA-*co*-**Zr₄**) nanoparticles prepared using either SDS or Lutensol AT50 as surfactants.34
- Figure 4.7.** TEM images of hybrid poly(MMA-*co*-**Zr₄**) nanoparticles with 10 wt% of **Zr₄**. Bright field images of (a) sample **S10** and (b) sample **L10** and corresponding zirconium mapping (c) and

(d), respectively. (The white spots in panel (a) are due to measuring artifacts caused by the cutting procedure).35

Figure 4.8. Fourier transforms of the EXAFS spectra for the cross-linked hybrid poly(MMA-*co*-Zr₄) nanoparticles compared to the Zr₄ as a reference. The samples with (a) 5 wt% and (b) 10 wt% of Zr₄ (synthesized using either SDS or Lutensol AT50 as surfactants) are shown.36

Figure 4.9. The poly(MMA-*co*-Zr₄) nanoparticles cross-linked fraction as a function of the Zr₄ detected content through ICP-OES. The cross-linked fraction was determined as the inverse of the soluble fractions, the latter being obtained through GPC on the supernatants. The cross-linker efficiency and the incorporation of Zr₄ are higher using SDS as a surfactant.38

Figure 4.10. ¹³C CP-MAS spectra of (a) a mixture of S0 (PMMA nanoparticles) and Zr₄ 5%, (b) S5, (c) Zr₄ oxocluster and (d) S0.39

Figure 4.11. DLS measurement of the hydrodynamic diameter of hybrid poly(MMA-*co*-Zr₄) nanoparticles (a) in water and THF for SDS samples and (b) additionally in acetonitrile for Lutensol AT50 samples as a function of Zr₄ content.41

Figure 4.12. DSC curves (a) and glass transition temperature as a function of the Zr₄ content (b) of hybrid poly(MMA-*co*-Zr₄) nanoparticles prepared with SDS. The glass transition temperature of the samples shown is calculated from the first derivative.41

Figure 4.13. Kinetic trace for the oxidation of methyl *p*-tolyl sulfide (S, black squares) to its sulfoxide (SO, red squares) and sulfone (SO₂, blue squares) by hydrogen peroxide in the presence of L10 as heterogeneous catalyst at 50 °C. The Zr₄ is present in 0.1 mol% with respect to the methyl *p*-tolyl sulfide. The continuous lines show second order kinetic fittings.42

Figure 4.14. Kinetic traces for the oxidation of methyl *p*-tolyl sulfide (red squares) to its sulfoxide (green circles) and sulfone (blue triangles) by hydrogen peroxide in the presence of (a) S10, (b) L7, (c) S7, (d) L5, (e) S5 as heterogeneous catalyst at 50 °C. The Zr₄ is present in 0.1 mol% respect to the methyl *p*-tolyl sulfide. Symbols: experimental points; lines: second order kinetic fitting.44

Figure 4.15. FTIR spectra of (a) S10 before and after catalysis and (b) L10 before and after catalysis.46

Figure 4.16. SEM images of the sample (a) S10 and (b) L10 after catalysis. The picture on the right clearly show the consequence of the lower cross-linking efficacy of L10.46

Figure 4.17. Kinetic traces for the oxidation of methyl *p*-tolyl sulfide (red squares) to its sulfoxide (green circles) and sulfone (blue triangles) by hydrogen peroxide in the presence of (a) L10 and (b) L7 as heterogeneous catalyst at 50 °C. The Zr₄ is present in 0.1 mol% respect to the methyl *p*-tolyl sulfide. The catalysts were removed after 30 min by high speed centrifugation. ..47

Figure 4.18. The methyl *p*-tolyl sulfide conversion and the selectivity to the sulfone at (a) 4 h and (b) 24 h in the presence of S7, S10, L7 and L10 in the first cycle and after recycling of the catalysts with a fresh mixture of sulfide and H₂O₂ (labeled as “_R”).48

- Figure 4.19.** The methyl *p*-tolyl sulfide conversion and the selectivity towards the sulfone at 24 h in the presence of **L10** in the first cycle and after three recycles of the catalysts with a fresh mixture of sulfide and H₂O₂ (labeled as “_R1”, “_R2”, “_R3” for the first, second and third recycle, respectively).48
- Figure 4.20.** ¹H NMR spectra of (a) a mixture of **Zr₄** and Lutensol AT50, (b) Lutensol AT50, and (c) **Zr₄**, all in THF.50
- Figure 4.21.** ¹H NMR spectra of (a) a mixture of **Zr₄** and Lutensol AT50, (b) Lutensol AT50, and (c) **Zr₄**, all in toluene.51
- Figure 4.22.** ¹H NMR spectra of (a) a mixture of **Zr₄** and SDS, (b) SDS, and (c) **Zr₄**, all in THF.51
- Figure 4.23.** ¹H NMR spectra of (a) a mixture of **Zr₄** and SDS, (b) SDS, and (c) **Zr₄**, all in toluene.52
- Figure 4.24.** Kinetic traces for (a), (c), and (e) the oxidation of benzylic alcohol (black squares) to its benzaldehyde (red circles) and for (b), (d), and (f) the epoxidation of cyclooctene (black squares) to its oxide (red circles) by hydrogen peroxide in the presence of Ti₉O₈(OPr)₄(OMc)₁₆ oxocluster as homogeneous catalyst at 50 °C. The **Ti₉** is present in 0.1 mol% with respect to the reagents, the reaction was conducted using either (a) and (b) half equivalent or (c) and (d) two equivalents of H₂O₂ with respect to the reagents. Charts (e) and (f) represent the blank in presence of two equivalents equivalent H₂O₂ and without **Ti₉**.57
- Figure 4.25.** Kinetic traces for the epoxidation of cyclooctene by hydrogen peroxide in the presence of Ti₉O₈(OPr)₄(OMc)₁₆ oxocluster as homogeneous catalyst at 50 °C. The **Ti₉** is present in 0.1 mol% respect to the reagents, the reaction was conducted either using half equivalent (red circles) or two equivalents of H₂O₂ (black squares) respect to the reagents.58
- Figure 4.26.** FTIR spectra of Ti₉O₈(OPr)₄(OMc)₁₆ before and after treatment with hydrogen peroxide.59
- Figure 4.27.** Kinetic traces for (a), (b), and (c) the oxidation of benzylic alcohol (black squares) to benzaldehyde (red circles) and for (d) the epoxidation of cyclooctene (black squares) to its oxide (red circles) by hydrogen peroxide at 50 °C. The reactions are conducted in presence of (a), (c), and (d) poly(NIPAM-*co*-**Ti₉**) nanoparticles and (b) poly(NMGA-*co*-**Ti₉**) nanoparticles. **Ti₉** is present in 0.1 mol% and 2 equivalents of H₂O₂ with respect to the reagents are used. The reaction solvent is either (a), (b), and (d) acetonitrile or (c) water.61
- Figure 4.28.** Schematic illustration of photoactivated copolymerization between methyl methacrylate (MMA) and Zr₄O₂(methacrylate)₁₂. The copolymerization is occurring in miniemulsion droplets. The lenses of the UV protection glass correspond to the monomer droplets during irradiation (left) and to the polymer particle (right, after polymerization).63
- Figure 4.29.** UV spectra of Irgacure 2959 (**P1**), Irgacure 754 (**P2**), Irgacure 369 (**P3**), and filter UG11.67
- Figure 4.30.** Hydrodynamic diameters of hybrid poly(MMA-*co*-**Zr₄**) nanoparticles in water suspensions determined by DLS as a function of oxocluster weight content.67

Figure 4.31. SEM images of hybrid poly(MMA- <i>co</i> -Zr ₄) nanoparticles synthesized using Irgacure 754 (P1).....	68
Figure 4.32. SEM images of hybrid poly(MMA- <i>co</i> -Zr ₄) nanoparticles synthesized using Irgacure 754 (P2).....	69
Figure 4.33. SEM images of hybrid poly(MMA- <i>co</i> -Zr ₄) nanoparticles synthesized using Irgacure 369 (P3).....	70
Figure 4.34. Cross-linked fraction (from GPC measurements) of hybrid poly(MMA- <i>co</i> -Zr ₄) nanoparticles as a function of the Zr ₄ content (determined by ICP-OES).	71
Figure 4.35. FTIR ATR spectra for the samples P1-0 , P1-5 , P2-0 , P2-5 , T1-0 and T1-5 , from 0s to complete polymerization conversion.	73
Figure 4.36. Typical IR spectra of poly(MMA- <i>co</i> -Zr ₄) nanoparticles (top left) and the evolution of the C=C peak during the polymerization (bottom right).....	74
Figure 4.37. MMA conversion as a function of time for polymerization process in PMMA (samples P1-0 , P2-0 , T1-0) and hybrid poly(MMA- <i>co</i> -Zr ₄) (P1-5 , P2-5 , T1-5) nanoparticles: P1-0 and P1-5 , black full and hollow circles, respectively); P2-0 and P2-5 , red full and hollow triangles, respectively; and T1-0 and T1-5 , blue full and hollow squares, respectively. Solid curves are calculated by least-squares fitting of experimental data to the model given by eq. 4.6.	74
Figure 4.38. Diluted miniemulsion (100 μL : 4 mL) with SDS water solution (3 g·L ⁻¹) of (a) MMA/Zr ₄ /Hexadecane and (b) MMA/Hexadecane.	76
Figure 4.39. TEM images of the cross-linked hybrid poly(NIPAM- <i>co</i> -Zr ₄) nanocapsules. The samples were embedded in trehalose and negatively stained with uranyl acetate.	81
Figure 4.40. TEM images of the cross-linked hybrid poly(NIPMM- <i>co</i> -Zr ₄) nanocapsules. The samples were embedded in trehalose and negatively stained with uranyl acetate.	82
Figure 4.41. Fourier transforms of the EXAFS spectra for poly(NIPAM- <i>co</i> -Zr ₄) nanocapsules containing 10 wt% of Zr ₄ compared to the Zr ₄ as a reference. Data non-corrected for phase shift.	83
Figure 4.42. Hydrodynamic diameter (<i>D</i> _h) of (a) poly(NIPAM- <i>co</i> -Zr ₄) and (b) poly(NIPMM- <i>co</i> -Zr ₄) nanocapsules in water suspension as a function of temperature. The samples were prepared with 1, 5 and 10 wt% of Zr ₄	84
Figure 4.43. (a) Fluorescence emission spectra of PNIPAM nanocapsules and cross-linked hybrid poly(NIPAM- <i>co</i> -Zr ₄) nanocapsules at 27 °C (dashed line) and 41 °C (straight line). (b) Plots of maximum fluorescence intensity versus temperature of PNIPAM nanocapsules and cross-linked hybrid poly(NIPAM- <i>co</i> -Zr ₄) nanocapsules in water suspension. Hybrid nanocapsules were prepared with 1, 5 and 10 wt% of Zr ₄ . Concentration of nanocapsules: 2 mg·mL ⁻¹ . λ _{ex} = 549 nm, band widths: Δλ _{em} = 20 nm, Δλ _{ex} = 20 nm, λ _{em} = 628 nm [(for panel (b))].	85

Figure 4.44. Plots of maximum fluorescence intensity versus **Zr₄** initial amount as comonomer of nanocapsules dispersion supernatants after centrifugation step at 40 °C. The data are collect at 41 °C. Concentration of nanocapsules before centrifugation: 2 mg·mL⁻¹. $\lambda_{em} = 628$ nm, $\lambda_{ex} = 549$ nm, band widths: $\Delta\lambda_{em} = 20$ nm, $\Delta\lambda_{ex} = 20$ nm.86

Figure 4.45. Reversibility of fluorescence of PNIPAM nanocapsules and cross-linked hybrid poly(NIPAM-*co*-**Zr₄**) nanocapsules in water suspension alternating temperature between 32 °C and 41 °C. Concentration of nanocapsules: 2 mg·mL⁻¹. $\lambda_{em} = 628$ nm, $\lambda_{ex} = 549$ nm, band widths: $\Delta\lambda_{em} = 20$ nm, $\Delta\lambda_{ex} = 20$ nm.....87

Figure 4.46. Picture of (a) Galileo thermometer and (b) Galileo-like thermometer concept using cross-linked hybrid nanocapsules.88

C. List of Tables

Table 4.1. Synthetic details for the preparation of poly(MMA- <i>co</i> - Zr₄) nanoparticles.	31
Table 4.2. Main features of the cross-linked hybrid poly(MMA- <i>co</i> - Zr₄) nanoparticles.	33
Table 4.3. Atomic percentages obtained by XPS. In brackets: theoretical values.	37
Table 4.4. Evaluation of the unreacted double bonds through ¹³ C CP-MAS.....	39
Table 4.5. Oxidation of methyl <i>p</i> -tolylsulfide with H ₂ O ₂ in the presence of Zr oxoclusters into nanoparticles.....	43
Table 4.6. Theoretical and determined Zr₄ content of the particles after catalysis.....	47
Table 4.7. Evaluation of SDS amount by using Stains-All dye.	53
Table 4.8. Main features of poly(NAGA- <i>co</i> - Ti₉), poly(NMGA- <i>co</i> - Ti₉) and poly(NIPAM- <i>co</i> - Ti₉) nanoparticles.....	60
Table 4.9. Thermoresponsive behavior of hybrid poly(NIPAM- <i>co</i> - Ti₉), poly(NAGA- <i>co</i> - Ti₉), poly(NMGA- <i>co</i> - Ti₉), poly(N-acryloyl glycinamide) and poly(N-methacryloyl glycinamide) nanoparticles.....	61
Table 4.10. Synthetic details and main features of the cross-linked hybrid poly(MMA- <i>co</i> - Zr₄) nanoparticles presented in this section.	72
Table 4.11. Synthetic details and main features of the cross-linked hybrid poly(NIPAM- <i>co</i> - Zr₄) and poly(NIPMM- <i>co</i> - Zr₄) nanocapsules.	81
Table 4.12. Fluorescence maximum intensity at 27 °C and 41 °C of the cross-linked hybrid poly(NIPAM- <i>co</i> - Zr₄) nanocapsules with different amount of Zr₄	84

D. List of Schemes

- Scheme 4.1.** Oxidation of methyl *p*-tolylsulfide to the corresponding sulfoxide and sulfone by using hydrogen peroxide as a oxidant and hybrid poly(MMA-*co*-Zr₄) nanoparticles as a catalyst.43
- Scheme 4.2.** Oxidation of benzylic alcohol to the corresponding benzaldehyde and benzoic acid by using hydrogen peroxide as oxidant and Ti based catalyst.....49
- Scheme 4.3.** Oxidation of cyclooctene to the corresponding cyclooctene oxide by using hydrogen peroxide as oxidant and Ti based catalyst.49
- Scheme 4.4.** Free radicals mechanisms formation for (a) Irgacure 2959 (**P1**), (b) Irgacure 754 (**P2**), (c) Irgacure 369 (**P3**), and (d) AMBN (**T1**).66

E. Acknowledgments

F. Curriculum Vitae

Cesare Benedetti was born in Urbino, Italy, on July 30th in 1988. In 2007, after finishing the technical high school studies in Chemistry, he started his bachelor studies in Industrial Chemistry at the Alma Mater Studiorum – University of Bologna. His bachelor's thesis, concerning the optimization of the purification process of additives for plastics materials, was performed at Department of Process/Plant Support of BASF (Pontecchio Marconi, Bologna, Italy). In 2010, he obtained his Bachelor of Science degree with the mark of 106/110. In the same year, he started a master in Industrial Chemistry at the same university. In 2012, he conducted his Master's thesis on defects in thermosensitive colloidal crystals at the Van't Hoff Laboratory for Physical and Colloid Chemistry (Debye Institute for Nanomaterials Science, Utrecht University, the Netherlands) under the supervision of Dr. Andrei Petukhov and Dr. Elisabetta Venuti. During his Master he got a Special Excellence Award Alma Mater Studiorum Certificate of Merit by the President Prof. Dionigi. After finalizing his MSc degree (2012; 110/110 cum laude), he spent 9 months as a research assistant, first at the University of Bologna, and then at the University of Parma, under the supervision of Prof. Dr. Alberto Girlando and Dr. Elisabetta Venuti. In this period, he focused on the study of molecular organic semiconductors and superconductors materials in the solid state. In 2013, before starting his doctoral studies, he worked as a laboratory responsible and quality manager at Italiana Corrugati S.p.a. In 2014, he started the PhD at the Department of Physical Chemistry of Polymers at the Max Planck Institute for Polymer Research under the supervision of Prof. Dr. Katharina Landfester, Dr. Rafael Muñoz-Espí (University of Valencia, Spain), and Dr. Silvia Gross (University of Padua, Italy). His PhD project focused on the synthesis and application of metal oxocluster/polymer hybrid nanoparticles.

G. Scientific Contributions

G.1. Publications

C. **Benedetti**, A. Cazzolaro, M. Carraro, R. Graf, K. Landfester, S. Gross, and R. Muñoz-Espí, *Dual Role of Zirconium Oxoclusters in Hybrid Nanoparticles: Cross-Linkers and Catalytic Sites*, ACS Appl. Mater. Interf. **2016**, 8, 26275.

C. **Benedetti**, P. Flouda, A. Antonello, C. Rosenauer, F.F. Pérez-Pla, K. Landfester, S. Gross, and R. Muñoz-Espí, *Zirconium Oxocluster/Polymer Hybrid Nanoparticles Prepared by Photoactivated Miniemulsion Copolymerization* (submitted).

J.M. Meijer, C. **Benedetti**, D. Verwijmeren, J. Hilhorst, A. V. Petukhov, *Inducing Defects in Colloidal Crystals with Thermosensitive PNIPAm Particles* (in preparation).

A. Antonello, C. **Benedetti**, M. Kokkinopoulou, K. Kirchhoff, V. Fischer, K. Landfester, S. Gross, and R. Muñoz-Espí, *Crystallization of Ammonium Phosphomolybdate: Miniemulsion vs Bulk* (in preparation).

C. **Benedetti**, M. Kokkinopoulou, S.-M. Jo, A. Antonello, C. Rosenauer, K. Landfester, S. Gross, and R. Muñoz-Espí, *Hybrid Cross-Linked Nanocapsules with Zirconium Oxocluster as Galileo-like Nano-Thermometer* (in preparation).

G.2. Conferences

Oral presentation “Hybrid Catalytic Nanoparticles based on Zirconium Oxocluster” at the **252th ACS Meeting & Exposition** (2016) in Philadelphia

Oral presentation “Zirconium Oxocluster-Based Hybrid Nanoparticles for Catalysis Applications” at the **E-MRS Spring meeting** (2016) In Lille

Oral presentation “Hybrid Catalytic Nanoparticles Cross-Linked with Zr₄ Oxocluster for Oxidation Reactions” at the **European Polymer Congress** (2015) in Dresden

Poster presentation “Multifunctional Metal Oxocluster/Polymer Hybrid Nanoparticles prepared by Miniemulsion” at **European-Winter School on Physical Organic Chemistry (E-WiSPOC, 2015)** in Brixen

Poster presentation “Polymorphism in Blue-Luminescent Tetraphenylbutadiene Crystal” at **IX Convegno Nazionale Scienza e Tecnologia dei Materiali (INSTM, 2013)** in Bari